

## Alterations in chromosome spatial compartmentalization classify prostate cancer progression

Rebeca San Martin<sup>1</sup>, Priyojit Das<sup>2</sup>, Renata Dos Reis Marques<sup>1</sup>, Yang Xu<sup>2</sup>, Rachel Patton McCord<sup>1\*</sup>

<sup>1</sup> Department of Biochemistry & Cellular and Molecular Biology, University of Tennessee, 309 Ken and Blaire Mossman Bldg. 1311 Cumberland Ave, Knoxville, TN, 37996, USA

<sup>2</sup> UT-ORNL Graduate School of Genome Science and Technology, University of Tennessee, 309 Ken and Blaire Mossman Bldg. 1311 Cumberland Ave, Knoxville, TN, 37996, USA

\*Corresponding author: [rmccord@utk.edu](mailto:rmccord@utk.edu) ; (865)-974-3149

### Summary

Through a systematic analysis of chromosome conformation capture in a cohort of cells that model cancer progression, San Martin et.al. find that rearrangement of the 3D genome structure in prostate cancer is a potential mechanism for disease exacerbation and that genome-wide compartment identity can classify cancer according to progression.

### Abstract

Prostate cancer aggressiveness and metastatic potential are influenced by gene expression, genomic aberrations, and cellular morphology. These processes are in turn dependent in part on the 3D structure of chromosomes, packaged inside the nucleus. Using chromosome conformation capture (Hi-C), we conducted a systematic genome architecture comparison on a cohort of cell lines that model prostate cancer progression, ranging from normal epithelium to bone metastasis. Here, we describe how chromatin compartmentalization identity (A- open vs. B-closed) changes with progression: specifically, we find that 48 gene clusters switch from the B to the A compartment, including androgen receptor, WNT5A, and CDK14. These switches could prelude transcription activation and are accompanied by changes in the structure, size, and boundaries of the topologically associating domains (TADs). Further, compartmentalization changes in chromosome 21 are exacerbated with progression and may explain, in part, the genesis of the TMPRSS2-ERG translocation: one of the main drivers of prostate cancer. These results suggest that discrete, 3D genome structure changes play a deleterious role in prostate cancer progression.

### Introduction

Prostate cancer (PCa) is the predominant new cancer diagnosis in males in the United States. It is also the second most common cause of male cancer-related deaths, second only to lung cancer (Siegel et al., 2020). Patients with late-stage prostate cancer present with a higher incidence of metastases to trabecular bone (Jacobs, 1983, Bubendorf et al., 2000, Hernandez et al., 2018). The specific mechanisms that promote metastasis to bone are not understood. However, disseminated tumor cells can be detected in the blood of about 25% of PCa patients with localized disease. The abundance of these circulating tumor cells positively correlates with metastatic occurrence (Moreno et al., 2005, Danila et al., 2007, Todenhofer et al., 2016).

Metastatic cancer cells migrate out of the primary site squeezing through gaps much smaller than their nuclei, such as interstitial spaces within the organ and tight endothelial junctions to gain access to the circulation (Barbazan et al., 2017, Bergeman et al., 2016, Mierke, 2008). The rigidity of the nucleus, which depends on the inherent stiffness of the nuclear lamina and chromosomal ultrastructure, is the limiting step of this migration (Davidson et al., 2014, Hatch and Hetzer, 2016, Lammerding et al., 2006). The human genome's packaging into the nucleus's constrained space requires a systematic organization: from chromosomal territories (Meaburn and Misteli, 2007) to transcriptionally active and inactive chromatin compartments (Lieberman-Aiden et al., 2009). Within compartments, chromatin further organizes into topologically associating domains (TADs), which are segregated from each other by the insulator protein CTCF (Dixon et al., 2012, Nora et al., 2017), and finally into chromatin loops (Nuebler et al., 2018). With the advent of technologies such as genome-wide chromosome conformation capture (Hi-C), it has become clear that these structures are essential for proper gene regulation, DNA replication, and repair (Hnisz et al., 2016, Dekker and Mirny, 2016, Pope et al., 2014, McCord and Balajee, 2018). Further, rearrangement of these domains can impact both the nuclei's ability to squeeze through tight spaces during metastatic migration and the expression patterns of oncogenes (Gerlitz and Bustin, 2010, Stephens et al., 2018, Hnisz et al., 2016, Barutcu et al., 2015). Nuclear atypia is a common diagnostic tool in PCa (Verdone et al., 2015, Diamond et al., 1982), and there is evidence that the nuclear lamina content of prostate cells differs between normal epithelium, BPH, and cancer (Partin et al., 1993). This suggests that genome architectural changes may occur in prostate cancer and might influence cancer-promoting gene expression profiles and the nuclear malleability necessary for cancer cells to metastasize.

While several genomic loci have been associated with a higher risk for prostate cancer (Ahmadiyeh et al., 2010, Helfand et al., 2015, Du et al., 2016), one of the most predominant features of poor patient prognosis is the TMPRSS2-ERG translocation in chromosome 21 (Zhou et al., 2020, Demichelis et al., 2007, Tomlins et al., 2005). Interestingly, it has been shown that overexpression of ERG results in chromatin conformation changes (Rickman et al., 2012), but whether the gene fusion occurs due to increased transcription remains unclear. Since it is known that relative chromosome proximity can influence the pattern of translocations that occur (Zhang et al., 2012, Balajee et al., 2018), this type of local rearrangement could potentially result alterations in chromosome compartmentalization that increase contact frequency among the different loci, as previously described in other systems (Engreitz et al., 2012).

Recent studies into the 3D genome structure associated with prostate cancer (Rhie et al., 2019, Luo et al., 2017a, Taberlay et al., 2016), have contributed some insight into regulatory chromatin loops, epigenetic alterations, and the influence that variable structures have in transcription. However, these studies did not address whether there are early changes in genome architecture that persist throughout progression. In this context, changes in compartment identity from transcriptionally repressed heterochromatin to euchromatin poised for transcription could identify genes required for early oncogenesis and those necessary for metastasis. Further, changes in TAD positioning, or shifting of TAD boundaries could reveal altered interactions of neighboring promoter-enhancer regions.

In the present study, we use a combination of Hi-C and ChIP-seq to characterize the genome organization across a cohort of nine cell lines that model prostate cancer progression from the normal epithelium to bone metastasis, including two bone metastatic cell lines of African American lineage. We further assess the different hierarchical levels of genome organization: from large inter-chromosomal translocations to compartment identity to TAD location and TAD boundary shifting. We have identified a cohort of 387 genes that change compartment identity across prostate cancer progression. Interestingly, most of these genes switch compartments as proximal clusters. These compartment identity changes are accompanied by distinct structural features at higher resolution such as gain or loss of TAD structure, stalled transcriptional loops and structural deserts, and TAD boundary appearance, disappearance, or positional shifting. Finally, our results revealed several "genomic architecture hotspots" whose structural changes are persistent throughout the metastatic models; these include WNT5A, CDK14, androgen receptor (AR), and the TMPRSS2-ERG locus, among others. These results suggest that the 3D genome structure can be used as a prognostic marker for the progression of prostate cancer to bone metastasis.

## Methods

### *Cell lines*

RWPE-1, LNCaP, DU145, 22RV1, VCaP and PC3 cell lines were obtained from the Physical Sciences Oncology Network Bioresource Core Facility, supported by ATCC.

All cell lines were cultured according to standard protocols, subculturing cells as they reached 80% confluency with the following media formulations: RWPE media was comprised of keratinocyte specific media supplemented with EGF and bovine pituitary extract (Gibco 17005042). RPMI (Gibco 11835030) was supplemented to match the suggested formula by ATCC (4.5 g/L glucose, 2.383 g/L HEPES and 0.11 g/L sodium pyruvate) and 10% FBS (Corning 35-010-CV). This media was used for LNCaP, 22RV1 and PC3. DU145 cells were cultured in DMEM supplemented with 10% FBS, and DMEM F12: Ham 1:1 (Gibco 11-320-033) with 10% FBS was used for VCaP.

Cell lines MDAPCa2a and MDAPCa2b were a kind gift of Dr. Nora Navone (MD Anderson Cancer Center, Houston TX). These cell lines were grown in HPC1 media (Athena Enzyme Systems) supplemented with 10% FBS, on standard cell culture T75 flasks coated with FCN Coating Mix (Athena Enzyme Systems) as per the manufacturer's instructions.

All media formulations were supplemented with 100 µg/ml penicillin-streptomycin (Gibco 15-140-122).

### *Chromosome Conformation Capture (Hi-C)*

Cell pellets for chromosome conformation capture were prepared as previously described (Gollosi et al., 2018). Briefly, cells growing in monolayer in standard T75 flasks were quickly washed with 10 ml of HBSS (Gibco 14-025-134) at room temperature and crosslinked with 10 ml 1% formaldehyde (Fisher Bioreagents BP531-25, in HBSS) for 10 min on a shaking platform. The crosslinking reaction was quenched by adding glycine to a final concentration of 0.14 M (MP biomedical ICN19482591), followed by a 5 min incubation at room temperature, with

shaking. After cooling down the plates on ice for 15 min, the formaldehyde solution was aspirated from the plate and substituted with 10 ml of ice cold HBSS, containing 1X Halt Protease Inhibitor cocktail (Thermo PI78438). Five million cell aliquots were collected by centrifugation and snap frozen in liquid nitrogen.

VCaP, MDAPCa2a and PC3 Hi-C was conducted as described (Gollosi et al., 2018), using DpnII (New England Biolabs). Hi-C was also performed on LNCaP, DU145, VCaP, MDAPCa2a, MDAPCa2b and PC3, using the Arima Hi-C (Arima Genomics) kit, following the manufacturer's protocol A160141 v01 for library amplification using the NEBNext Ultra II kit (NEB E7645S). Sequencing was performed by Genewiz (South Plainfield, NJ) on either an Illumina NovaSeq or HiSeq platform with 50 or 150 bp paired end reads. Sequenced reads were mapped to a reference human genome (hg19), binned, and iteratively corrected according to established pipelines (Imakaev et al., 2012) using the dekkerlab-cMapping tool available at <https://github.com/dekkerlab/cMapping>.

In addition, the same analysis above was performed on fastq files from previously published Hi-C datasets for RWPE, 22RV1 and LNCaP C4-2B: GSE118629 and GSE73782 (Rhie et al., 2019, Luo et al., 2017b). See Supplementary Table 1 for all data sources and statistics. Newly generated LNCaP results were checked for consistency with previously published LNCaP Hi-C results (ENCSR346DCU, Taberlay et al., 2016). Since our LNCaP data had a dramatically higher cis/trans ratio than these previously published datasets, comparisons were difficult, and so we proceeded with only our newly generated data.

#### *Analysis of Hi-C data*

All Hi-C data analysis was carried out using the existing cworld-dekker pipeline, available on github (<https://github.com/dekkerlab/cworld-dekker>) as follows:

Hi-C heatmaps were generated for genome-wide datasets at a 2.5 Mb resolution, and per chromosome at a 250kb resolution, using the heatmap script.

Compartment analysis was performed via principal component analysis on 250 kb binned matrices using the matrix2compartment script. Positive and negative PC1 values were assigned to A and B compartments, respectively.

The PC1 values per bin for the normal epithelial cell line (RWPE) were subtracted from the values from each cancer cell line, resulting in a normalized distribution (referred to as  $\Delta$ PC1analysis). Significant changes in compartment identity were defined as those bins whose subtracted value fell either under the mean minus 1.5 the standard deviation or the mean plus 1.5 the standard deviation, for at least six cell lines or all four cells lines in the primary axis, as defined by nearest neighbor analysis as described below (SPRING plot).

The genes contained in regions of interest determined from the  $\Delta$ PC1 analysis were annotated using the knownGene primary table as referenced in UCSC Genome Browser. (<https://genome.ucsc.edu/>).

To facilitate the visualization of chromatin compartmentalization, heatmaps for cis interactions were generated by first calculating the Z score of the interactions at 250 kb resolution

compared to an expected interaction at each distance from the diagonal and then taking the Pearson correlation of each row and column of the heatmap (zScore correlation matrices). Multi compartment track figures and overlays were constructed using the visualization tool Sushi (Phanstiel et al., 2014)

Genome wide topologically associating domain (TAD) boundaries were determined using the matrix2insulation script on 40kb binned matrices, following the insulation score approach with an insulation square size of 500 kb (Crane et al., 2015).

#### *Calculation of A-A and B-B compartment interaction strengths*

To calculate A-A and B-B compartment interaction strengths for each chromosome distance corrected Hi-C intra-chromosomal interaction frequencies at 250 Kb resolution was reordered according to their corresponding PC1 values (from strongest B to strongest A). Then, the reordered intra-chromosomal interaction matrix was smoothed at 500 Kb resolution. Interactions were classified as A-A, B-B and A-B and thresholded to include only the top 20% of interactions. The median value of each A-A, B-B and A-B interactions is calculated. Finally, the relative A-A and B-B compartment interaction strengths were obtained by subtracting the absolute A-B compartment interaction strength from the absolute A-A and B-B interaction compartment strengths respectively.

For the average compartment interaction strength, the mean of the relative A-A and B-B interaction compartment strengths was calculated. A stronger A-A or B-B compartmentalization level compared to the A-B compartment intermixing would produce a higher positive value. On the other hand, a value close to zero suggests a weaker level of compartmentalization.

#### *SPRING Plot*

To construct the SPRING plot of the prostate cancer cells based on the Hi-C compartmental data, the compartment profile of the cells at the 250 Kb resolution was binarized. For example, the genomic regions where the compartment strength are greater than '0', were converted to '1' and the negative strengths to '-1'. The reason behind using that discretization step was to only consider the A/B compartment signature irrespective of the compartment strength. Once binarized, the data was then organized in a matrix format, where the rows are the genomic regions and columns are cells and principal component analysis (PCA) was performed on that data. Since we were dealing with a small set of samples (cells) for our analysis, we kept all the principal components from the PCA transformation for further analysis. Then, a k-nearest neighbor graph with 2 nearest neighbors (includes the node itself) was constructed from the PCA transformed data and the network was visualized with a force-directed layout.

#### *Microarray*

RNA was purified from 5 million cells at three different passages, per cell line, using the RNEasy mini kit (Qiagen 74104) using QIAshredder (Qiagen 79654) for homogenization. Purification was followed up by cleanup, and concentration using the RNase-Free DNase Set (Qiagen 79254) and

QIAquick PCR Purification Kit (Qiagen 28104), respectively. RNA concentration was determined using a NanoDrop One (Thermo).

Clariom S microarray was carried out through the Transcriptome Analysis Services (Transcriptome Profiling), from Thermo Fisher Scientific.

In addition, for cross-validation purposes, data for HG-U133 Plus2 microarray was also collected from ENCODE, as follows: RWPE (GSM966512, GSM966513, GSM966514), LNCaP (GSM2571978, GSM2571979, GSM2571980), DU145 (GSM1374469), PC3 (GSM1517530, GSM1517531, GSM1517532), LNCaP-C4-2B (GSM1565257, GSM1565258), and 22RV1 (GSM2571966, GSM2571967, GSM2571968).

Analysis of Microarray data was performed using the Transcription Analysis Console (TAC) from Applied Biosystems (Thermo Fisher Scientific), curating the log<sub>2</sub> fold upregulated/downregulated genes ( $p < 0.05$ ) with targets identified in the  $\Delta$ PC1 analysis.

## Results

*Hi-C reveals distinct changes in the 3D genome structure of a cohort of cell lines that model prostate cancer progression.*

To determine how the genome's organization is affected by disease stage, we selected a cohort of nine cell lines that model the progression of prostate cancer, as follows: RWPE1 (Bello et al., 1997) was used to represent normal epithelium. LNCaP (Horoszewicz et al., 1983), originally isolated from lymph node metastasis, was used as an early adenocarcinoma model. VCaP (Korenchuk et al., 2001) and MDaPCa2a/b (Navone et al., 1997) were used as models for prototypical osteoblastic bone metastasis; these cells are Caucasian and African American origins, respectively. 22RV1 (Sramkoski et al., 1999) and LNCaP C4-2B (Thalmann et al., 2000) were included in the study as cells that, although isolated from human sources, are models of murine bone metastasis. Atypical metastatic cell lines used in this study include PC3 (Kaighn et al., 1979) (osteoclastic and androgen-independent) and Du145 (Stone et al., 1978) (brain metastasis) (Fig 1).

Hi-C was performed in cells under normal cell culture conditions (Methods) on five million cell pellets. Additionally, publicly available datasets for RWPE and LNCaP-C42B were used as comparisons (Rhie et al., 2019, Taberlay et al., 2016). Hi-C mapping and quality control statistics for all samples can be found in Sup. Fig. 1.

The frequency of chromosome contacts is represented in a heatmap where the XY axes are the chromosomal coordinates. The color intensity reflects the frequency with which two particular locations were found to be in contact. At a resolution of 1 megabase (Mb) bins, the Hi-C heatmaps reveal chromosome territories. At a 250-kilobase (kb) resolution, it is possible to see a plaid pattern of interaction strength, which represents the spatial segregation of A and B compartments. We classify each genomic region as belonging to the A or B compartment using principal component analysis. Positive values of the first eigenvector (eigen1) represent A compartment regions (typically open euchromatin) while negative values denote B compartment (heterochromatin). Finally, at 40 kb resolution, distinct topologically associating

domains (TADs) are evident, which are regions of enhanced contacts (which may promote contacts between promoters and enhancers) segregated by the insulator protein CTCF (Fig. 2A).

Whole-genome contact maps for cells in our model reveal that the highest incidence of interactions occurs in cis: chromosomes primarily interacting within themselves (Fig 2B, C, D, E). Chromosomal translocations are evident as very strong interactions occurring in trans between different chromosomes. Comparing our Hi-C results with published spectral karyotyping (SKY) data (Pan et al., 1999, van Bokhoven et al., 2003) and karyotyping information from ATCC, we found that our Hi-C data detects 84% of all previously reported translocations. Owing to the high resolution of Hi-C data, we also characterized several previously unreported, smaller translocation events (Sup. Fig. 2). Interestingly, chromosomal territories remain well defined throughout progression, with subtle changes in intrachromosomal interactions, as shown in 250 Kb-resolution heatmaps of each chromosome (Sup. Fig. 3).

*Genes important to prostate cancer progression switch chromatin compartment identity, and these changes are accompanied by transcription activation.*

Examination of higher resolution (250 kb) z-score correlation heatmaps of cis interactions for each chromosome shows that the characteristic plaid contact pattern, associated with spatial compartment identity, changes among cell lines. For example, for chromosome X, an erosion of the pattern is observed in the bone metastatic cell line VCaP compared to the normal epithelium (RWPE). In contrast, the patterning observed in the model cell line for adenocarcinoma (LNCaP) and the bone metastatic MDAPCa2a line is more similar for chrX (Fig.3A). These patterns can be observed throughout all chromosomes, and the changes in compartmentalization are specific to each cell line (Sup. Fig.4). Motivated by the visible compartment “erosion” in VCaP, we quantified the overall strength of interactions within A compartment regions and within B compartment regions in the different cell types. We find that all prostate cancer cell lines show a loss of A compartment interaction strength relative to RWPE, reflecting an increased intermixing of the A compartment with B compartment regions. Meanwhile, B compartment strength experiences less change in LNCaP and VCaP and even increases in MDAPCa cell lines. Overall, this leads to an imbalance of B and A compartment strength in all prostate cancer cell lines (Sup. Fig. 5A).

Systematic analysis of the A/B compartment tracks, per chromosome, for all the cell lines in our model, revealed regions where the compartment identity remained the same and where it was changed (Sup. Fig. 5B and 6). From the contact maps, it is evident that some chromosomes in some cell lines are broken into multiple pieces (Sup. Fig. 7). However, when we perform compartment analysis on each of these broken pieces separately, we find that their underlying A/B compartmentalization is largely similar to cell lines with unbroken chromosomes. We note that there is a general level of similarity between epithelial-derived cell lines (Sup. Fig. 5B). By comparing compartment tracks for each cancer cell line to the normal control (RWPE), we find that the changes among cell lines are specific and localized. For example, eigenvector tracks for chromosome 21 show three distinct hotspots of compartment identity switches between the RWPE and cancer cell lines (Fig 3B). Interestingly, the right-most region encompasses the

TMPRSS2-ERG locus, a local translocation site that correlates with worse progression and metastasis in prostate cancer (Tomlins et al., 2005, Demichelis et al., 2007, Hagglof et al., 2014).

A comparison of genome-wide compartment tracks for all cell lines by nearest neighbor analysis (SPRING Plot, see Methods) revealed that LNCaP is a central node in a model axis to metastasis (Fig. 3C, axis highlighted in yellow), connecting RWPE (normal epithelium) to bone metastatic cell lines (VCaP and MDAPCa). Interestingly, the compartment pattern of MDAPCa2A and 2B, which were derived from an African American patient, is distinct from VCaP, which is of Caucasian lineage. This analysis also clusters atypical metastatic lines DU145 and PC3 together along a third axis radiating from the LNCaP central node.

To consistently mathematically classify regions that significantly changed compartments between cell lines, PC1 values per bin per cell line were normalized by subtracting the corresponding value derived from the normal RWPE cell line. Significant changes in compartment identity ( $|\bar{X} + 1.5\sigma|$ ) were identified, and the corresponding genomic areas annotated (Sup. Fig. 8). Through this analysis, we have identified 181 genomic bins (250 kb in size) whose compartmentalization changes from the B to the A compartment in either (a) six or more cancer cell lines compared to RWPE or (b) in all cells in the progression axis, compared to RWPE. These genomic bins contain about three hundred genes that are therefore moving from the B to the A compartment (Sup. Table 2), suggesting that these genes become more likely to be transcribed. These include androgen receptor (AR), WNT5A, CDK14, and genes located close to TMPRSS2, such as BACE2. The majority of these genes (256) are grouped in forty-eight proximal clusters (Sup. Table 3). We have also identified eighty-six genes whose genomic loci switch compartments from the A to B compartment, suggesting a genome structure rearrangement more likely to result in gene silencing (Sup. Table 2). Such is the case for certain cadherins, annexins, and mediators of inflammation. Of these genes, sixty-four are grouped in sixteen clusters (Sup. Table 3).

Since a switch from the B to A compartment could signify transcriptional activation, we used the Clariom-S microarray to profile expression levels in the targets identified. Using the expression level of RWPE as a baseline, we have found that forty-seven percent of genes that switch from B to A compartment show a significant transcriptional induction in LNCaP (2-fold or higher). In turn, forty-nine percent of those genes are even further upregulated in VCaP compared to LNCaP, suggesting an exacerbation of this expression pattern with progression. These genes include, among others, androgen receptor (AR), TMPRSS2, CDK14, and WNT5a. (Fig. 4A). In contrast, only 18% of the genes that show induction in LNCaP are induced further in the MDAPCa cell lines. (Fig. 4B).

Finally, we found that 25 genes that underwent a B to A compartment switch show transcriptional induction in both MDAPCa cell lines relative to VCaP, including CDK14, WNT5a, and BACE2, which is a close neighbor of TMPRSS2. (Fig 4C). This data suggests that these transcriptional hotspots are common for osteoblastic metastatic cells and might be necessary for colonization and survival in a secondary bone site.



*Compartment identity switches are accompanied by distinct structural changes at the TAD level, including boundary shifts.*

Topologically associating domains (TADs) contribute to the 3D architecture of the genome by sequestering enhancers and promoters with their target genes, with a low likelihood of interaction across boundaries (Lupianez et al., 2015, Nora et al., 2012, Dixon et al., 2012). The disappearance of TAD boundaries has been identified as a potential activator of oncogenes (Hnisz et al., 2016). To analyze whether there are changes in 3D genomic structure at the local level surrounding genes associated with compartment identity switches, we used higher resolution Hi-C heatmaps (40Kb).

The WNT5a-ERC2 locus (Fig. 5 Cluster 1) is in the B compartment in normal epithelium, switching to the A compartment in all four members of the model axis to progression: LNCaP, VCaP, and both MDAPCa cell lines. While the right TAD boundary location is relatively consistent, the location of the left boundary shifts positions: In LNCaP, DU145, MDAPCa2B, and PC3, WNT5A localizes in a TAD with LRTM1 instead of ERC2. Interestingly, in VCaP, these three genes are clustered in the same TAD. FZD1 and CDK14, a receptor and activator cyclin of non-canonical WNT signaling, and which have been associated with the function of WNT5A, also switch to the A compartment (Fig. 5, Cluster 2). In this case, the genes are separated by a TAD boundary that rests atop the gene body of CDK14, but increased loops are evident on the separate TADs in the cancer cell lines, compared to normal epithelium. Remarkably, CDK14 is one of the genes whose transcription is consistently upregulated in all metastatic cell lines in the progression axis. TAD boundary shifting, appearance and disappearance were also observed in other clusters that switch compartment identity (Examples in Sup. Fig 9).

A detailed survey of all compartment-switched loci revealed five possible categories of changes in local structure. We classified all compartment switch regions into these categories. Strikingly, the androgen receptor locus, displays all five types of structure change across the different cell lines. First, a highly disorganized area (No TADs, uniformly distributed interactions across a region of the heatmap) becomes highly organized, or vice versa (Fig 6A). In AR, the gene is in the B compartment in RWPE, and the area around it is highly disorganized. With progression, the area becomes organized into TADs and sub-TADs for both LNCaP C4-2b and VCaP. The third type of structural conformation is the appearance of a high incidence of interactions along the edge the TAD (Fig. 6B). We call these interactions “loops” or “stalled loops” because these have previously been associated with the phenomenon of cohesin becoming stalled as it extrudes loops but encounters RNA polymerase, CTCF, or other barriers. This increased loop formation is evident at the AR locus in LNCaP, MDAPCa2a, and MDAPCa2b. The fourth structural feature is a complete absence of structure (loss of contacts in the entire region) associated with the gene of interest. This "structural desert" is observed at the AR locus in the 22RV1 cell line (Fig. 6C) and is reminiscent of previously observed structural features at highly transcribed long genes (Leidescher et al., 2020, Heinz et al., 2018). Finally, the local structure can remain unchanged. For AR, this is the case in PC3 and DU145, where the gene remains in a disorganized region of the B compartment (Fig. 6D).

Overall, for those genes that switch from the A to the B compartment, all types of changes happen with fairly even probability: 12.64% lose structure at the local level, 14.37% gain structure, 28.16% present stalled loops, 21.26% associate with structural deserts, and 23.56% do not change. However, genes located in the B to A compartment switches predominantly acquire structure (39.06%) or do not change (21.88%). Only about 3% of B to A switch loci lose structure. The remaining loci are distributed evenly between stalled loop-areas and structural desert change (Fig 6E). From this survey of prostate cancer cell lines, therefore, we also gain basic insight about the types of local structure change that most often accompany compartment level changes.

*The TMPRSS2-ERG locus shows an increase in local interactions in cell lines in the metastatic progression axis.*

As previously mentioned, the incidence of the TMPRSS2-ERG translocation has a positive correlation with prostate cancer progression and a poor prognosis. For the TMPRSS2-ERG locus, we observe that the region that encompasses TMPRSS2, BACE2, PLAC4, MX1, MX2, and FAM3B switches from the B compartment in RWPE to the A compartment in all cancer cell lines. In the model cell line for normal epithelium RWPE, this genomic area is enclosed in a large TAD, including genes downstream of TMPRSS2 (Fig. 7A), as is also the case for LNCaP, 22RV1, MDAPCa2a, and PC3, with a slight shifting of the TAD boundary location. In LNCaP-C42B, an osteoblastic cell line derived from LNCaP, a sub-TAD appears within this locus, sequestering the MX1 gene. Sub-TAD fragmentation also occurs in DU145, MDAPCa2b, and VCaP. In contrast, ERG is in the A compartment in RWPE (normal epithelium), switching to the B compartment only in LNCaP and MDAPCa2b. The TAD boundary location around ERG does not change. Of note, the whole genomic area surrounding these two clusters is located in the A compartment in VCaP, a known carrier of the TMPRSS2-ERG translocation, evident as a high interaction location in the Hi-C heatmap (Fig7A: VCaP-rectangle).

In the bone metastatic cell line VCaP the TMPRSS2-ERG translocation is apparent in the Hi-C heatmap of the long arm of chromosome 21 at a 250kb resolution (Figure 7B). While a translocation is not evident in the MDAPCa cell lines, there is a distinct higher incidence of interactions close to that area: a log<sub>2</sub> ratio comparison against normal epithelium (RWPE) shows that that chromosomal region is enriched for interactions in adenocarcinoma (LNCaP) (Fig 7C), and that this phenotype is aggravated in both bone metastatic MDAPCa cell lines.

## Discussion

The deliberate, hierarchical organization of chromatin within the eukaryotic nucleus's constrained space is necessary for adequate DNA maintenance, repair, and gene transcription or silencing, all of which contribute to the cell's homeostasis. In this study, we have characterized the genomic architecture in a cohort of cells that model prostate cancer progression. At the genome-wide level, given the inherent high resolution of Hi-C data, we have identified small translocations that, to our knowledge, have not previously been reported in the literature.

Many regions across the genome are unchanged in their spatial compartmentalization across cell lines. This suggests that there are inherent 3D genome structure features of prostate epithelium that arise during initial differentiation and tissue patterning (Flyamer et al., 2017, Ke et al., 2017), and that these are persistent, regardless of malignancy status. These results suggest that genomic loci that switch compartment identity between the normal epithelium and cancer cells are associated with an oncogenic genomic architecture profile and that those features result from concerted biological events.

It is noteworthy that the majority of the compartment changes we identify involve a switch from the B to the A compartment. Correspondingly, we find in our compartment strength analyses that the A compartment becomes more intermixed, interacting more broadly, while the strongest B compartment regions remain more spatially segregated in the cancer cell lines. Both of these results point to a general shift in the prostate cancer lines toward a more open / poised for activation chromatin environment, which could lead to misactivation of oncogenes.

Our genome-wide compartment analysis revealed that compartment identity alone is enough to stratify prostate epithelium in a continuum of progression. LNCaP is a central node that connects the normal epithelium (RWPE) to bone metastatic cell lines (MDAPCa2a/b and VCaP). These results provide further insight into the importance of cell line selection in progression studies: the atypical metastatic cell lines DU145 and PC3 cluster together away from the primary axis. This emphasizes that as researchers select cell lines for study, it is important to consider the differences in these cell lines and that not all will capture the most common pathways of metastasis.

It is important to consider that the compartment switching events observed here involve clusters of genes, that in some cases expand through several topologically associating domains (TADs). This observation echoes previous results in a plant system, where clusters of genes often changed their spatial compartmentalization and expression together (Nutzmann et al., 2020). Interestingly, the clusters we observe include both genes previously identified in prostate cancer progression and others seemingly unrelated. Such is the case of the WNT5a locus in which is a known target of both prostate tissue development, patterning, and cancer aggressiveness (Allgeier et al., 2008, Dai et al., 2008, Yamamoto et al., 2010, Huang et al., 2009). Our results show that in normal epithelium, WNT5a is sequestered within a TAD with the ELKS/RAB6-Interacting/CAST Family Member 2 (ERC2). In contrast, TAD boundary shifting or eviction in the proximity of WNT5a in the bone metastatic cell lines represented in our primary axis for progression (VCaP and MDAPCa2a/b) results in TAD-limited interactions with Leucine-rich repeats and transmembrane domains-containing protein 1 (LRTM1) instead. While this shift does not result in transcriptional induction of LRTM1, it could potentially lead to aberrant interactions between the promoters for both genes, ultimately resulting in the overexpression of WNT5a. Since TAD structure is essential for proper gene regulation (Lupianez et al., 2015, Rhie et al., 2019, Guo et al., 2018), this phenomenon requires further exploration. Still, it is attractive to consider TAD-targeted therapies that hold the potential to reverse the deleterious effects of TAD shifting. Interestingly, another target of non-canonical WNT signaling, CDK14

(reviewed by Davidson and Niehrs, 2010), also switches from the B to the A compartment and is transcriptionally activated in our metastatic axis.

The clustering of different genes in the described compartment switches raises the interesting question of whether certain genes could act as a driver of compartment identity switches while neighboring genes act as “passengers.” For example, the transcriptional activation of one gene could influence a whole genomic region to switch to the A compartment. Indeed, previous work has shown that binding of transcriptional activators can prefigure spatial compartment alterations (Stadhouders et al., 2018, Therizols et al., 2014). This compartment switch would then result in the switching of neighboring genes, which may increase their probability of later becoming activated as well. Recent work has shown that spatial reorganization of a chromosome region can make it more permissive for derepression, even if the structural switch does not immediately change its expression level (Manjón et al., 2021). Is it possible that earlier transcriptional events required for the cell to survive a particular insult trigger a full compartment shift? Is this, in turn, a potential trigger for oncogenic transcriptional activity? Such seems to be the case of the observed amyloid precursor protein (APP) – beta secretase 2 (BACE2) axis, along chromosome 21. APP presents with enhanced expression in the LNCaP – MDAPCa – VCaP axis, compared to the normal RWPE (Sup. Fig 10). APP is also proximal to one of the persistent compartment switches in chromosome 21, but it does not change compartment itself: The A compartment identity atop the gene gets stronger with progression. Mounting evidence from the Alzheimer's field, where abnormal amyloid processing results in aggregation and neurodegeneration, has shown that this protein and derived peptides serve a crucial role as antimicrobials and are necessary for mounting an appropriate host response to infection (thoroughly reviewed by Moir et al., 2018). If an environmental signal such as infection results in the prostate epithelium being exposed to excessive or chronic APP, could this trigger expression of its processing enzyme BACE2? Our evidence of BACE2 switched compartmentalization and experienced higher levels of transcription in all three prototypical bone metastatic lines suggests so. Critically, these events would imply the need for the compartment switch around the TMPRSS2 locus.

Since its discovery, the TMPRSS2-ERG translocation in chromosome 21 has been recognized as an important indicator of poor prognosis and a higher risk of prostate cancer-related death (Tomlins et al., 2005, Perner et al., 2006, Demichelis et al., 2007, Hagglof et al., 2014, Deplus et al., 2017). The genesis of this translocation and fusion, however, remains poorly understood. Here, we implicate a 3D genome organization change of compartmentalization in this event. As mentioned before, TMPRSS2 switches from the B to the A compartment consistently in all prostate cancer cell lines we queried. Meanwhile, ERG switches from the A to the B compartment in LNCaP and its nearest neighbor in our experimental metastatic axis, MDAPCa2b. Remarkably, ERG remains in the A compartment for VCaP and MDAPCa2a, suggesting a potential dual switching event during progression to more aggressive phenotypes. All these spatial rearrangements in such proximity result in the enhanced contact incidence observed in all of these cell lines, even the early adenocarcinoma model LNCaP (as described in figure 7), and ultimately could lead to the translocation event, as it has been shown in other systems (McCord and Balajee, 2018, Zhang et al., 2012)

Recent efforts (Hawley et al., 2021), have characterized 3D genomic profiles in prostate tumor cohorts. These studies recapitulate our findings that the 3D genome organization between malignant and benign prostate tissues remains largely consistent. We propose that prostate cancer progression is associated with specific changes in the 3D genome structure that arise early in the disease and facilitate an oncogenic expression phenotype. Based on these results, we can hypothesize that analyzing the 3D genome structure of patient derived samples could be a prognostic marker for progression and bone metastasis.

## Acknowledgments

We thank Jeremy Hughes (Web Communications Manager – UTK Department of Arts & Sciences) for his help in constructing the accompanying website.

We thank Nora Navone Ph.D. for providing the MDAPCa cell lines. We thank Justin Roberts Ph.D. for technical support in the culturing of these cell lines.

We thank Rosela Gollosi Ph.D. and Jacob Sanders Ph.D. for their technical support.

This work was supported, in part, by the by NIH NIGMS grant R35GM133557 to R. P. McCord. R. San Martin was supported by a Postdoctoral Fellowship from the American Cancer Society (134060-PF-19-183-01-CSM). The authors declare no competing financial interests.

## Data Availability

All Hi-C and microarray data are available on GEO at accession number GSE172099. Other processed data figures, and a UCSC Genome Browser Track Hub containing all data are available for browsing at <https://3dgenome.utk.edu/3d-genome-architecture-in-prostate-cancer-progression/>.

## Author Contributions

*Conceptualization:* R. San Martin and R. P. McCord; *Investigation:* R. San Martin. *Formal analysis:* R. San Martin, R. P. McCord P. Das and R. Dos Reis Marques; *Visualization:* R. San Martin, Y. Xu and R. Dos Reis Marques; *Writing – original draft:* R. San Martin and R. P. McCord; *Software:* P. Das and Y. Xu *Writing – review and editing:* all authors; *Supervision,* R. P. McCord.

## References

- AHMADIYEH, N., POMERANTZ, M. M., GRISANZIO, C., HERMAN, P., JIA, L., ALMENDRO, V., HE, H. H., BROWN, M., LIU, X. S., DAVIS, M., CASWELL, J. L., BECKWITH, C. A., HILLS, A., MACCONAILL, L., COETZEE, G. A., REGAN, M. M. & FREEDMAN, M. L. 2010. 8q24 prostate, breast, and colon cancer risk loci show tissue-specific long-range interaction with *MYC*. *Proceedings of the National Academy of Sciences*, 107, 9742-9746.
- ALLGEIER, S. H., LIN, T. M., VEZINA, C. M., MOORE, R. W., FRITZ, W. A., CHIU, S. Y., ZHANG, C. & PETERSON, R. E. 2008. WNT5A selectively inhibits mouse ventral prostate development. *Dev Biol*, 324, 10-7.
- BALAJEE, A. S., SANDERS, J. T., GOLLOSHI, R., SHURYAK, I., MCCORD, R. P. & DAINIAK, N. 2018. Investigation of Spatial Organization of Chromosome Territories in Chromosome Exchange Aberrations After Ionizing Radiation Exposure. *Health Phys*, 115, 77-89.
- BARBAZAN, J., ALONSO-ALCONADA, L., ELKHATIB, N., GERALDO, S., GURCHENKOV, V., GLENTIS, A., VAN NIEL, G., PALMULLI, R., FERNANDEZ, B., VIANO, P., GARCIA-CABALLERO, T., LOPEZ-LOPEZ, R., ABAL, M. & VIGNJEVIC, D. M. 2017. Liver Metastasis Is Facilitated by the Adherence of Circulating Tumor Cells to Vascular Fibronectin Deposits. *Cancer Res*, 77, 3431-3441.
- BARUTCU, A. R., LAJOIE, B. R., MCCORD, R. P., TYE, C. E., HONG, D., MESSIER, T. L., BROWNE, G., VAN WIJNEN, A. J., LIAN, J. B., STEIN, J. L., DEKKER, J., IMBALZANO, A. N. & STEIN, G. S. 2015. Chromatin interaction analysis reveals changes in small chromosome and telomere clustering between epithelial and breast cancer cells. *Genome Biol*, 16, 214.
- BELLO, D., WEBBER, M. M., KLEINMAN, H. K., WARTINGER, D. D. & RHIM, J. S. 1997. Androgen responsive adult human prostatic epithelial cell lines immortalized by human papillomavirus 18. *Carcinogenesis*, 18, 1215-23.
- BERGEMAN, J., CAILLIER, A., HOULE, F., GAGNE, L. M. & HUOT, M. E. 2016. Localized translation regulates cell adhesion and transendothelial migration. *J Cell Sci*, 129, 4105-4117.
- BUBENDORF, L., SCHOPFER, A., WAGNER, U., SAUTER, G., MOCH, H., WILLI, N., GASSER, T. C. & MIHATSCH, M. J. 2000. Metastatic patterns of prostate cancer: an autopsy study of 1,589 patients. *Hum Pathol*, 31, 578-83.
- CRANE, E., BIAN, Q., MCCORD, R. P., LAJOIE, B. R., WHEELER, B. S., RALSTON, E. J., UZAWA, S., DEKKER, J. & MEYER, B. J. 2015. Condensin-driven remodelling of X chromosome topology during dosage compensation. *Nature*, 523, 240-4.
- DAI, J., HALL, C. L., ESCARA-WILKE, J., MIZOKAMI, A., KELLER, J. M. & KELLER, E. T. 2008. Prostate cancer induces bone metastasis through Wnt-induced bone morphogenetic protein-dependent and independent mechanisms. *Cancer Res*, 68, 5785-94.
- DANILA, D. C., HELLER, G., GIGNAC, G. A., GONZALEZ-ESPINOZA, R., ANAND, A., TANAKA, E., LILJA, H., SCHWARTZ, L., LARSON, S., FLEISHER, M. & SCHER, H. I. 2007. Circulating tumor cell number and prognosis in progressive castration-resistant prostate cancer. *Clin Cancer Res*, 13, 7053-8.
- DAVIDSON, G. & NIEHRS, C. 2010. Emerging links between CDK cell cycle regulators and Wnt signaling. *Trends Cell Biol*, 20, 453-60.
- DAVIDSON, P. M., DENAIS, C., BAKSHI, M. C. & LAMMERDING, J. 2014. Nuclear deformability constitutes a rate-limiting step during cell migration in 3-D environments. *Cell Mol Bioeng*, 7, 293-306.
- DEKKER, J. & MIRNY, L. 2016. The 3D Genome as Moderator of Chromosomal Communication. *Cell*, 164, 1110-1121.
- DEMICHELI, F., FALL, K., PERNER, S., ANDREN, O., SCHMIDT, F., SETLUR, S. R., HOSHIDA, Y., MOSQUERA, J. M., PAWITAN, Y., LEE, C., ADAMI, H. O., MUCCI, L. A., KANTOFF, P. W., ANDERSSON, S. O., CHINNAIYAN, A. M., JOHANSSON, J. E. & RUBIN, M. A. 2007. TMPRSS2:ERG gene fusion associated with lethal prostate cancer in a watchful waiting cohort. *Oncogene*, 26, 4596-9.
- DEPLUS, R., DELLIAUX, C., MARCHAND, N., FLOURENS, A., VANPOUILLE, N., LEROY, X., DE LAUNOIT, Y. & DUTERQUE-COQUILLAUD, M. 2017. TMPRSS2-ERG fusion promotes prostate cancer metastases in bone. *Oncotarget*, 8, 11827-11840.
- DIAMOND, D. A., BERRY, S. J., JEWETT, H. J., EGGLESTON, J. C. & COFFEY, D. S. 1982. A new method to assess metastatic potential of human prostate cancer: relative nuclear roundness. *J Urol*, 128, 729-34.

- DIXON, J. R., SELVARAJ, S., YUE, F., KIM, A., LI, Y., SHEN, Y., HU, M., LIU, J. S. & REN, B. 2012. Topological domains in mammalian genomes identified by analysis of chromatin interactions. *Nature*, 485, 376-80.
- DU, M., TILLMANS, L., GAO, J., GAO, P., YUAN, T., DITTMAR, R. L., SONG, W., YANG, Y., SAHR, N., WANG, T., WEI, G.-H., THIBODEAU, S. N. & WANG, L. 2016. Chromatin interactions and candidate genes at ten prostate cancer risk loci. *Scientific Reports*, 6, 23202.
- ENGREITZ, J. M., AGARWALA, V. & MIRNY, L. A. 2012. Three-dimensional genome architecture influences partner selection for chromosomal translocations in human disease. *PLoS One*, 7, e44196.
- FLYAMER, I. M., GASSLER, J., IMAKAEV, M., BRANDAO, H. B., ULIANOV, S. V., ABDENNUR, N., RAZIN, S. V., MIRNY, L. A. & TACHIBANA-KONWALSKI, K. 2017. Single-nucleus Hi-C reveals unique chromatin reorganization at oocyte-to-zygote transition. *Nature*, 544, 110-114.
- GERLITZ, G. & BUSTIN, M. 2010. Efficient cell migration requires global chromatin condensation. *J Cell Sci*, 123, 2207-17.
- GOLLOSHI, R., SANDERS, J. T. & MCCORD, R. P. 2018. Iteratively improving Hi-C experiments one step at a time. *Methods*, 142, 47-58.
- GUO, Y., PEREZ, A. A., HAZELETT, D. J., COETZEE, G. A., RHIE, S. K. & FARNHAM, P. J. 2018. CRISPR-mediated deletion of prostate cancer risk-associated CTCF loop anchors identifies repressive chromatin loops. *Genome Biology*, 19, 160.
- HAGGLOF, C., HAMMARSTEN, P., STROMVALL, K., EGEVAD, L., JOSEFSSON, A., STATTIN, P., GRANFORS, T. & BERGH, A. 2014. TMPRSS2-ERG expression predicts prostate cancer survival and associates with stromal biomarkers. *PLoS One*, 9, e86824.
- HATCH, E. M. & HETZER, M. W. 2016. Nuclear envelope rupture is induced by actin-based nucleus confinement. *J Cell Biol*, 215, 27-36.
- HAWLEY, J. R., ZHOU, S., ARLIDGE, C., GRILLO, G., KRON, K., HUGH-WHITE, R., VAN DER KWAST, T., FRASER, M., BOUTROS, P. C., BRISTOW, R. G. & LUPIEN, M. 2021. *Cis*-regulatory Element Hijacking Overshadows Topological Changes in Prostate Cancer. 2021.01.05.425333.
- HEINZ, S., TEXARI, L., HAYES, M. G. B., URBANOWSKI, M., CHANG, M. W., GIVARKES, N., RIALDI, A., WHITE, K. M., ALBRECHT, R. A., PACHE, L., MARAZZI, I., GARCIA-SASTRE, A., SHAW, M. L. & BENNER, C. 2018. Transcription Elongation Can Affect Genome 3D Structure. *Cell*, 174, 1522-1536 e22.
- HELFAND, B. T., ROEHL, K. A., COOPER, P. R., MCGUIRE, B. B., FITZGERALD, L. M., CANCEL-TASSIN, G., CORNU, J. N., BAUER, S., VAN BLARIGAN, E. L., CHEN, X., DUGGAN, D., OSTRANDER, E. A., GWO-SHU, M., ZHANG, Z. F., CHANG, S. C., JEONG, S., FONTHAM, E. T., SMITH, G., MOHLER, J. L., BERNDT, S. I., MCDONNELL, S. K., KITTLES, R., RYBICKI, B. A., FREEDMAN, M., KANTOFF, P. W., POMERANTZ, M., BREYER, J. P., SMITH, J. R., REBBECK, T. R., MERCOLA, D., ISAACS, W. B., WIKLUND, F., CUSSENOT, O., THIBODEAU, S. N., SCHAID, D. J., CANNON-ALBRIGHT, L., COONEY, K. A., CHANOCK, S. J., STANFORD, J. L., CHAN, J. M., WITTE, J., XU, J., BENSEN, J. T., TAYLOR, J. A. & CATALONA, W. J. 2015. Associations of prostate cancer risk variants with disease aggressiveness: results of the NCI-SPORE Genetics Working Group analysis of 18,343 cases. *Hum Genet*, 134, 439-50.
- HERNANDEZ, R. K., WADE, S. W., REICH, A., PIROLI, M., LIEDE, A. & LYMAN, G. H. 2018. Incidence of bone metastases in patients with solid tumors: analysis of oncology electronic medical records in the United States. *BMC Cancer*, 18, 44.
- HNISZ, D., WEINTRAUB, A. S., DAY, D. S., VALTON, A. L., BAK, R. O., LI, C. H., GOLDMANN, J., LAJOIE, B. R., FAN, Z. P., SIGOVA, A. A., REDDY, J., BORGES-RIVERA, D., LEE, T. I., JAENISCH, R., PORTEUS, M. H., DEKKER, J. & YOUNG, R. A. 2016. Activation of proto-oncogenes by disruption of chromosome neighborhoods. *Science*, 351, 1454-1458.
- HOROSZEWICZ, J. S., LEONG, S. S., KAWINSKI, E., KARR, J. P., ROSENTHAL, H., CHU, T. M., MIRAND, E. A. & MURPHY, G. P. 1983. LNCaP model of human prostatic carcinoma. *Cancer Res*, 43, 1809-18.
- HUANG, L., PU, Y., HU, W. Y., BIRCH, L., LUCCIO-CAMELO, D., YAMAGUCHI, T. & PRINS, G. S. 2009. The role of Wnt5a in prostate gland development. *Dev Biol*, 328, 188-99.
- IMAKAEV, M., FUDENBERG, G., MCCORD, R. P., NAUMOVA, N., GOLOBORODKO, A., LAJOIE, B. R., DEKKER, J. & MIRNY, L. A. 2012. Iterative correction of Hi-C data reveals hallmarks of chromosome organization. *Nat Methods*, 9, 999-1003.
- JACOBS, S. C. 1983. Spread of prostatic cancer to bone. *Urology*, 21, 337-44.
- KAIGHN, M. E., NARAYAN, K. S., OHNUKI, Y., LECHNER, J. F. & JONES, L. W. 1979. Establishment and characterization of a human prostatic carcinoma cell line (PC-3). *Invest Urol*, 17, 16-23.



- KE, Y., XU, Y., CHEN, X., FENG, S., LIU, Z., SUN, Y., YAO, X., LI, F., ZHU, W., GAO, L., CHEN, H., DU, Z., XIE, W., XU, X., HUANG, X. & LIU, J. 2017. 3D Chromatin Structures of Mature Gametes and Structural Reprogramming during Mammalian Embryogenesis. *Cell*, 170, 367-381 e20.
- KORENCHUK, S., LEHR, J. E., L, M. C., LEE, Y. G., WHITNEY, S., VESSELLA, R., LIN, D. L. & PIENTA, K. J. 2001. VCaP, a cell-based model system of human prostate cancer. *In Vivo*, 15, 163-8.
- LAMMERDING, J., FONG, L. G., JI, J. Y., REUE, K., STEWART, C. L., YOUNG, S. G. & LEE, R. T. 2006. Lamins A and C but not lamin B1 regulate nuclear mechanics. *J Biol Chem*, 281, 25768-80.
- LEIDESCHER, S., NÜBLER, J., FEODOROVA, Y., HILDEBRAND, E., ULLRICH, S., BULTMANN, S., LINK, S., THANISCH, K., DEKKER, J., LEONHARDT, H., MIRNY, L. & SOLOVEI, I. 2020. SPATIAL ORGANIZATION OF TRANSCRIBED EUKARYOTIC GENES. 2020.05.20.106591.
- LIEBERMAN-AIDEN, E., VAN BERKUM, N. L., WILLIAMS, L., IMAKAEV, M., RAGOCZY, T., TELLING, A., AMIT, I., LAJOIE, B. R., SABO, P. J., DORSCHNER, M. O., SANDSTROM, R., BERNSTEIN, B., BENDER, M. A., GROUDINE, M., GNIRKE, A., STAMATOYANNOPOULOS, J., MIRNY, L. A., LANDER, E. S. & DEKKER, J. 2009. Comprehensive mapping of long-range interactions reveals folding principles of the human genome. *Science*, 326, 289-93.
- LUO, Z., RHIE, S. K., LAY, F. D. & FARNHAM, P. J. 2017a. A Prostate Cancer Risk Element Functions as a Repressive Loop that Regulates HOXA13. *Cell Reports*, 21, 1411-1417.
- LUO, Z., RHIE, S. K., LAY, F. D. & FARNHAM, P. J. 2017b. A Prostate Cancer Risk Element Functions as a Repressive Loop that Regulates HOXA13. *Cell Rep*, 21, 1411-1417.
- LUPIANEZ, D. G., KRAFT, K., HEINRICH, V., KRAWITZ, P., BRANCATI, F., KLOPOCKI, E., HORN, D., KAYSERILI, H., OPITZ, J. M., LAXOVA, R., SANTOS-SIMARRO, F., GILBERT-DUSSARDIER, B., WITTLER, L., BORSCHIWER, M., HAAS, S. A., OSTERWALDER, M., FRANKE, M., TIMMERMANN, B., HECHT, J., SPIELMANN, M., VISEL, A. & MUNDLOS, S. 2015. Disruptions of topological chromatin domains cause pathogenic rewiring of gene-enhancer interactions. *Cell*, 161, 1012-1025.
- MANJÓN, A. G., HUPKES, D. P., LIU, N. Q., FRISKES, A., JOOSTEN, S., TEUNISSEN, H., AARTS, M., PREKOVIC, S., ZWART, W., DE WIT, E., VAN STEENSEL, B. & MEDEMA, R. H. 2021. Perturbations in 3D genome organization can promote acquired drug resistance. 2021.02.02.429315.
- MCCORD, R. P. & BALAJEE, A. 2018. 3D Genome Organization Influences the Chromosome Translocation Pattern. *Adv Exp Med Biol*, 1044, 113-133.
- MEABURN, K. J. & MISTELI, T. 2007. Cell biology: chromosome territories. *Nature*, 445, 379-781.
- MIERKE, C. T. 2008. Role of the endothelium during tumor cell metastasis: is the endothelium a barrier or a promoter for cell invasion and metastasis? *J Biophys*, 2008, 183516.
- MOIR, R. D., LATHE, R. & TANZI, R. E. 2018. The antimicrobial protection hypothesis of Alzheimer's disease. *Alzheimers Dement*, 14, 1602-1614.
- MORENO, J. G., MILLER, M. C., GROSS, S., ALLARD, W. J., GOMELLA, L. G. & TERSTAPPEN, L. W. 2005. Circulating tumor cells predict survival in patients with metastatic prostate cancer. *Urology*, 65, 713-8.
- NAVONE, N. M., OLIVE, M., OZEN, M., DAVIS, R., TRONCOSO, P., TU, S. M., JOHNSTON, D., POLLACK, A., PATHAK, S., VON ESCHENBACH, A. C. & LOGOTHETIS, C. J. 1997. Establishment of two human prostate cancer cell lines derived from a single bone metastasis. *Clin Cancer Res*, 3, 2493-500.
- NORA, E. P., GOLOBORODKO, A., VALTON, A. L., GIBBUS, J. H., UEBERSOHN, A., ABDENNUR, N., DEKKER, J., MIRNY, L. A. & BRUNEAU, B. G. 2017. Targeted Degradation of CTCF Decouples Local Insulation of Chromosome Domains from Genomic Compartmentalization. *Cell*, 169, 930-944 e22.
- NORA, E. P., LAJOIE, B. R., SCHULZ, E. G., GIORGETTI, L., OKAMOTO, I., SERVANT, N., PILOT, T., VAN BERKUM, N. L., MEISIG, J., SEDAT, J., GRIBNAU, J., BARILLOT, E., BLUTHGEN, N., DEKKER, J. & HEARD, E. 2012. Spatial partitioning of the regulatory landscape of the X-inactivation centre. *Nature*, 485, 381-5.
- NUEBLER, J., FUDENBERG, G., IMAKAEV, M., ABDENNUR, N. & MIRNY, L. A. 2018. Chromatin organization by an interplay of loop extrusion and compartmental segregation. *Proc Natl Acad Sci U S A*, 115, E6697-E6706.
- NUTZMANN, H. W., DOERR, D., RAMIREZ-COLMENERO, A., SOTELO-FONSECA, J. E., WEGEL, E., DI STEFANO, M., WINGETT, S. W., FRASER, P., HURST, L., FERNANDEZ-VALVERDE, S. L. & OSBOURN, A. 2020. Active and repressed biosynthetic gene clusters have spatially distinct chromosome states. *Proc Natl Acad Sci U S A*, 117, 13800-13809.

- PAN, Y., KYTOLA, S., FARNEBO, F., WANG, N., LUI, W. O., NUPPONEN, N., ISOLA, J., VISAKORPI, T., BERGERHEIM, U. S. & LARSSON, C. 1999. Characterization of chromosomal abnormalities in prostate cancer cell lines by spectral karyotyping. *Cytogenet Cell Genet*, 87, 225-32.
- PARTIN, A. W., GETZENBERG, R. H., CARMICHAEL, M. J., VINDIVICH, D., YOO, J., EPSTEIN, J. I. & COFFEY, D. S. 1993. Nuclear matrix protein patterns in human benign prostatic hyperplasia and prostate cancer. *Cancer Res*, 53, 744-6.
- PERNER, S., DEMICHELIS, F., BEROUKHIM, R., SCHMIDT, F. H., MOSQUERA, J. M., SETLUR, S., TCHINDA, J., TOMLINS, S. A., HOFER, M. D., PIENTA, K. G., KUEFER, R., VESSELLA, R., SUN, X. W., MEYERSON, M., LEE, C., SELLERS, W. R., CHINNAIYAN, A. M. & RUBIN, M. A. 2006. TMPRSS2:ERG fusion-associated deletions provide insight into the heterogeneity of prostate cancer. *Cancer Res*, 66, 8337-41.
- PHANSTIEL, D. H., BOYLE, A. P., ARAYA, C. L. & SNYDER, M. P. 2014. Sushi.R: flexible, quantitative and integrative genomic visualizations for publication-quality multi-panel figures. *Bioinformatics*, 30, 2808-10.
- POPE, B. D., RYBA, T., DILEEP, V., YUE, F., WU, W., DENAS, O., VERA, D. L., WANG, Y., HANSEN, R. S., CANFIELD, T. K., THURMAN, R. E., CHENG, Y., GULSOY, G., DENNIS, J. H., SNYDER, M. P., STAMATOYANNOPOULOS, J. A., TAYLOR, J., HARDISON, R. C., KAHVECI, T., REN, B. & GILBERT, D. M. 2014. Topologically associating domains are stable units of replication-timing regulation. *Nature*, 515, 402-5.
- RHIE, S. K., PEREZ, A. A., LAY, F. D., SCHREINER, S., SHI, J., POLIN, J. & FARNHAM, P. J. 2019. A high-resolution 3D epigenomic map reveals insights into the creation of the prostate cancer transcriptome. *Nature Communications*, 10, 4154.
- RICKMAN, D. S., SOONG, T. D., MOSS, B., MOSQUERA, J. M., DLABAL, J., TERRY, S., MACDONALD, T. Y., TRIPODI, J., BUNTING, K., NAJFELD, V., DEMICHELIS, F., MELNICK, A. M., ELEMENTO, O. & RUBIN, M. A. 2012. Oncogene-mediated alterations in chromatin conformation. *Proceedings of the National Academy of Sciences of the United States of America*, 109, 9083-9088.
- SIEGEL, R. L., MILLER, K. D. & JEMAL, A. 2020. Cancer statistics, 2020. *CA Cancer J Clin*, 70, 7-30.
- SRAMKOSKI, R. M., PRETLOW, T. G., 2ND, GIACONIA, J. M., PRETLOW, T. P., SCHWARTZ, S., SY, M. S., MARENGO, S. R., RHIM, J. S., ZHANG, D. & JACOBBERGER, J. W. 1999. A new human prostate carcinoma cell line, 22Rv1. *In Vitro Cell Dev Biol Anim*, 35, 403-9.
- STADHOUDERS, R., VIDAL, E., SERRA, F., DI STEFANO, B., LE DILY, F., QUILEZ, J., GOMEZ, A., COLLOMBET, S., BERENQUER, C., CUARTERO, Y., HECHT, J., FILION, G. J., BEATO, M., MARTI-RENOM, M. A. & GRAF, T. 2018. Transcription factors orchestrate dynamic interplay between genome topology and gene regulation during cell reprogramming. *Nat Genet*, 50, 238-249.
- STEPHENS, A. D., LIU, P. Z., BANIGAN, E. J., ALMASSALHA, L. M., BACKMAN, V., ADAM, S. A., GOLDMAN, R. D. & MARKO, J. F. 2018. Chromatin histone modifications and rigidity affect nuclear morphology independent of lamins. *Mol Biol Cell*, 29, 220-233.
- STONE, K. R., MICKEY, D. D., WUNDERLI, H., MICKEY, G. H. & PAULSON, D. F. 1978. Isolation of a human prostate carcinoma cell line (DU 145). *Int J Cancer*, 21, 274-81.
- TABERLAY, P. C., ACHINGER-KAWECKA, J., LUN, A. T., BUSKE, F. A., SABIR, K., GOULD, C. M., ZOTENKO, E., BERT, S. A., GILES, K. A., BAUER, D. C., SMYTH, G. K., STIRZAKER, C., O'DONOGHUE, S. I. & CLARK, S. J. 2016. Three-dimensional disorganization of the cancer genome occurs coincident with long-range genetic and epigenetic alterations. *Genome Res*, 26, 719-31.
- THALMANN, G. N., SIKES, R. A., WU, T. T., DEGEORGES, A., CHANG, S. M., OZEN, M., PATHAK, S. & CHUNG, L. W. 2000. LNCaP progression model of human prostate cancer: androgen-independence and osseous metastasis. *Prostate*, 44, 91-103 Jul 1;44(2).
- THERIZOLS, P., ILLINGWORTH, R. S., COURILLEAU, C., BOYLE, S., WOOD, A. J. & BICKMORE, W. A. 2014. Chromatin decondensation is sufficient to alter nuclear organization in embryonic stem cells. *Science*, 346, 1238-42.
- TODENHOFER, T., PARK, E. S., DUFFY, S., DENG, X., JIN, C., ABDI, H., MA, H. & BLACK, P. C. 2016. Microfluidic enrichment of circulating tumor cells in patients with clinically localized prostate cancer. *Urol Oncol*, 34, 483 e9-483 e16.
- TOMLINS, S. A., RHODES, D. R., PERNER, S., DHANASEKARAN, S. M., MEHRA, R., SUN, X. W., VARAMBALLY, S., CAO, X., TCHINDA, J., KUEFER, R., LEE, C., MONTIE, J. E., SHAH, R. B., PIENTA, K. J., RUBIN, M. A. & CHINNAIYAN, A. M. 2005. Recurrent fusion of TMPRSS2 and ETS transcription factor genes in prostate cancer. *Science*, 310, 644-8.

- VAN BOKHOVEN, A., CAIRES, A., MARIA, M. D., SCHULTE, A. P., LUCIA, M. S., NORDEEN, S. K., MILLER, G. J. & VARELLA-GARCIA, M. 2003. Spectral karyotype (SKY) analysis of human prostate carcinoma cell lines. *Prostate*, 57, 226-44.
- VERDONE, J. E., PARSANA, P., VELTRI, R. W. & PIENTA, K. J. 2015. Epithelial-mesenchymal transition in prostate cancer is associated with quantifiable changes in nuclear structure. *Prostate*, 75, 218-24.
- YAMAMOTO, H., OUE, N., SATO, A., HASEGAWA, Y., MATSUBARA, A., YASUI, W. & KIKUCHI, A. 2010. Wnt5a signaling is involved in the aggressiveness of prostate cancer and expression of metalloproteinase. *Oncogene*, 29, 2036-46.
- ZHANG, Y., MCCORD, R. P., HO, Y. J., LAJOIE, B. R., HILDEBRAND, D. G., SIMON, A. C., BECKER, M. S., ALT, F. W. & DEKKER, J. 2012. Spatial organization of the mouse genome and its role in recurrent chromosomal translocations. *Cell*, 148, 908-21.
- ZHOU, E., ZHANG, B., ZHU, K., SCHAAFSMA, E., KUMAR, R. D. & CHENG, C. 2020. A TMPRSS2-ERG gene signature predicts prognosis of patients with prostate adenocarcinoma. *Clin Transl Med*, 10, e216.

**Figure 1. A cell line-based model for the progression of prostate cancer.**

Cell lines used in this study model different stages in the progression from normal epithelium (RWPE) to localized disease (LNCaP) to prostate cancer that has metastasized to bone (VCaP, MDAPCa2a, MDAPCa2b, PC3) or to an atypical site (DU145). Cell lines developed through mouse xenografts and androgen independent cell lines highlighted in italics and boldface, respectively.

**Figure 2. Chromosome conformation capture characterizes the hierarchical genome of each cell line.**

A) At 1 Mb resolution (left), Hi-C heatmaps reveal show defined chromosome territories along the diagonal. At 100 kb resolution a characteristic plaid pattern emerges: principal component analysis of this matrix reveals A/B chromosome compartmentalization (center). At 40 kb resolution, topologically associating domains (TADs), within compartments, become apparent (right).

2.5 Mb Hi-C heatmaps for RWPE (B), LNCaP (C), VCaP (D) and MDAPCa2a (E). Translocations between chromosomes appear as high interaction frequency areas away from the diagonal. Translocation between chromosomes 8 and 5 highlighted as an example in RWPE (circle). While these translocation events have been validated by SKY analysis, the high resolution of Hi-C data allows for the characterization of smaller events (Sup. Fig. 2).

**Figure 3. Changes in A/B compartment identity are relevant to prostate cancer progression.**

A) 250 kb resolution z-score correlation heatmaps of cis interactions along the X chromosome show a characteristic plaid pattern that denotes compartment identity (compartments classified by PC1 of this matrix: green = A, red = B). A weakening of this pattern is observed in the bone metastatic cell line VCaP when compared to normal epithelium (RWPE). Similar patterning is observed in the model cell line for adenocarcinoma (LNCaP) and the bone metastatic MDAPCa2a line.

B) PC1 compartment tracks for chromosome 21 show distinct hotspots of compartment identity switches (boxes) along the chromosome between the normal epithelium (RWPE) and bone metastatic cell lines. The right-most region encompasses the TMPRSS2-ERG locus.

C) A comparison of genome-wide compartment tracks for all cell lines by nearest neighbor analysis reveals that LNCaP is a central node in a model axis to metastasis (highlighted yellow), connecting RWPE (normal epithelium) to bone metastatic cell lines (VCaP and MDA cell lines). Atypical androgen independent lines cluster together along a different axis from LNCaP.

**Figure 4. Microarray: genes whose increased expression correlates with changes in B to A compartment identity.**

A) 143 genes identified as switching from the B to the A compartment show overexpression in LNCaP when compared to RWPE (purple). Of these, 70 are further overexpressed in VCaP (green) compared to LNCaP, denoting an exacerbation of this expression pattern with progression. This overlapping gene set includes known prostate cancer targets such as androgen receptor (AR) and TMPRSS2.

B) Of the genes upregulated in LNCaP vs. RWPE (purple) 24 and 28 genes are further overexpressed in MDAPCa2a and MDAPCa2B, respectively, when compared to LNCaP. Overlap of the genes overexpressed in the MDA cell lines, compared to LNCaP, shows a high concordance between these cell lines, which were derived from the same patient.

C) Genes that change compartment identity from B to A and are overexpressed in all bone metastatic cell lines, compared to LNCaP, which in turn are overexpressed in LNCaP compared to normal epithelium.

**Figure 5. Gene clusters that switch from the B to the A compartment include genes critical for prostate cancer progression.** 40 kb resolution heatmaps, compartment tracks, and TAD boundaries are shown for two representative clusters of genes that change compartment across the primary axis of progression. (Left) WNT5A switches from the B to the A compartment in cells of the primary progression axis. WNT5A sits at the location of a shifting TAD boundary, and strong interaction sites in the TAD surrounding this gene become more apparent in cancer progression as compared to RWPE. (Right) CDK14 switches from the B to the A compartment in most cancer cell lines. A TAD boundary localizes atop the gene body of CDK1.

**Figure 6. Compartment identity switches are accompanied by varying types of structural changes at the TAD level.**

The AR locus is shown as an example of the different categories of TAD-scale genome organization changes that accompany compartment changes. A cartoon of the general type of change is shown above sets of representative data.

A) No structure to structure. In RWPE, the AR locus is in the B compartment, and there is little defined TAD structure. TADs that appear C4-2B and VCaP are of different sizes and location.

B) Stalled loops. In addition to the appearance of a TAD structure, LNCaP, MDAPCa2a and MDAPCA2b show enriched foci of interactions along the edges of TAD boundaries, consistent with previously documented cases of stalled loop extrusion.

C) Structural desert. In 22RV1, the entirety of the AR gene is in a region of depleted contacts.

D) No change. In PC3 and DU145, the AR locus remains disorganized as in RWPE.

E) Genome-wide distribution of above structural change categories across regions that change from A to B (left) or B to A (right).

**Figure 7. Alterations in interactions around the TMPRSS2-ERG locus in cell lines in the metastatic progression axis.**

A) Interaction heatmaps of the portion of chr21 containing TMPRSS2-ERG: chr21:30 Mb – 45.2 Mb at 250kb resolution. The TMPRSS2-ERG translocation is visible in VCaP (blue square) as a high interaction away from the diagonal. Interestingly, the other bone metastatic cell lines (MDAPCa2a and b) also show enhanced interactions close to that area.

B) Log<sub>2</sub> ratio of interactions in each cell line compared to RWPE. Red areas have more interactions in the cell line compared to RWPE, while blue represents fewer interactions compared to RWPE. The area adjacent to the TMPRSS2-ERG translocation (red box) shows an increase in interactions in LNCaP and MDA cell lines. This increase of interactions in the region surrounding these genes is no longer evident in VCaP, where the TMPRSS2-ERG translocation has occurred.

C) TMPRSS2 switches from the B to the A compartment in all cancer cell lines while ERG switches from A to B only on certain cell lines. The TMPRSS2-ERG translocation is easily visible in VCaP, as a high interaction area away from the diagonal. Changes in TAD boundary locations around TMPRSS2 are also observed.

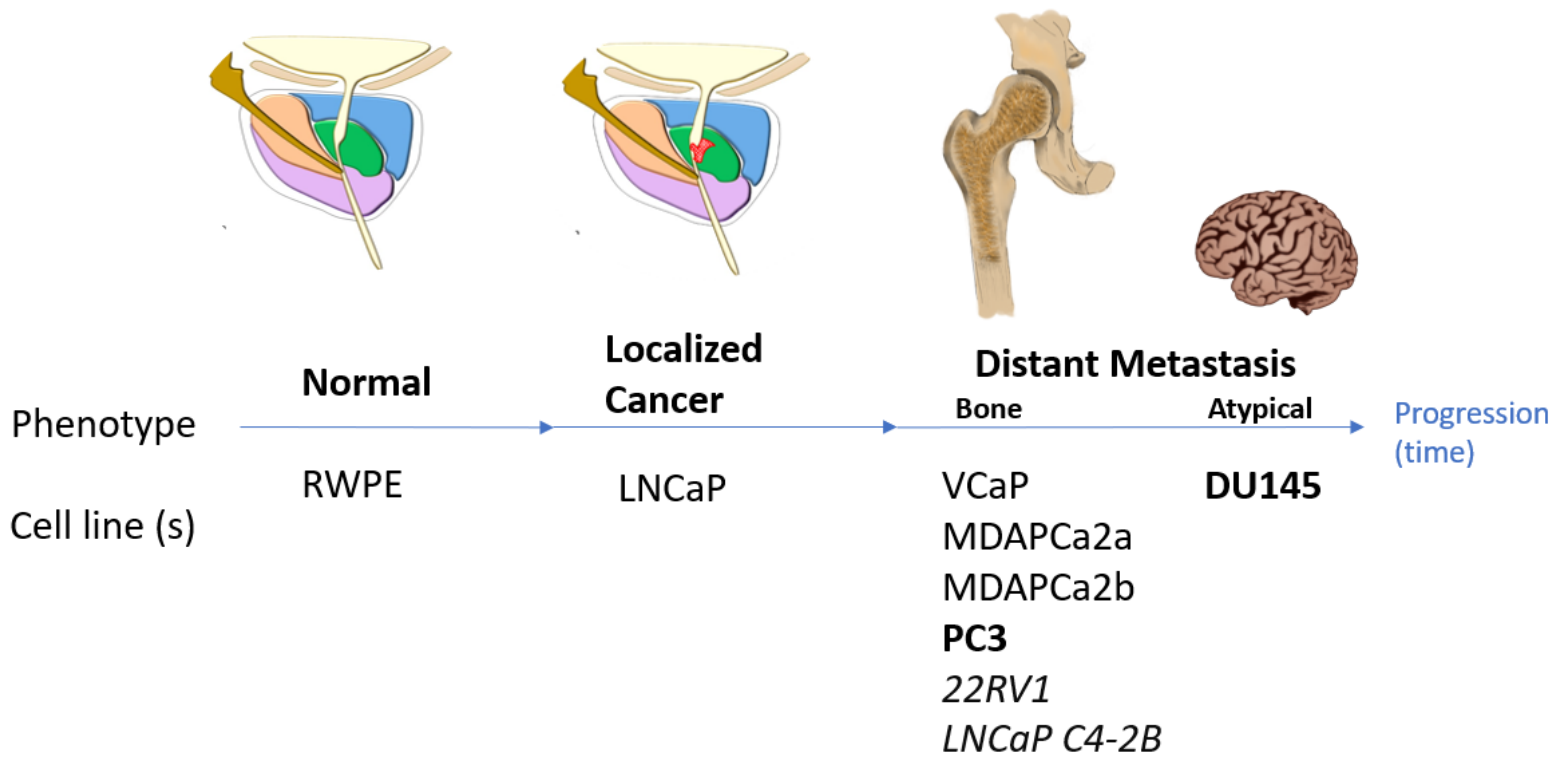


Figure 2

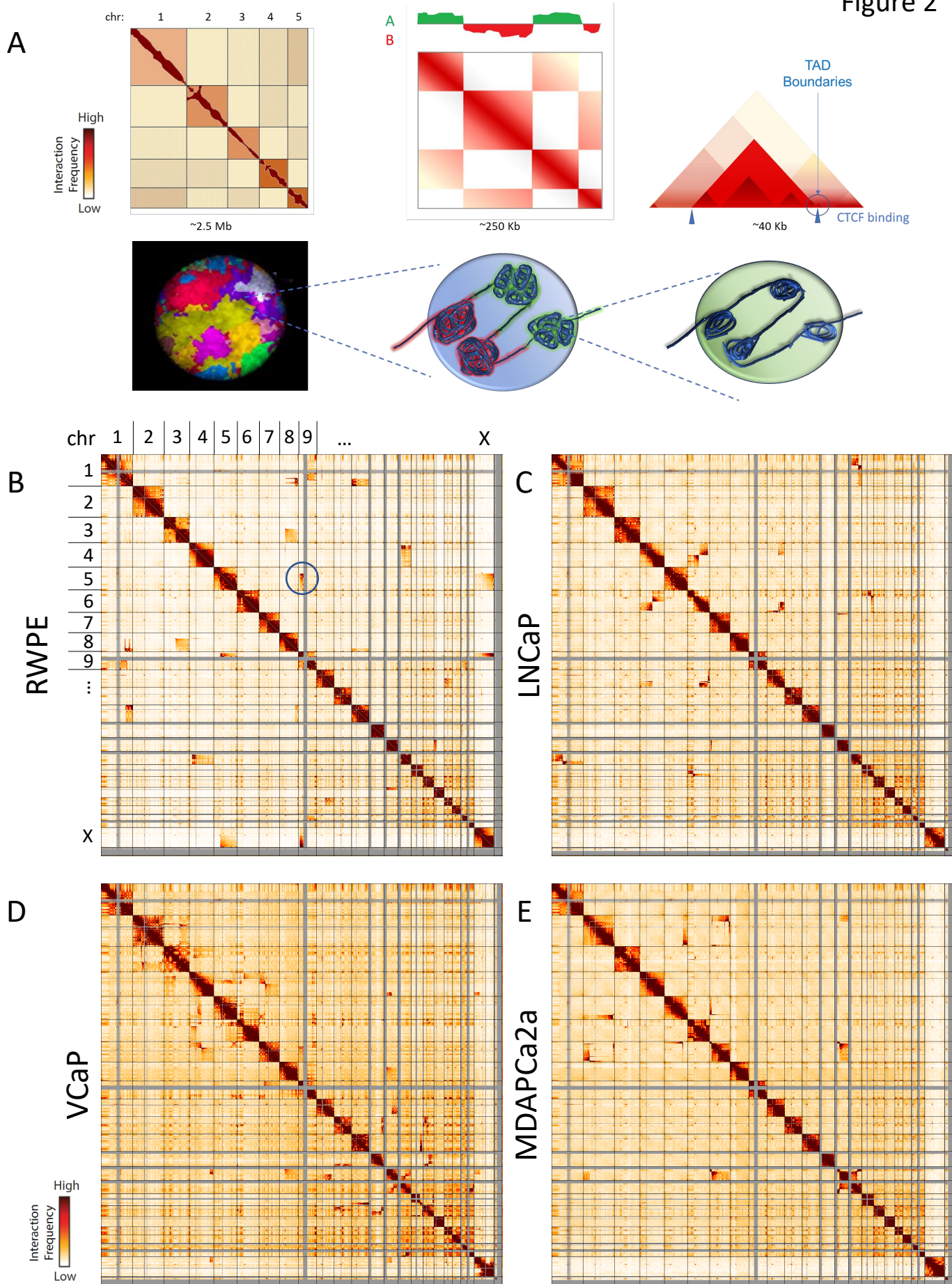
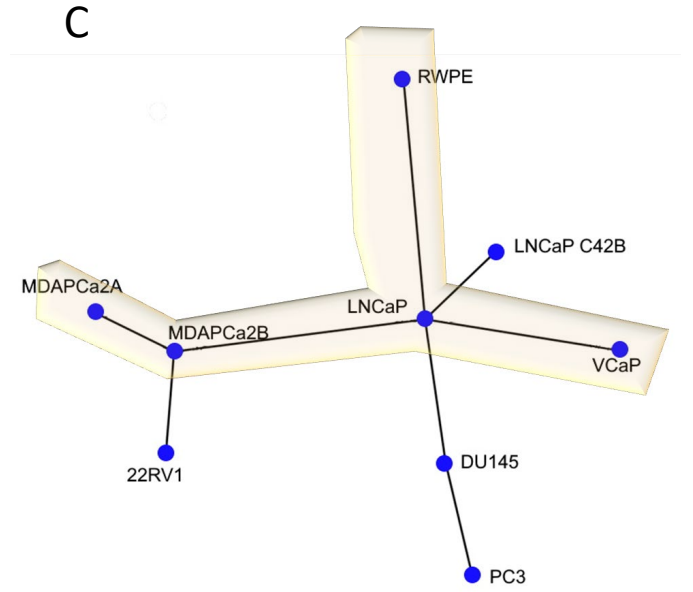
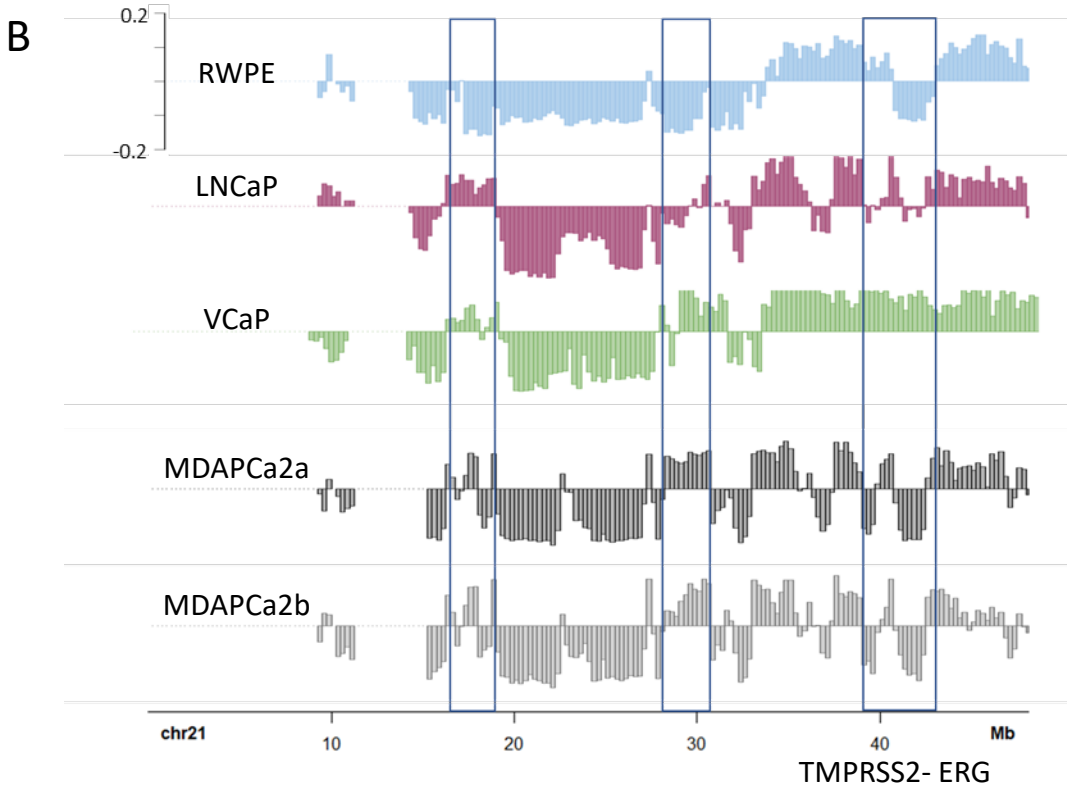
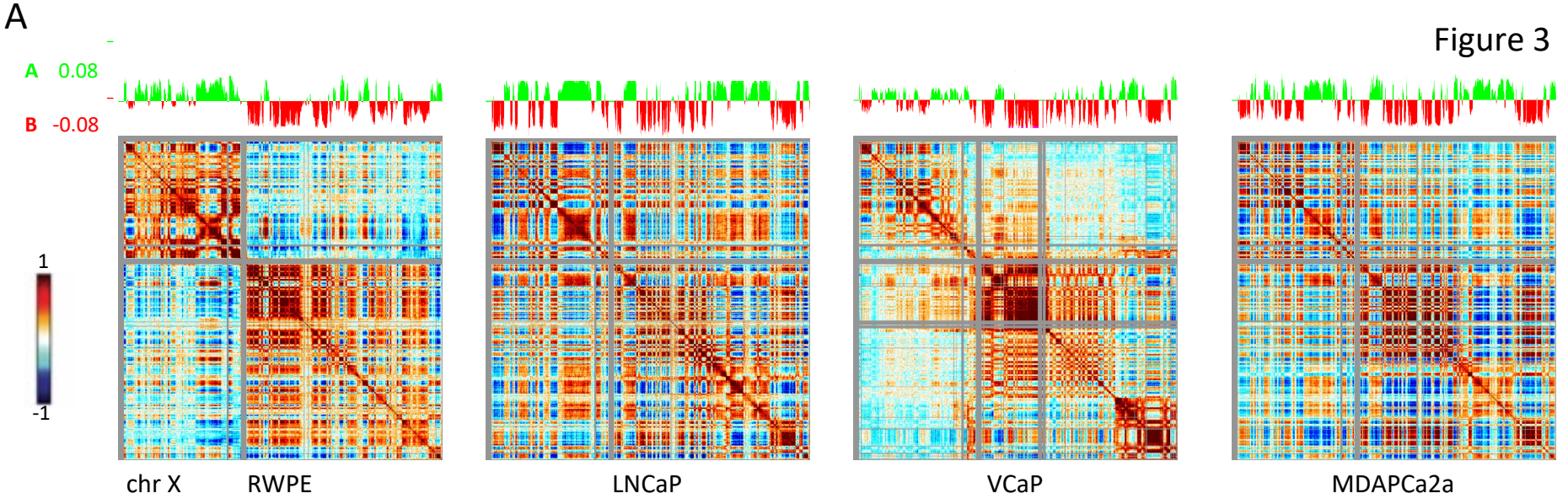
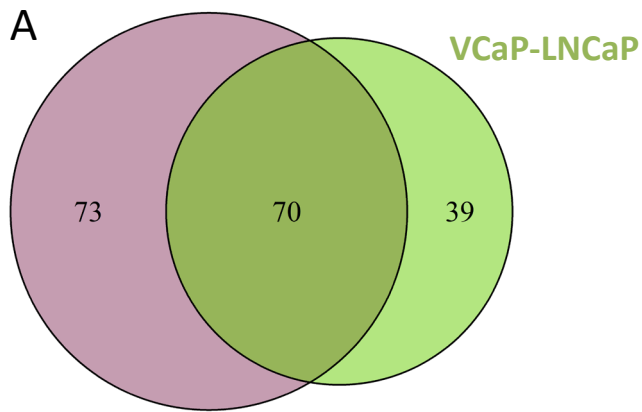




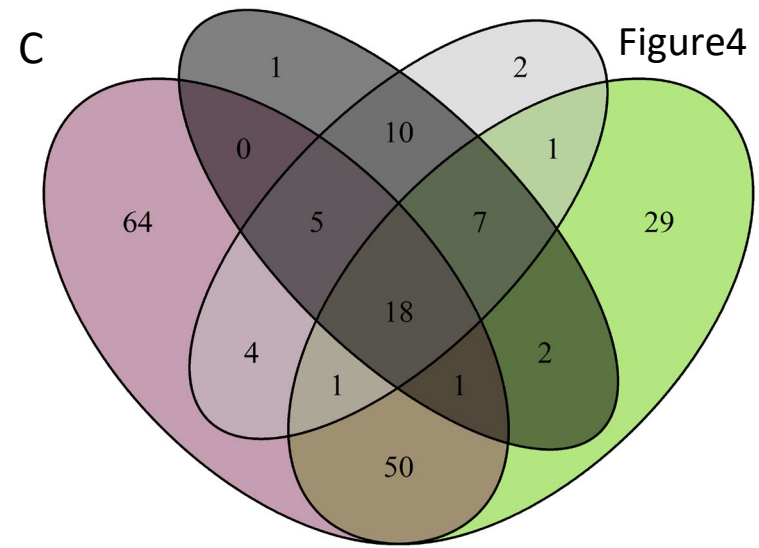
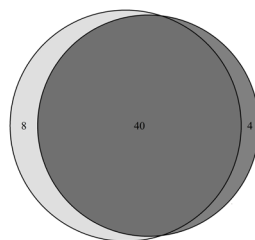
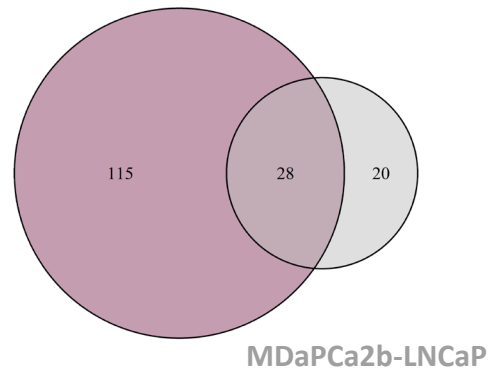
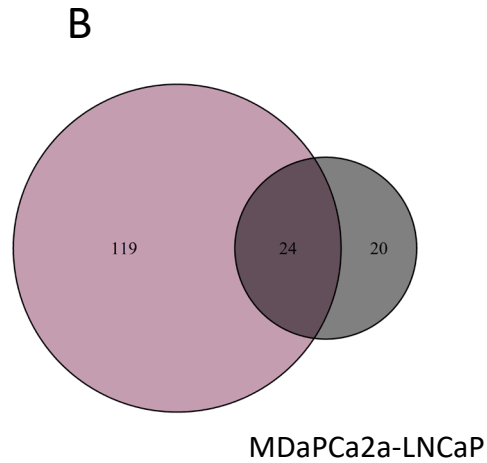
Figure 3





**LNCaP-RWPE**

ABCC4	IGSF5	SECISBP2L	ZNF615
ANK3	LRIG1	SEMA6A	ZNF677
AR	MIS18A	SLC27A2	ZNF765
ASZ1	MTERF3	SLC4A4	ZNF776
CCT8	MYBPC1	SLCO5A1	ZNF792
CDK14	MYRIP	SOX4	ZNF813
CHPT1	N6AMT1	TMPRSS2	ZNF880
CXADR	ONECUT2	TRIM36	
DEPDC1B	OPRK1	UBE2W	
DMXL1	PARPBP	UGT2B4	
DTWD1	PART1	URB1	
EDA	PPM1A	VLDLR	
EXOC5	PPM1H	WNT5A	
FAM3B	PRKCA	ZNF302	
FRY	PRUNE2	ZNF331	
FUT8	PSMC2	ZNF350	
GALK2	RALGAPA2	ZNF544	
GDAP1	REPIN1	ZNF548	
GNA13	RTN1	ZNF550	
GPR180	RWDD2B	ZNF551	
IFRD1	SDC2	ZNF613	



**MDAPCa – VCaP Intersect**

BACE2	TRIM36
CDK14	TSPYL5
CXADR	WNT5A
GALK2	ZNF350
GPC6	ZNF613
HUNK	ZNF615
LTN1	ZNF792
MTERF3	
MYBPC1	
NBEA	
PPM1H	
PRKCA	
PRUNE2	
PTDSS1	
RALGAPA2	
SDC2	
SECISBP2L	
SLC4A4	

**4 Intersect**

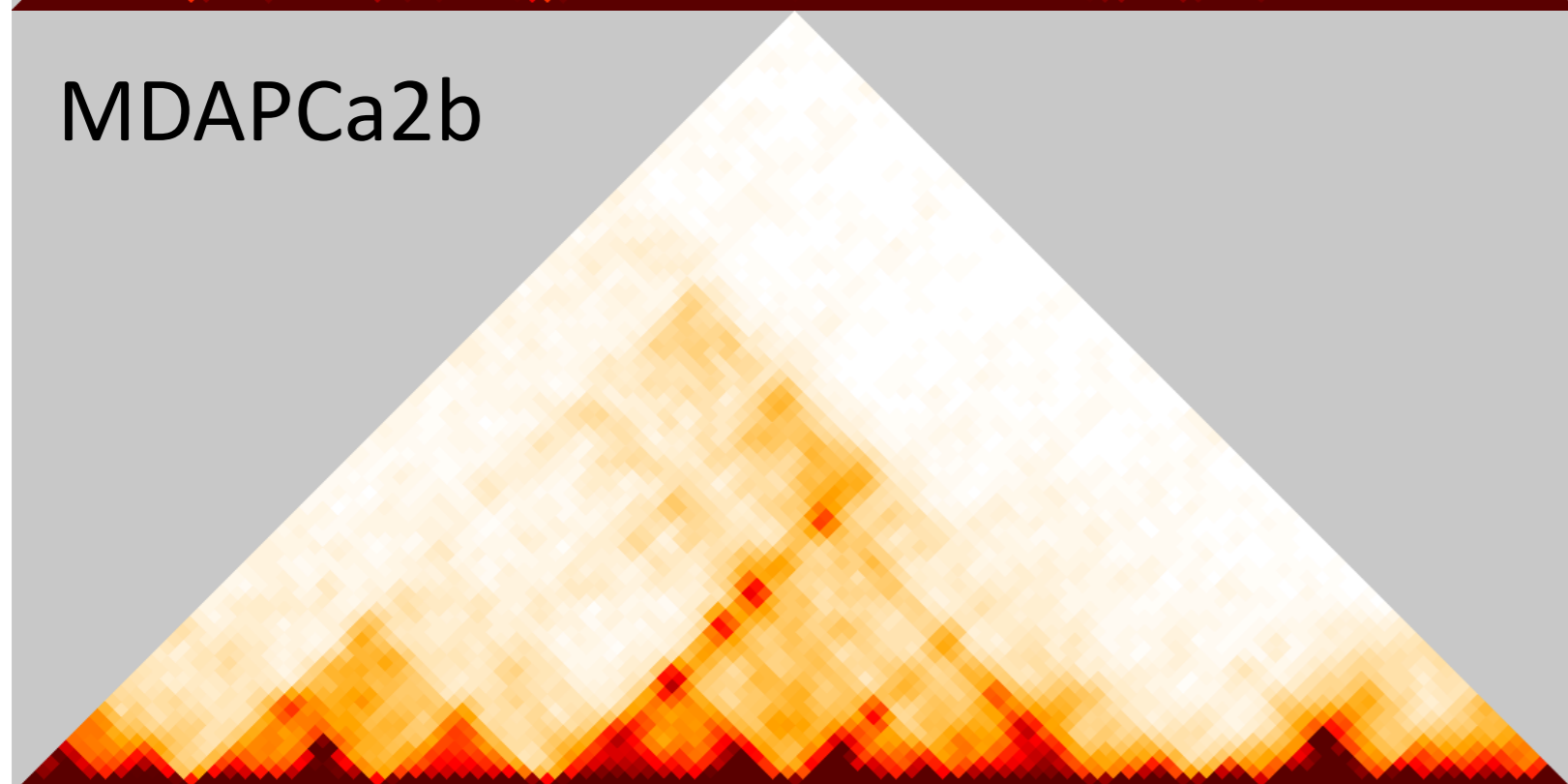
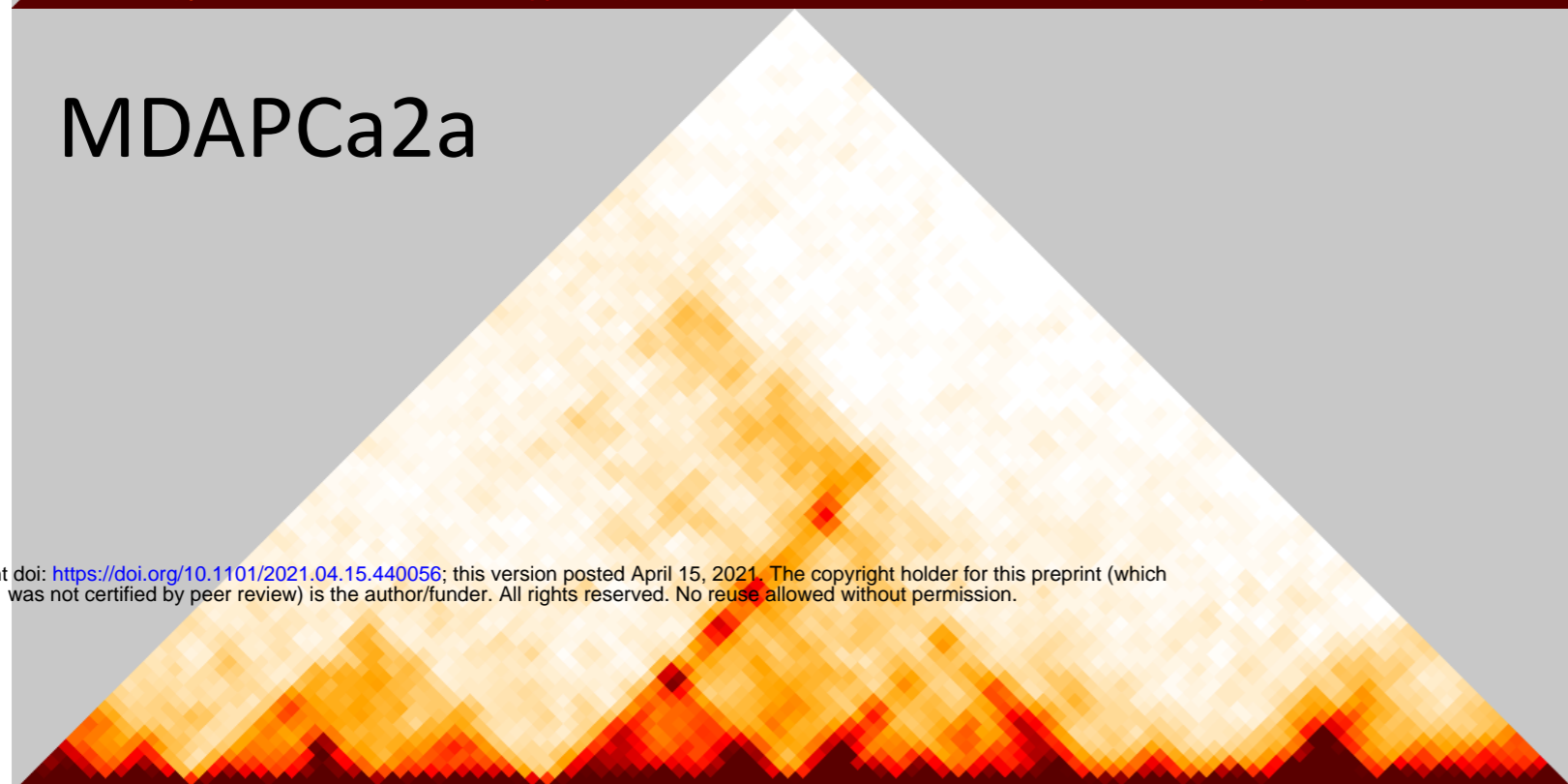
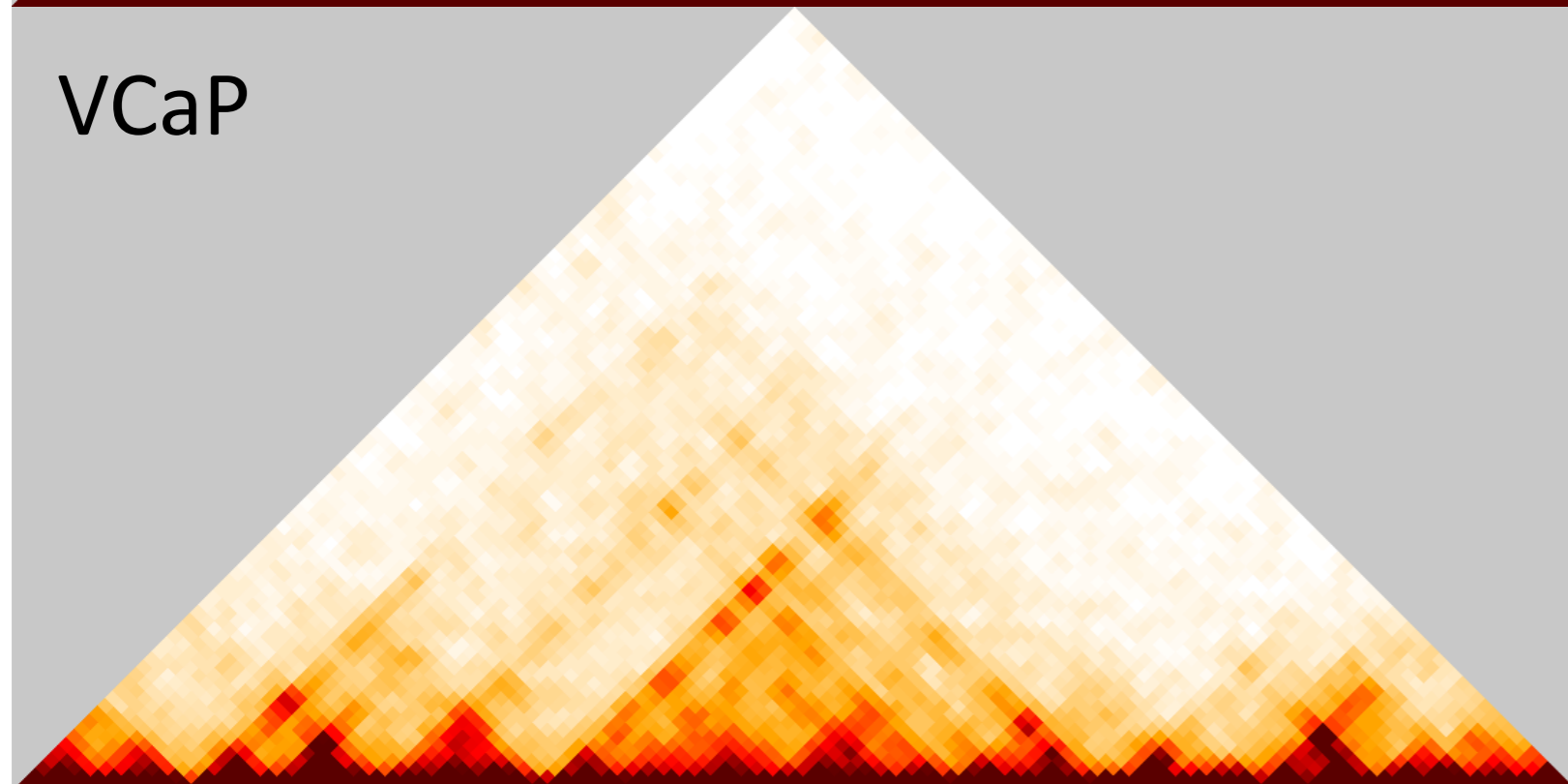
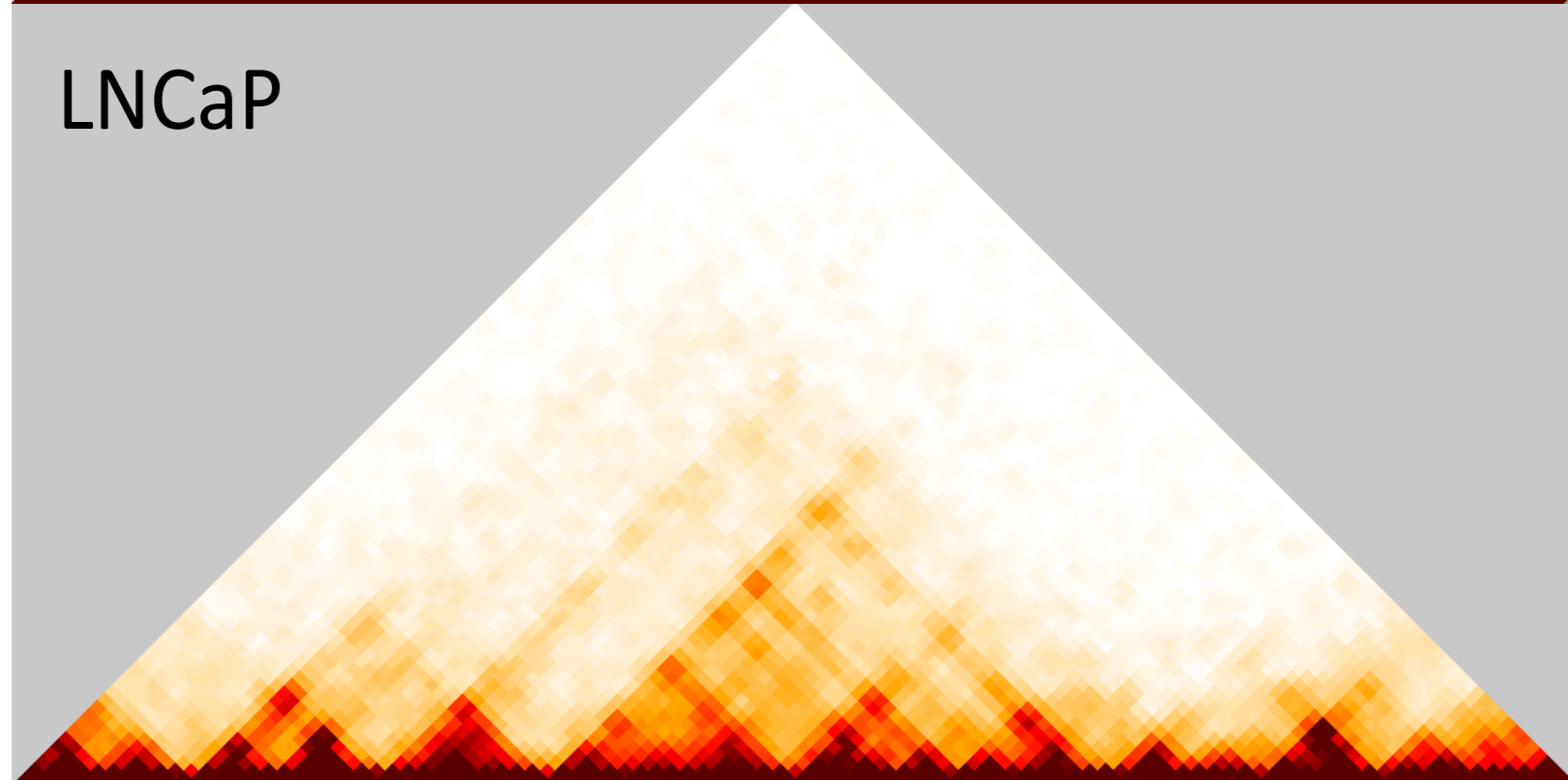
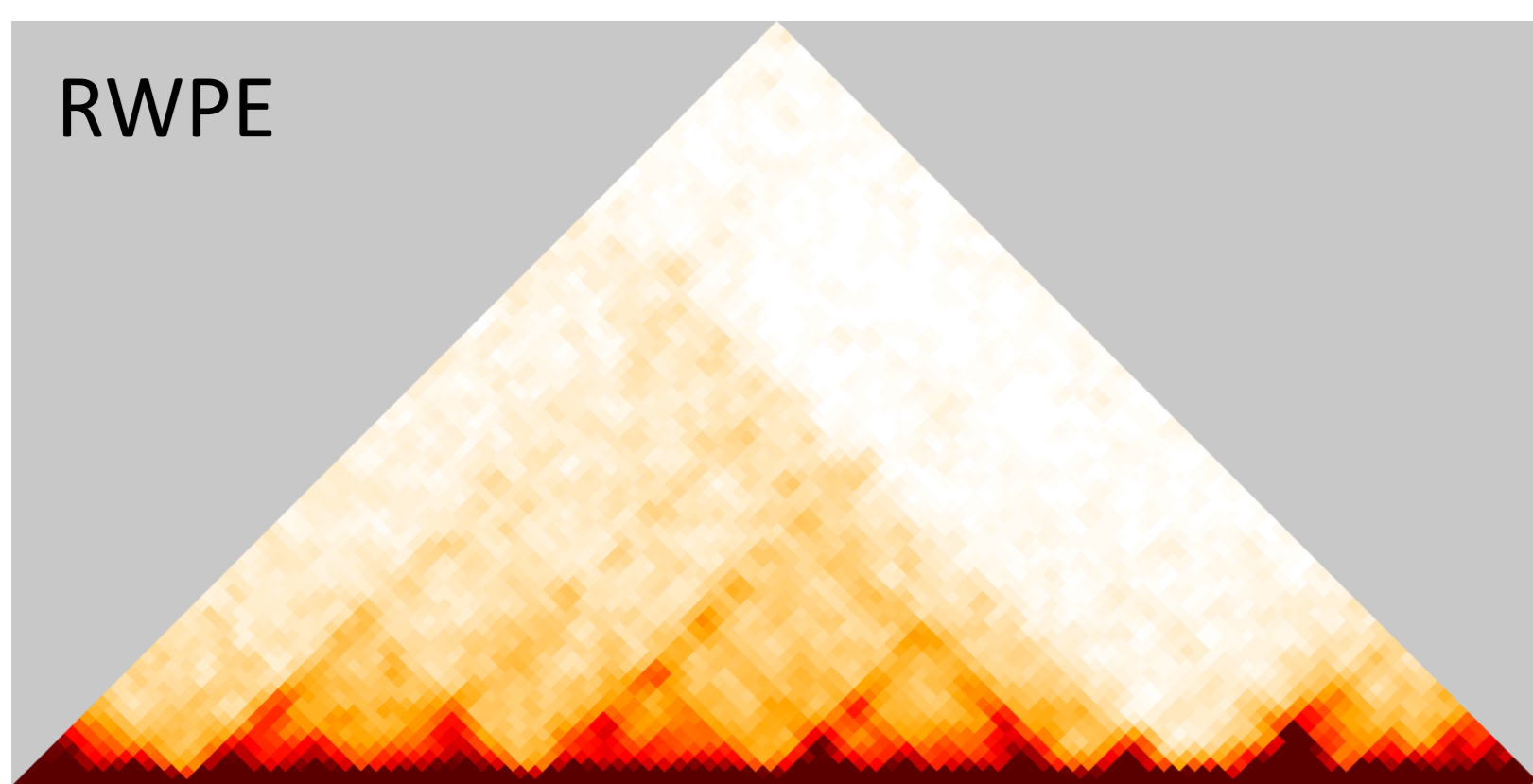
CDK14
CXADR
GALK2
MTERF3
MYBPC1
PPM1H
PRCKA
PRUNE2
RALGAPA2
SDC2
SECISBP2L
SLC4A4
TRIM36
WNT5A
ZNF350
ZNF613
ZNF615
ZNF792

Figure 5

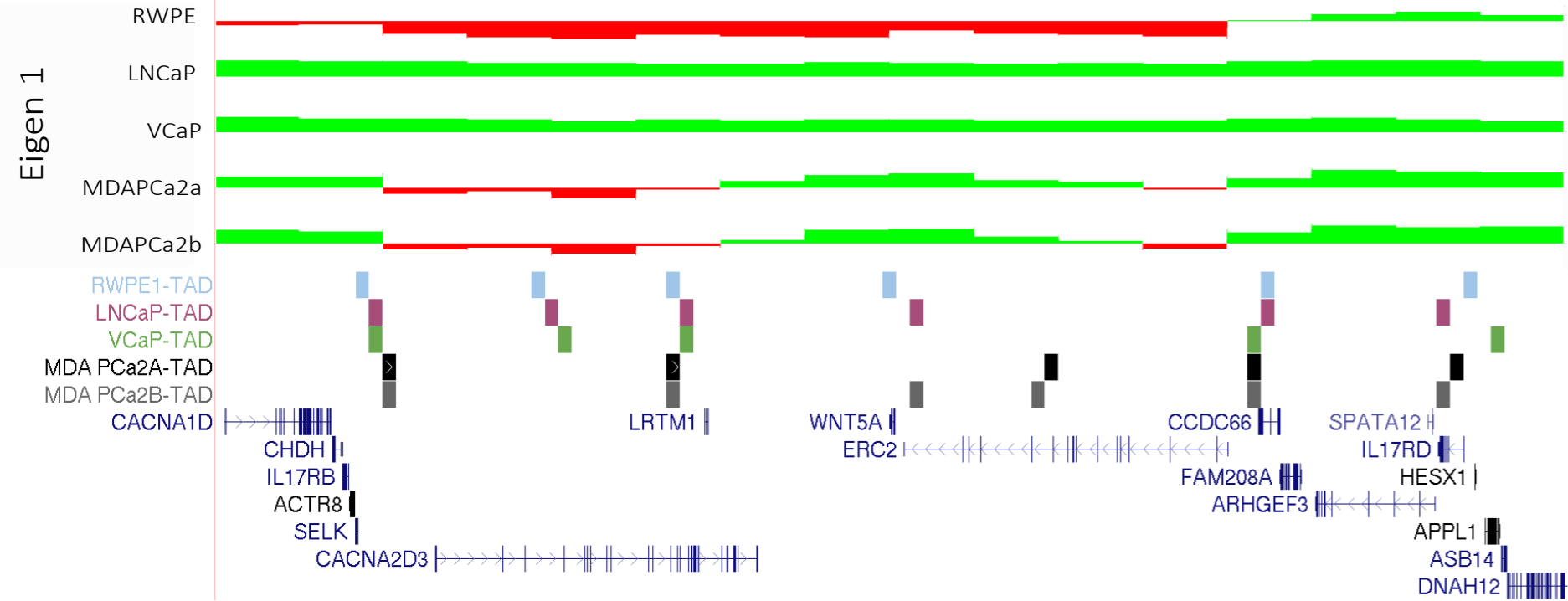
Cluster 1: WNT5A - ERC2

Interaction Frequency

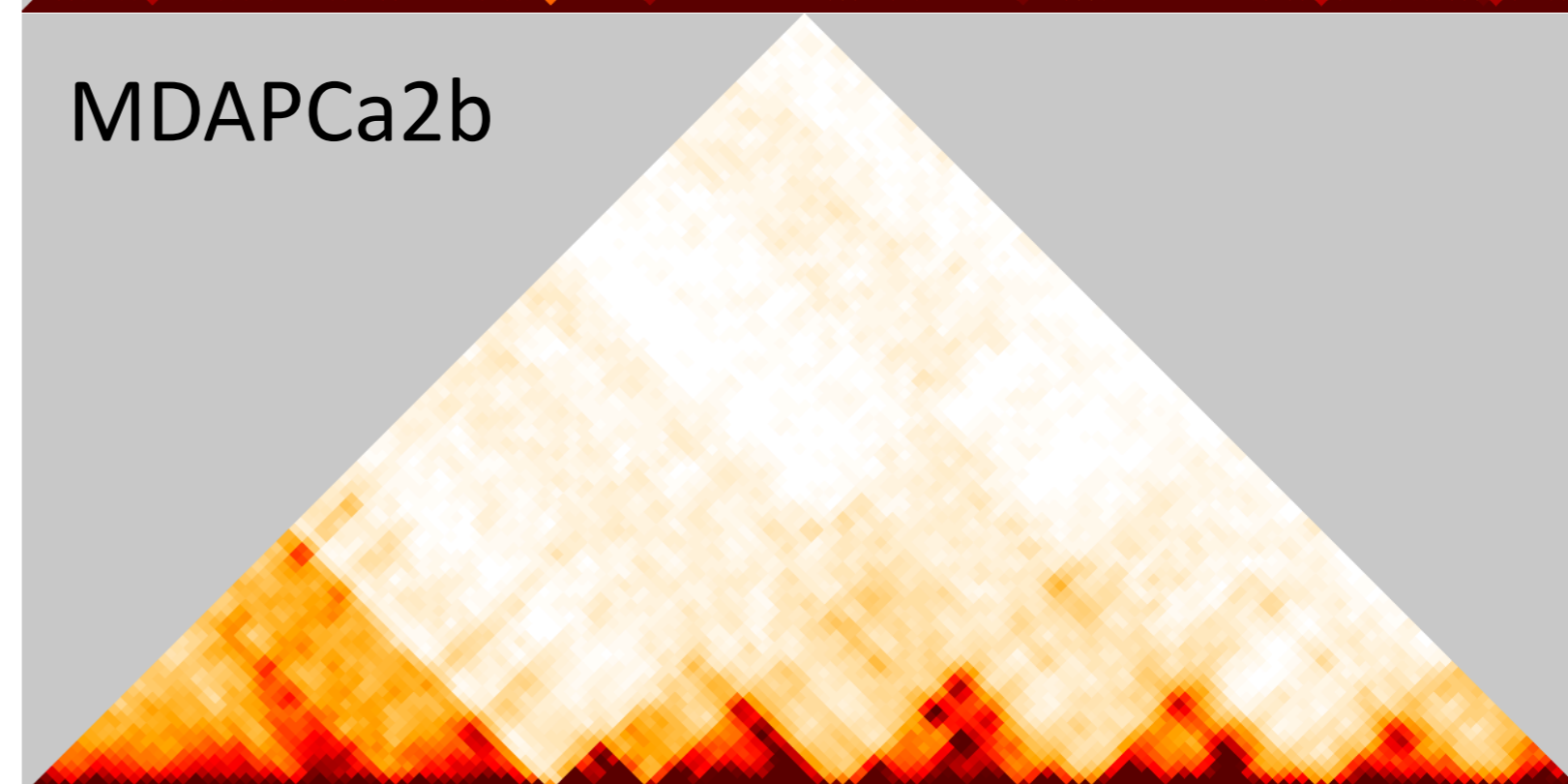
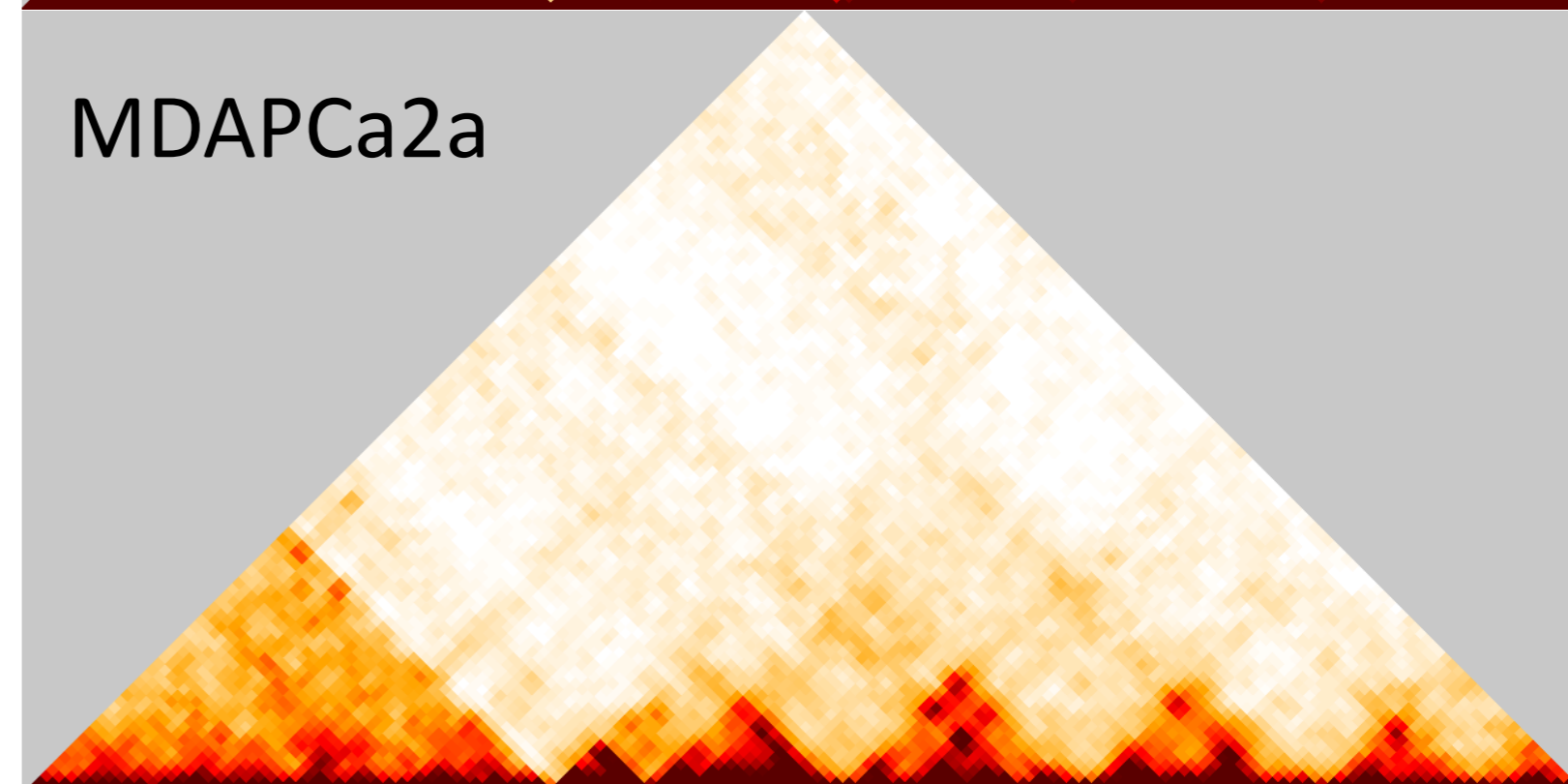
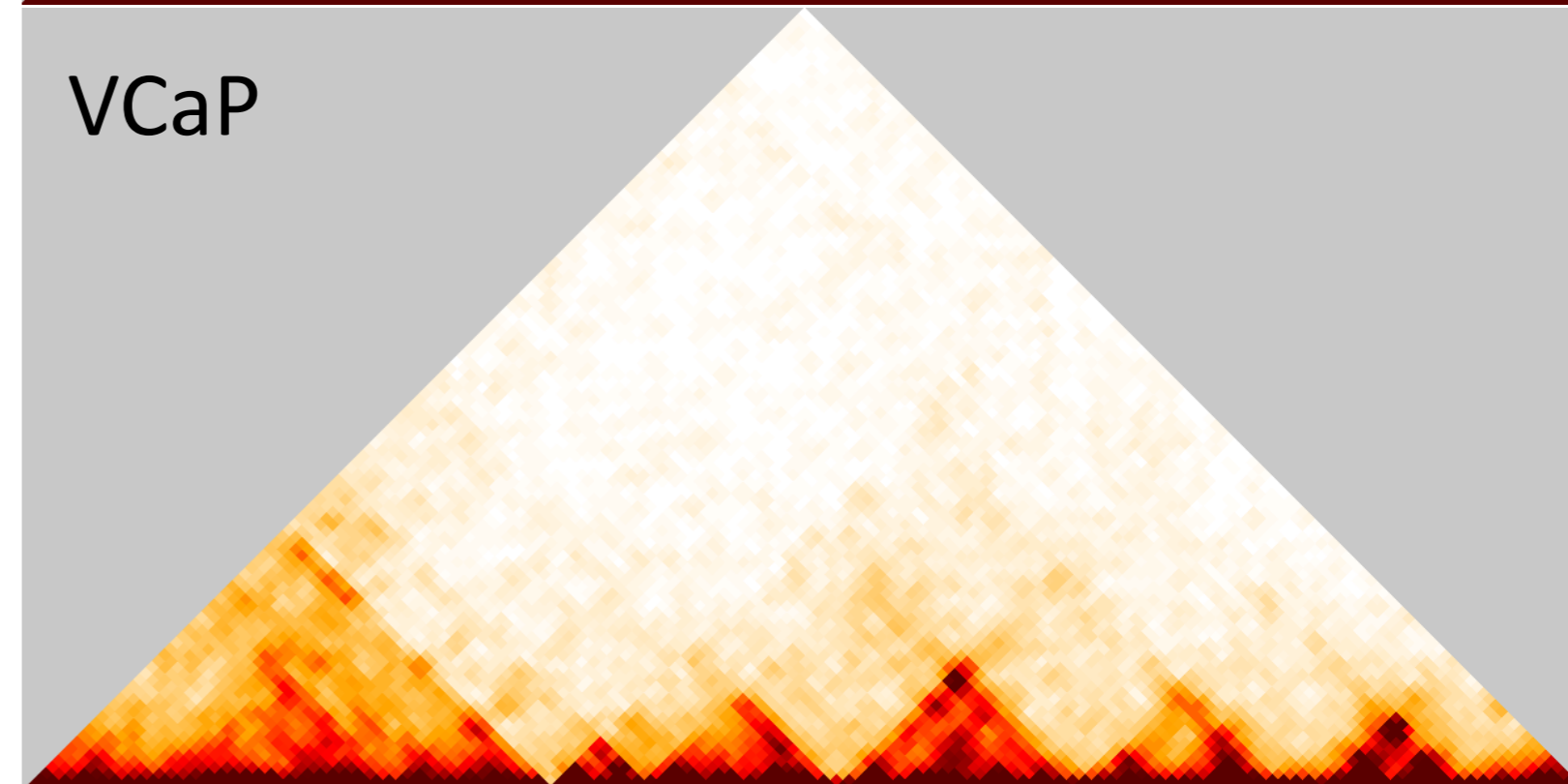
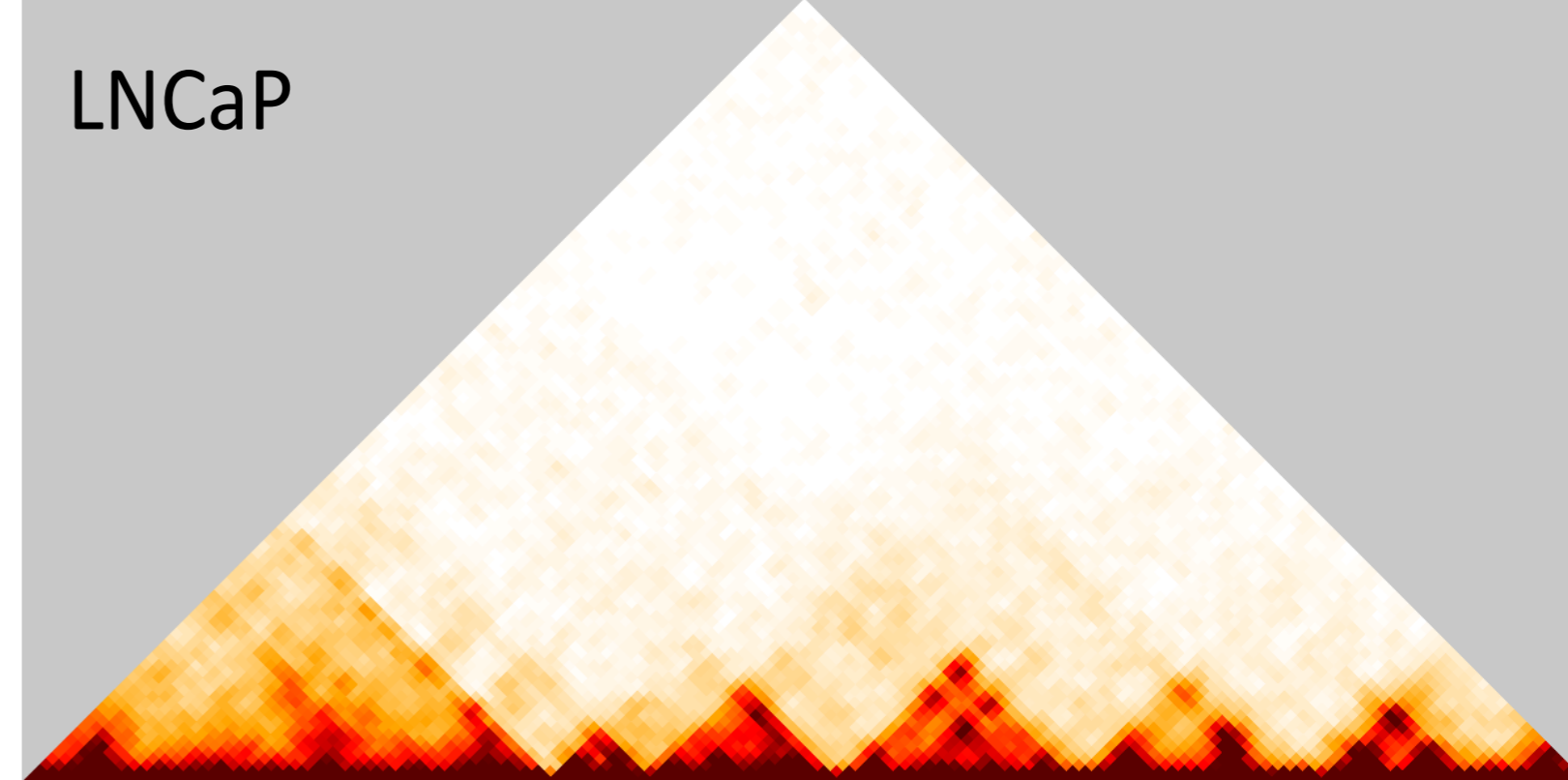
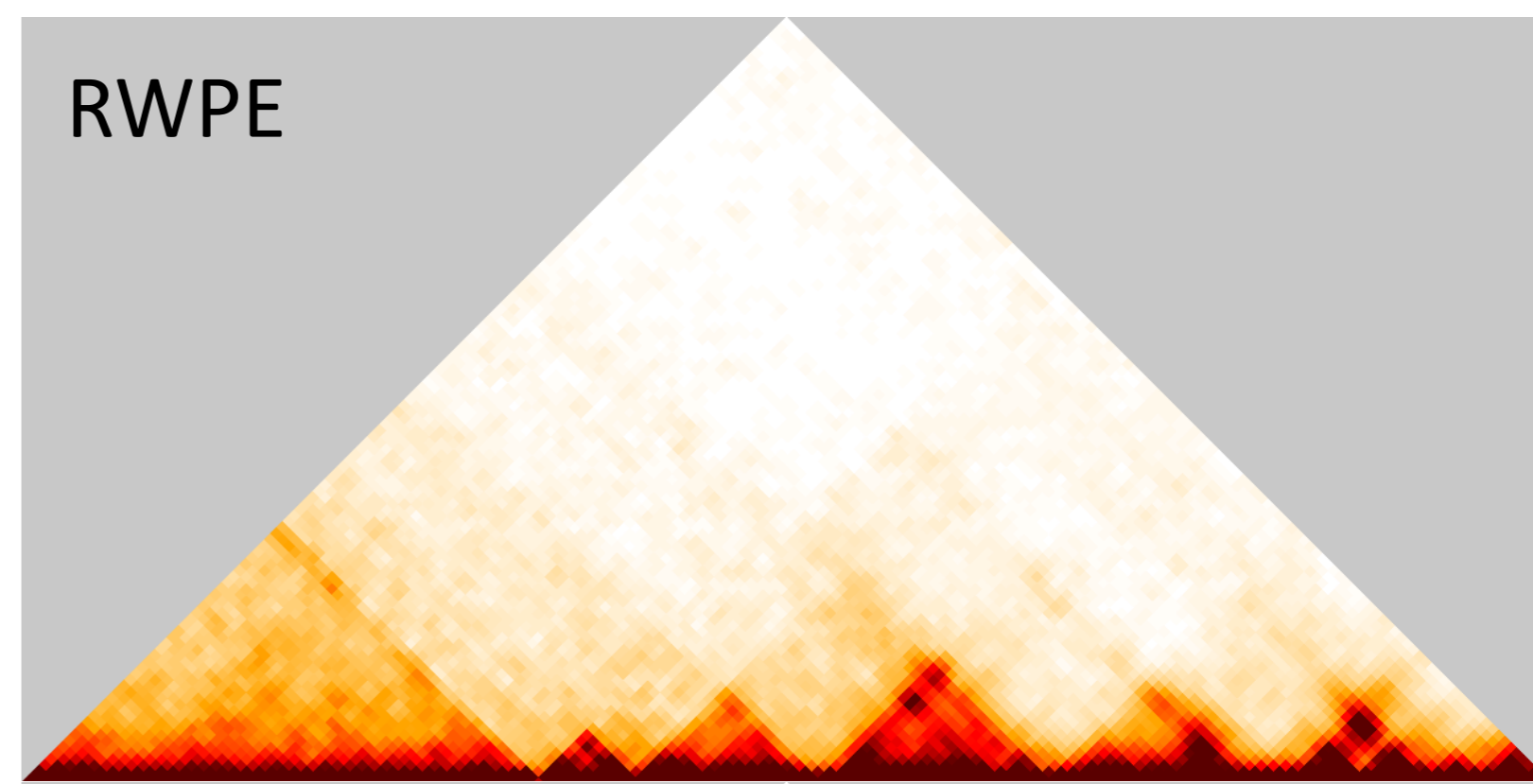
bioRxiv preprint doi: <https://doi.org/10.1101/2021.04.15.440056>; this version posted April 15, 2021. The copyright holder for this preprint (which was not certified by peer review) is the author/funder. All rights reserved. No reuse allowed without permission.



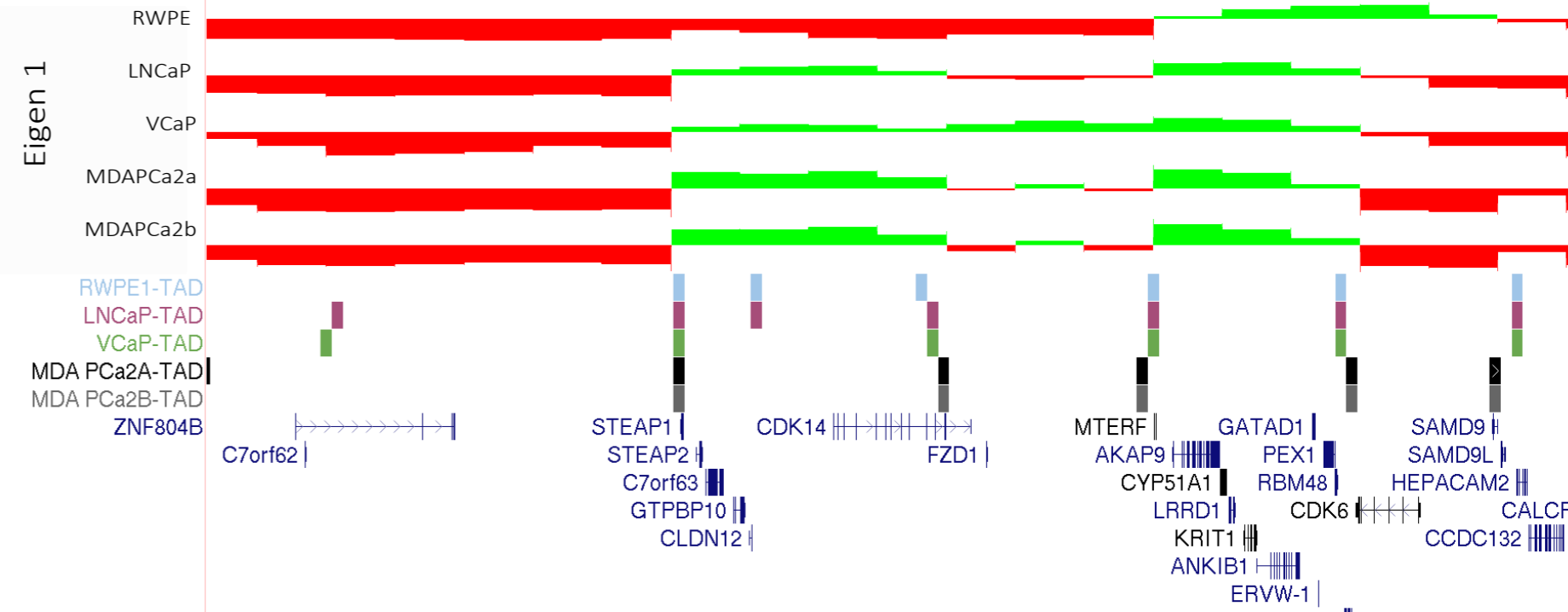
Scale chr3: 54,000,000 54,500,000 55,000,000 55,500,000 56,000,000 56,500,000 57,000,000 57,500,000 hg19

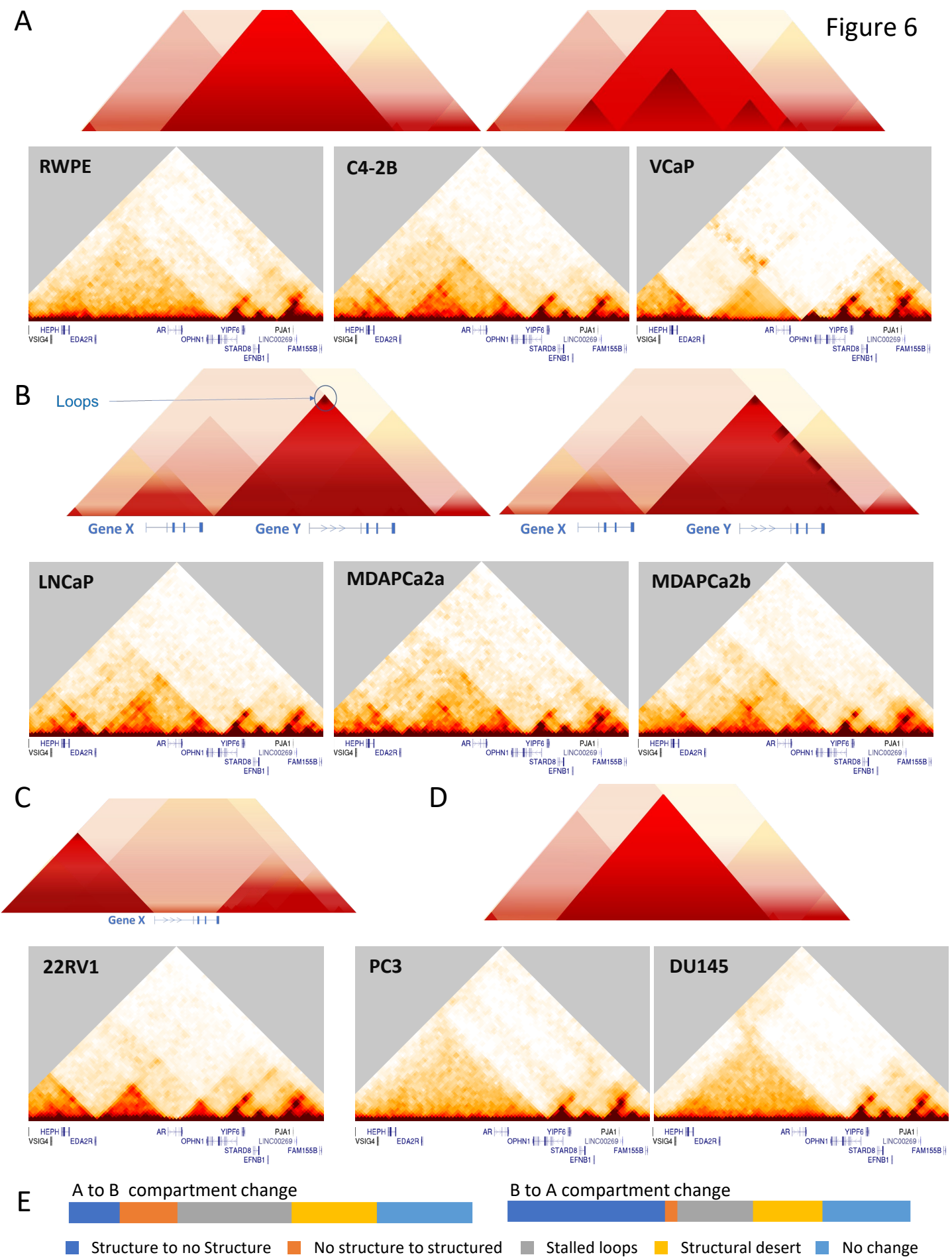


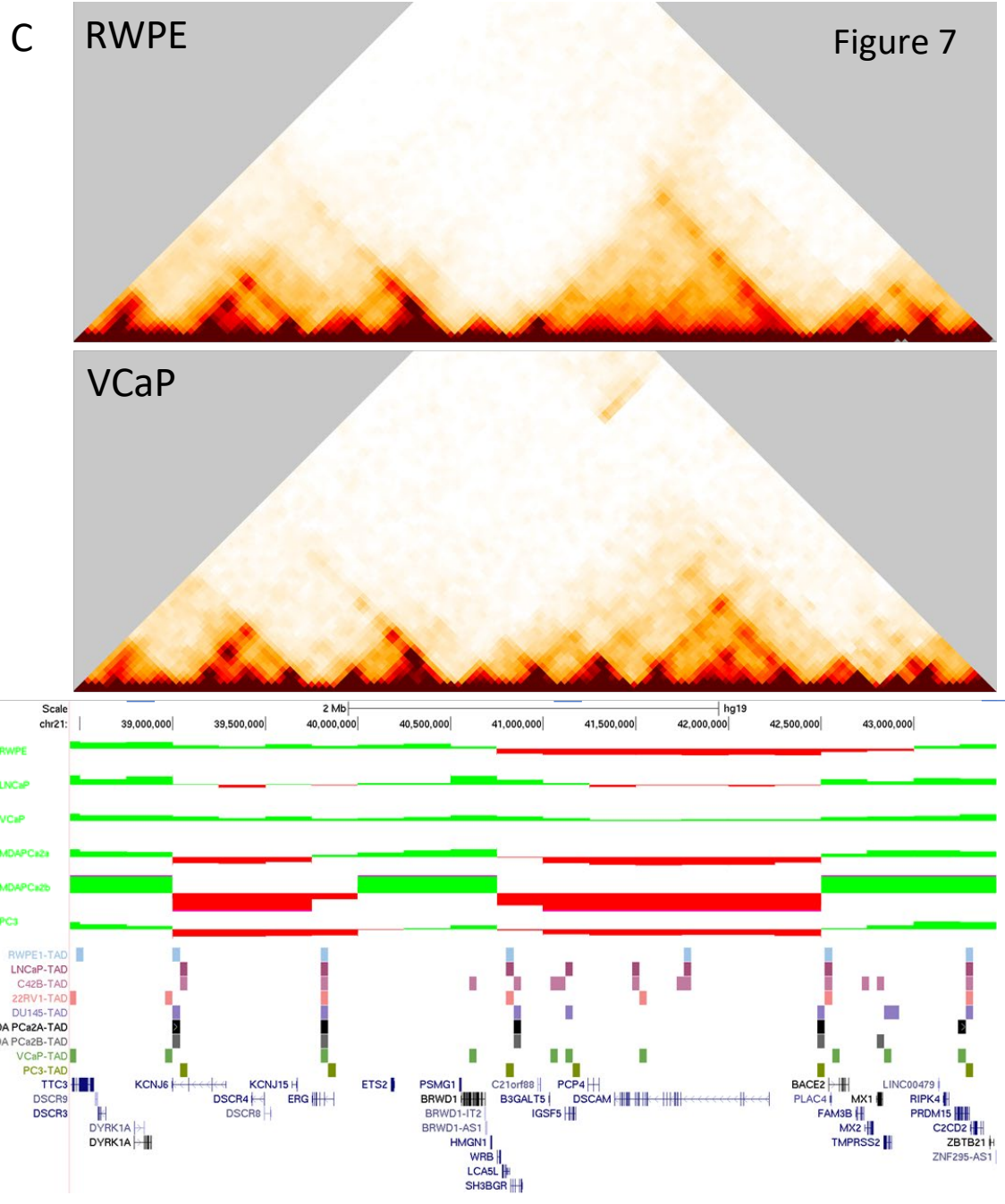
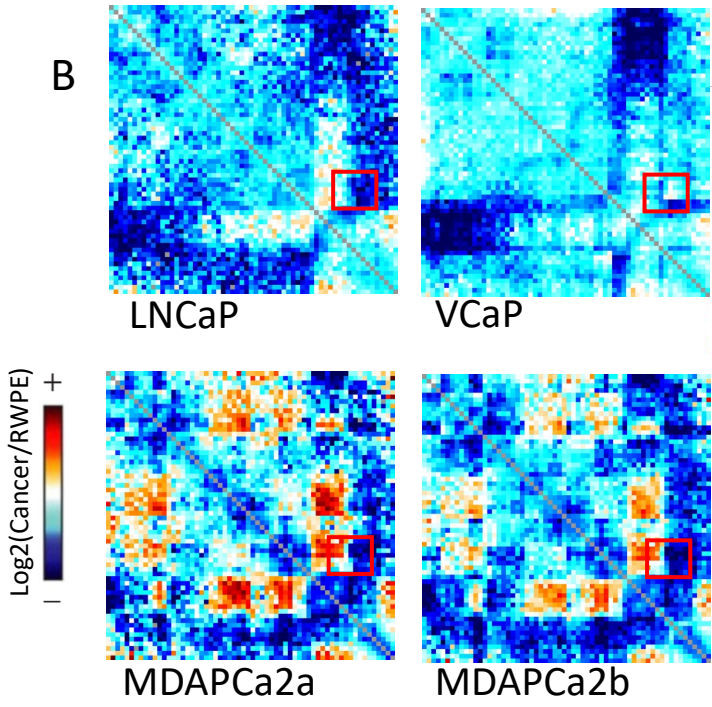
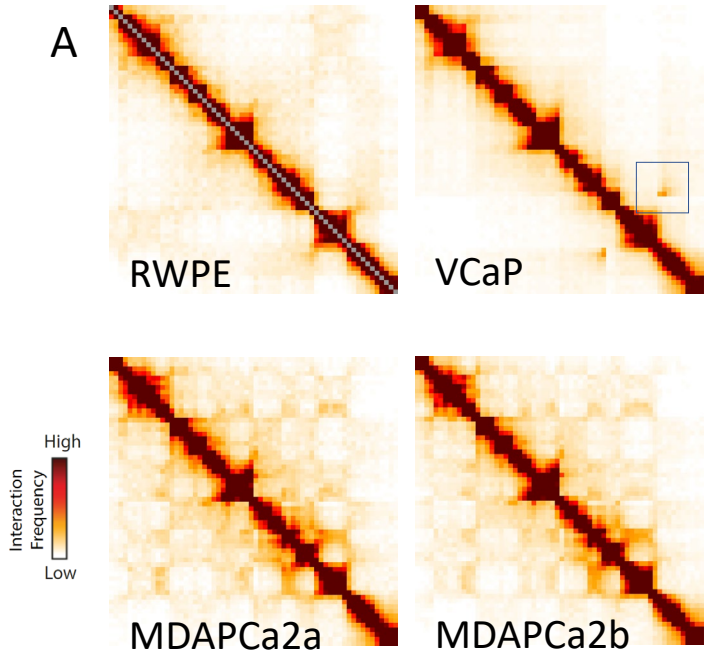
Cluster 2: CDK14 - FZD1



Scale chr7: 88,500,000 89,000,000 89,500,000 90,000,000 90,500,000 91,000,000 91,500,000 92,000,000 92,500,000 93,000,000 hg19







## Supplementary figures

### Note:

The following figures are presented in an abridged form:

Supplementary figure 1

Supplementary figure 2

Supplementary figure 3

Supplementary figure 4

Supplementary figure 6

Please visit <https://3dgenome.utk.edu/3d-genome-architecture-in-prostate-cancer-progression/> to access the complete supplementary figures.

**Supplementary Figure 1. Mapping Statistics for all Hi-C samples.**

**Supplementary Figure 2. Previously reported translocations for cell lines in this study, as well as some novel ones, are evident in heatmaps of 2.5 MB resolution Hi-C data.**

2.5 Mb Hi-C heatmaps for RWPE (A), LNCaP (B), DU145 (C), 22RV1 (D), PC3 (E), MDAPCa2a (F), MDAPCa2b (G) and VCaP (H). Translocations between chromosomes appear as high interaction frequency areas away from the diagonal. Translocations previously described by SKY analysis are listed on the right of each heatmap, along with those events identified in this study; our study has an 83% concordance with previously reported SKY data. The inherent higher resolution of the data obtained by Hi-C makes it possible to identify smaller translocation events.

**Supplementary figure 3. Hi-C Heatmaps for all chromosomes, per cell line, at a 250 kb bin resolution.**

**Supplementary Figure 4. Cis Interaction heatmaps of 250kb-binned data, per chromosome, per cell line.**

**Supplementary Figure 5. Compartment strength and similarity across cell lines.** (A-E) Each graph shows the A-A interaction strength (red) and B-B interaction strength (blue) within each chromosome for the indicated cell line. The dotted line represents the average compartment strength. Compartment strength calculation is defined in Methods. (F) Pearson correlation coefficient between the PC1 compartment tracks genome-wide for the indicated cell lines. A375 is included as a different epithelial-derived cancer (melanoma).

**Supplementary Figure 6. Plots of the 1st eigenvector for each chromosome, obtained from principal component analysis (PC1) of 250 kb-binned data, reveal the compartment identity.**

Compartment tracks, per chromosome for all the cell lines in this study. From the top: RWPE (light blue), LNCaP (violet), LNCaP C4-2B (pink), 22RV1 (coral), DU145(purple), PC3 (gold), VCaP (green), MDAPCa2a (black) and MDAPCa2b (grey). The high concordance of compartmentalization among tracks for all cells in our model for progression suggests that compartment switches are a consequence of intended biological function.

**Supplementary Figure 7. Mathematical reconstruction of highly segmented genomic regions for compartment analysis.**

A) Hi-C Heatmap of a highly segmented chromosome (chr10, PC3). This type of fragmentation precludes compartment analysis.

B) By performing the insulation calculation on the 250 kb-binned data, using an insulation square size of 1.5 Mb it is possible to identify the largest dips in insulation plot, which denote the breaks in the chromosome.

C) Compartment analysis is performed on the fragments defined by the bin location.

For that particular chromosome, the compartment analysis for RWPE is done for the fragments, to provide a fair comparison for subtraction.

### **Supplement Figure 8. Analytical strategy to determine compartment change relevance in Prostate cancer progression.**

A) A histogram of the genome wide PC1 values from compartment analysis, per bin at 250kb resolution shows a trimodal distribution for all cell lines in our model for progression. High, positive values represent the A compartment and low negative values represent the B compartment. The third mode represents enrichment of values close to zero.

B) A per-bin subtraction of the PC1 values from RWPE creates a distribution closer to normal. Changes in PC1 that exceeded +/- 1.5 of the standard deviation were considered significant compartment changes for the purposes of this study.

C) A graphical representation of the  $\Delta$ PC1 analysis for identification of compartment switches. When superimposing two Eigen 1 tracks, we observe three possibilities: a) a clear, significant compartment change, b) a slight change in the same compartment or c) a modest change in compartments. Normalization against RWPE and thresholding is a straightforward way to identify candidate genomic bins for compartment switches.

### **Supplementary Figure 9. Examples of gene clusters**

Examples of genes that switch compartments.

Left. Cluster 18 includes the following genes: FBN1, CEP152, SHC4, EID1, SECISBP2L, COPS2, NDUFAF4P1, GALK2, FAM227B, FGF7, DTWD1, ATP8B4, SLC27A2 and HDC. While in some cell lines the whole area switches compartments, in others the B compartment persists.

Center. Cluster 5 includes the following genes: Cluster with SLC24A3, RIN2, NAA20, CRNKL1, CFAP61, INSM1, RALGAPA2, PLK1S1 XRN2, NKX2-4, NKX2-2, PAX1, FOXA2 and TTC6. Changes to the A compartment in all cell lines in the main progression axis.

Right. Cluster 4 changes compartments as a cluster (in DU145, VCaP and MDA lines) or in fragments. It comprises the following genes: Fry (switches B to A) BRCA2 (switches to the B compartment in 22RV1), and N4BP2L1, RFC3, DCLK1, CCNA, SMAD9, ALG5, ZAR1L, RXFP2, and EEF1DP3, all of which switch from the B to the A compartment

### **Supplementary Figure 10. The amyloid precursor protein (APP) – beta secretase 2 (BACE2) axis, located in chromosome 21 is a potential connection between transcriptional activity and compartment switching.**

Compiled data aligning microarray expression (Log2) for genes along chromosome 21. Genes whose expression increases  $\geq 2$  fold or decreases  $\leq 2$  fold in the comparison, with a p value  $< 0.05$  represented as vertical tick marks along the X axis (chromosome location). Chromosome compartment tracks overlay, superimposed along the microarray track). APP-specific probes highlighted in pink. An increased APP expression is observed in all comparisons, except for MDAPCa2b/LNCaP.



A, B, C) Data from HG-U133\_Plus\_2 microarray comparing LNCaP/RWPE, VCaP/RWPE and VCaP/LNCaP, respectively

D,E) Data from Clariom S microarray, comparing MDAPCa2a/LNCaP and MDAPCa2b/LNCaP, respectively

**Supplementary Table 1. Database references and valid pair counts for all datasets used in this study.**

**Supplementary Table 2. Genes identified through  $\Delta$ Eigen 1 analysis (In at least 6 cancer cell lines OR in all 4 cancer cell lines represented in the axis).**

Eighty five percent of all genes identified as switching from the B to the A compartment are included in 48 proximal clusters. Of the genes that switch from the A to the B compartment, 74% are included in 16 clusters.

**Supplementary Table 3. Gene clusters that switch compartment identity with progression**

Gene clusters that switch from the B to the A compartment are highlighted in green, those that switch from the A to the B compartment, in red.

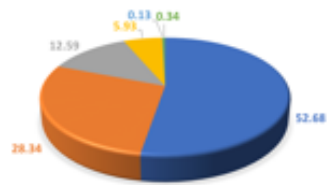
RWPE



LNCaP



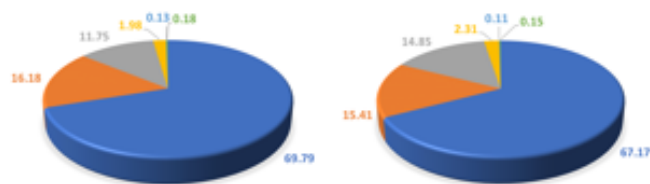
LNCaP-C42B



22RV1



DU145



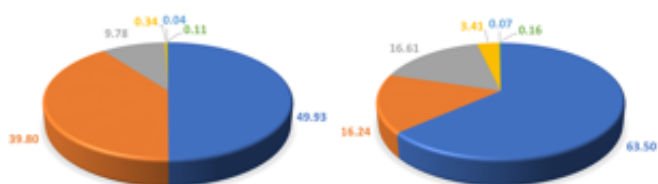
VCaP



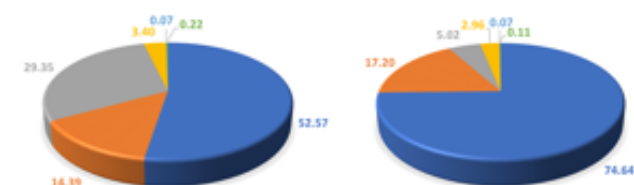
PC3



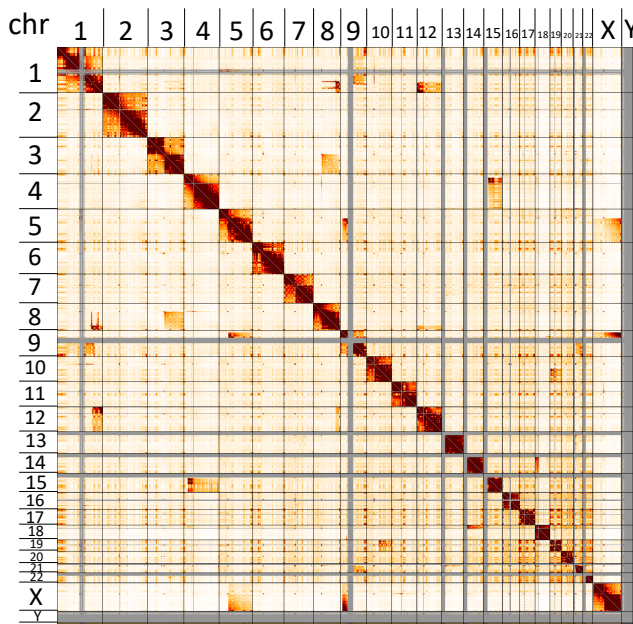
MDAPCa 2a



MDAPCa2b



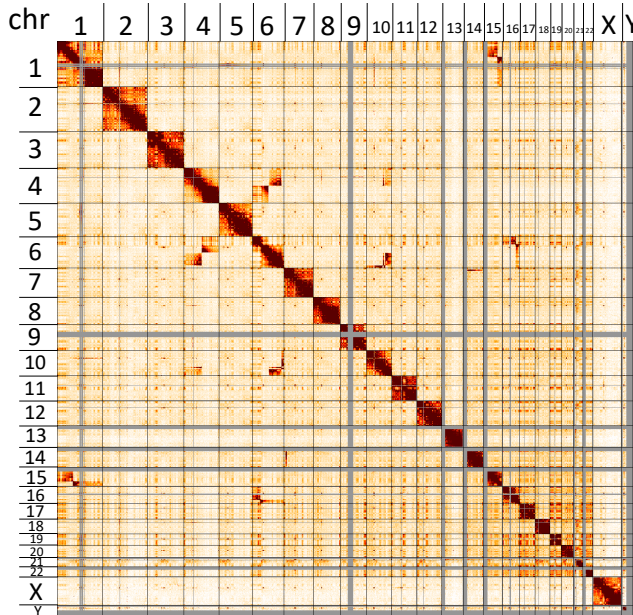
A



## RWPE

		Observed in Hi-C
ATCC SOP	der(X)t(X;5)(q28;q11.2) der(1)t(1;9)(q42;q22.1) t(4;15)(p16;q11.2) der(18)t(14;18)(q11.2;q11.2) t(9;21)(q13;p11.2)	Yes Yes Yes Yes Yes
Roh, et al.	t(9;20;X) t(11;18) t(14;18) t(18;20)	Yes No Yes No
Additional identified by Hi-C in this study	t(1;8) t(1;12) t(3;8) t(5;9) t(10;19)	

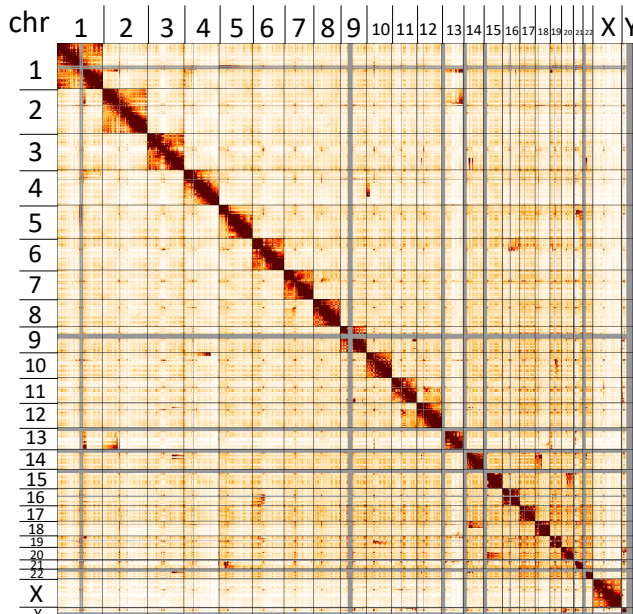
B



## LNCaP

		Observed in Hi-C
ATCC SOP	t(1;15)(p22;q22)x2 der(16)t(6;16)(p12;q11.2)x2	Yes Yes
Pan Y. et al	der(1)t(1;15)(p22;q24)x2 der(4)t(4;6)(q22;q15)x2 der(6)t(6;16)(p21.1;q22) der(15)t(1;15)(p22;q24)x2 der(16)t(6;16)(p21.1;q22)x2	Yes Yes Yes Yes Yes
Additional identified by Hi-C in this study	t(4;10) t(6;10)	

C



## DU145

		Observed in Hi-C
ATCC SOP	der(6;16)(p10;q10) der(10)t(10;19)(p10;p10) der(11;12)(q10;q10) der(15)t(15;20)(q10;q10)x2	Yes Yes Yes Yes
Pan, Y et. al.	der(1)t(1;4)(p11;p12) der(5)t(5;21)(p11;?) der(8)t(7;8)(p11.2;p11.2) der(10)t(10;19)(p11.1;?) der(11;12)(q10;q10) der(13)t(2;13)(?;p11.1) der(15)t(3;15)(?;q26) der(6;16)(p10;q10) der(18)t(14;18)(q?;q21)x2 der(15;20)(q10;q10)x2 der(Y)t(Y;20)(q12;?)	Yes Yes Yes Yes Yes Yes Yes Yes Yes Yes Yes
Additional identified by Hi-C in this study	t(1;2) t(1;13) t(10;4) t(14;3) t(21;5)	

Chromosome 1

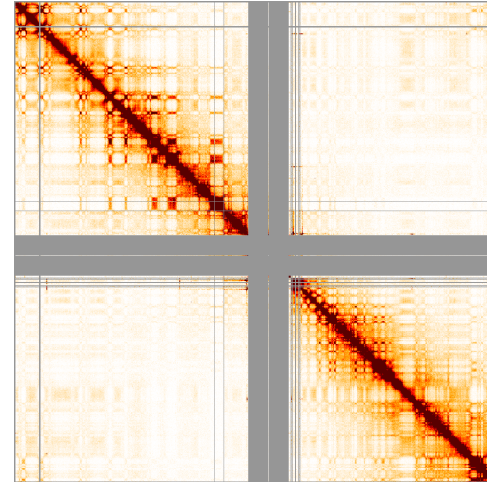
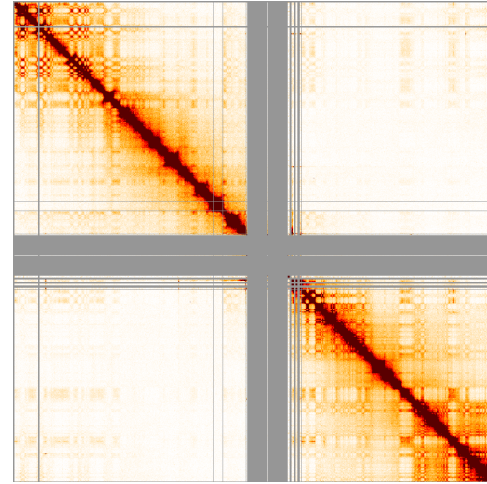
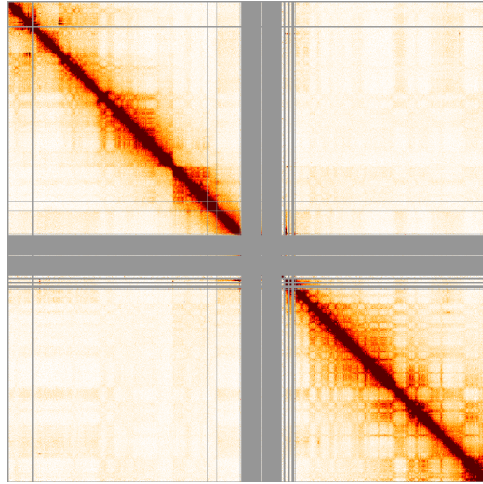
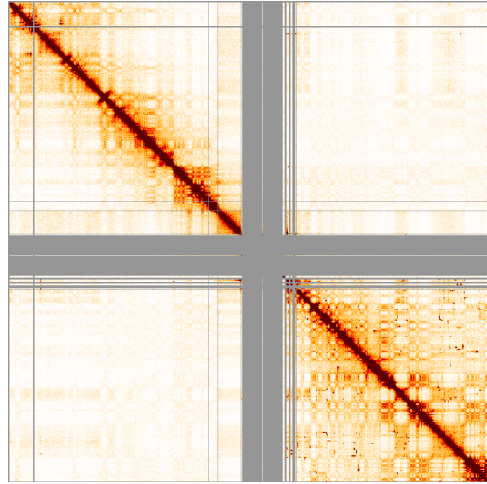
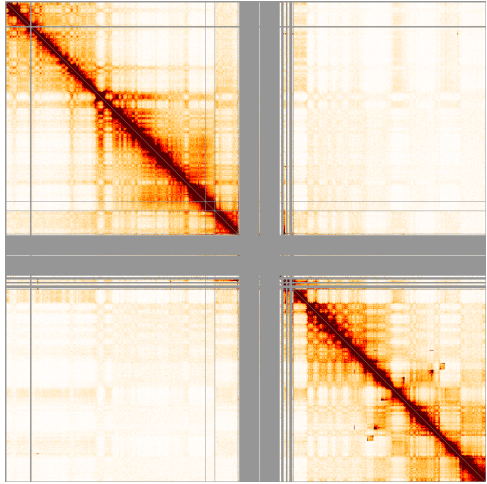
RWPE

LNCaP

LNCaP C4-2B

22RV1

DU145

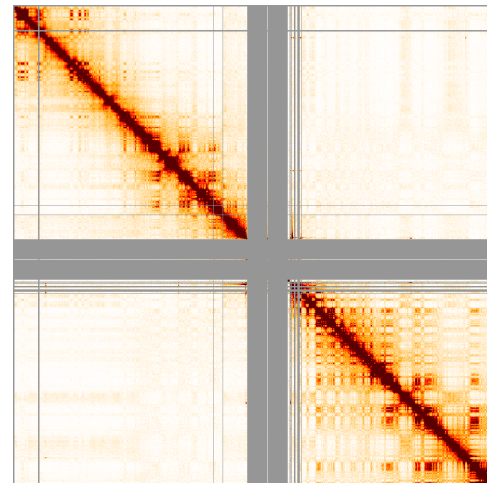
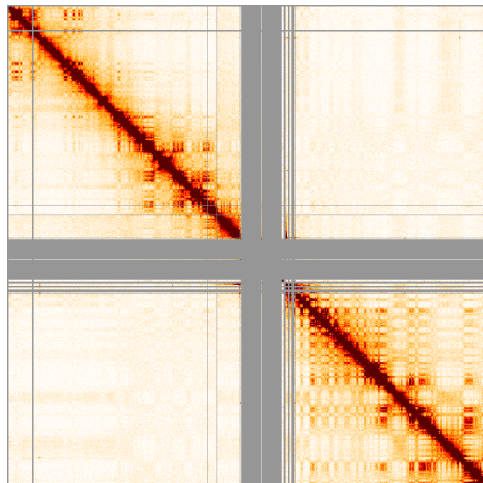
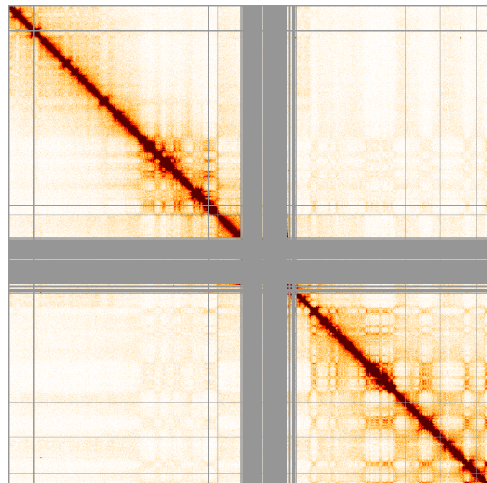
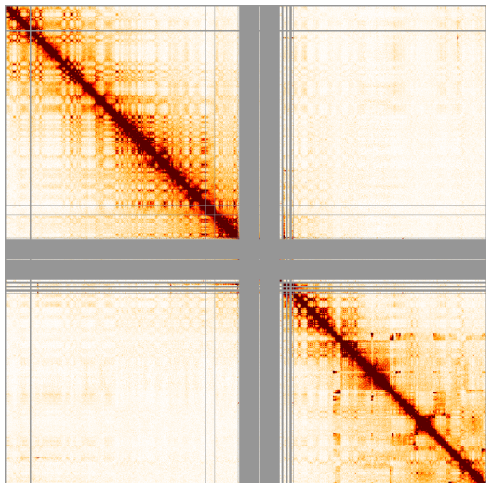


PC3

VCaP

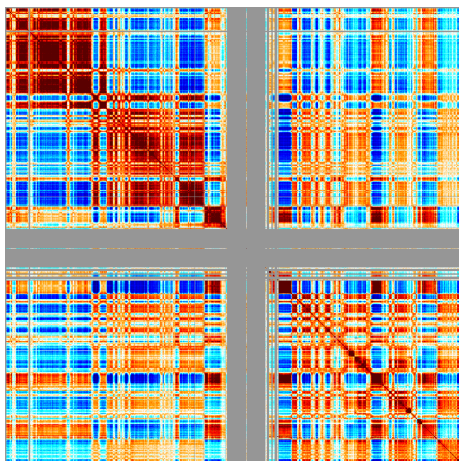
MDAPCa-2A

MDAPCa-2B

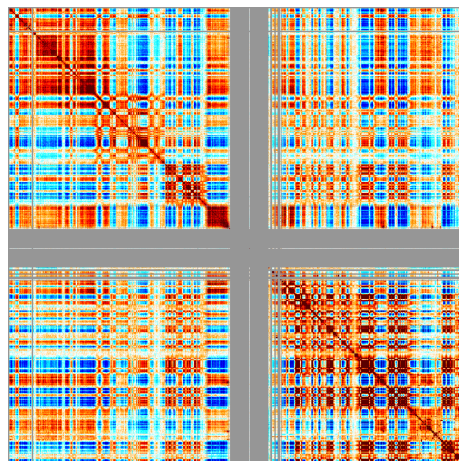


# Chromosome 1

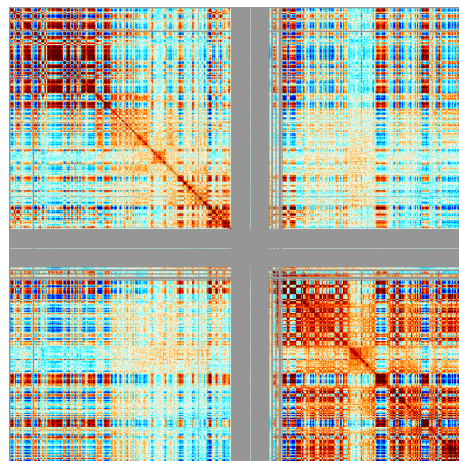
RWPE



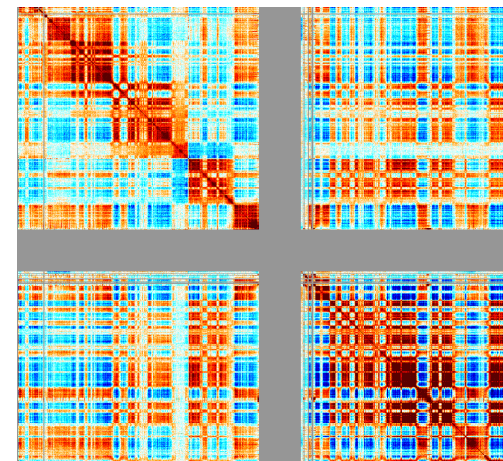
LNCaP



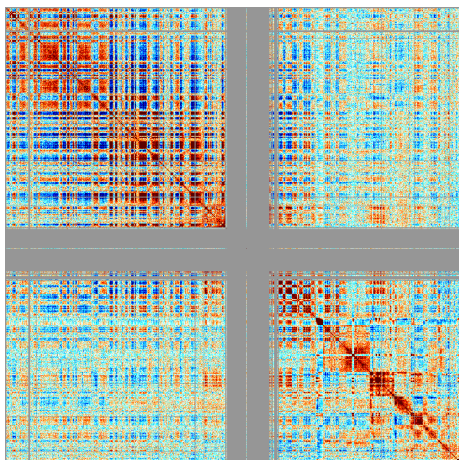
22RV1



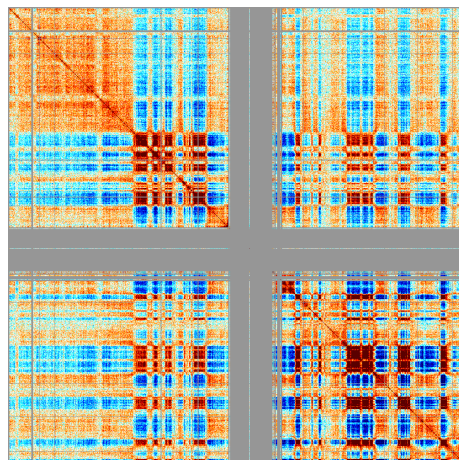
C42B



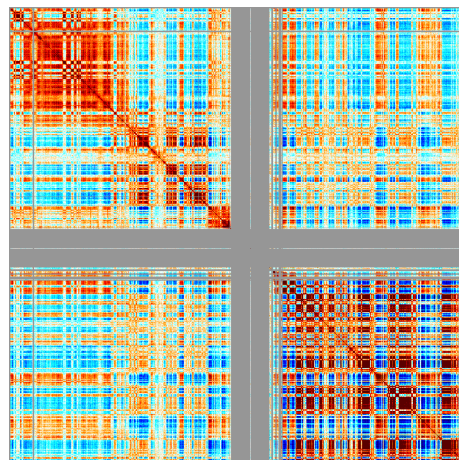
PC3



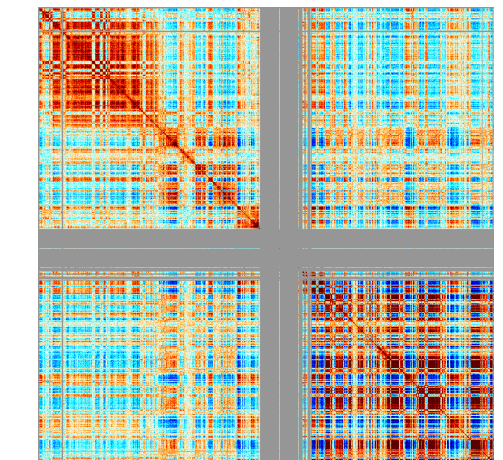
VCaP



MDAPCa2A

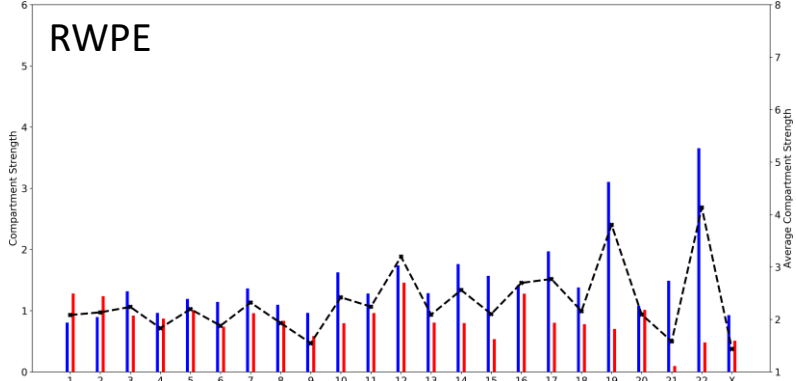


MDAPCa2B

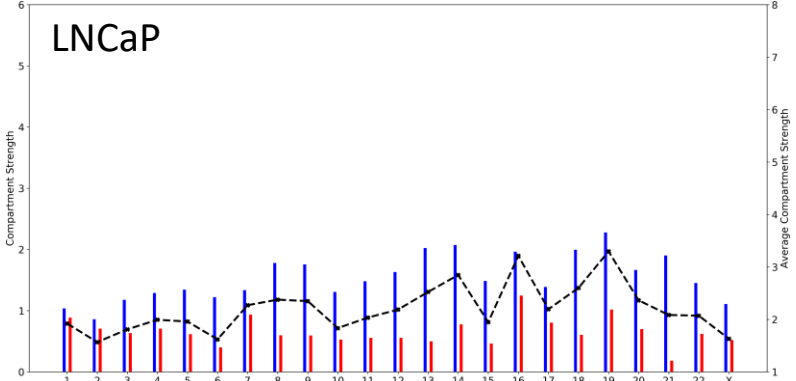


# Supplementary Figure 5

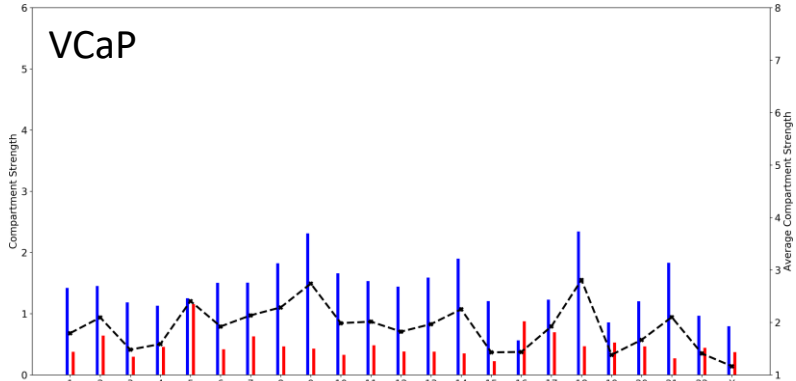
**A** RWPE



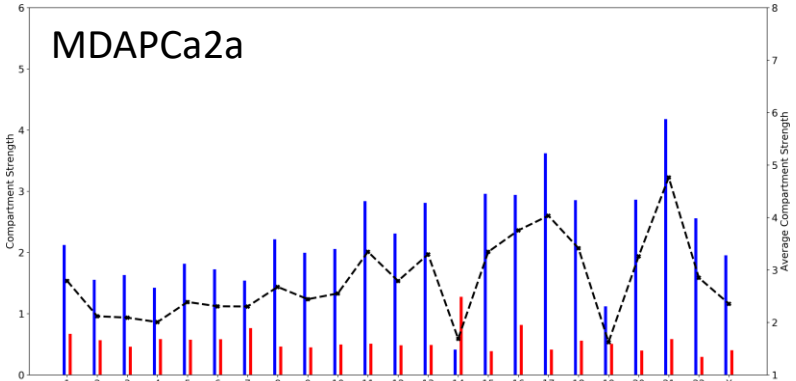
**B** LNCaP



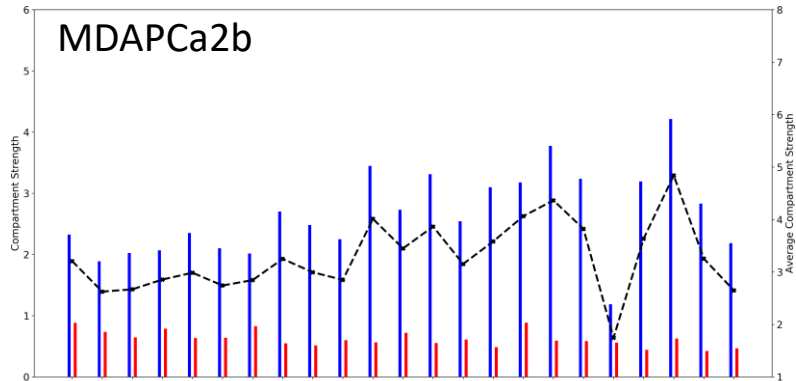
**C** VCaP



**D** MDAPCa2a



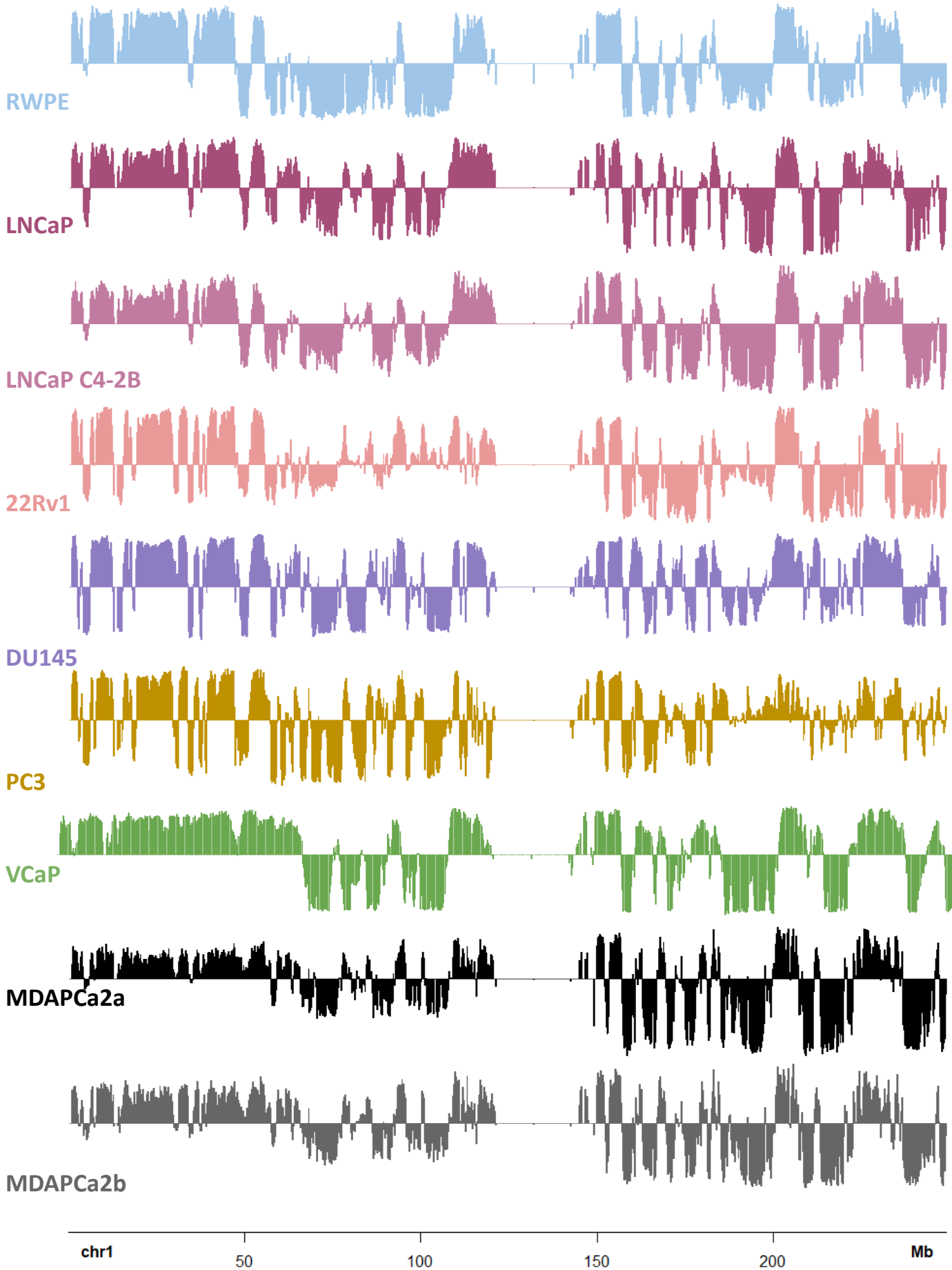
**E** MDAPCa2b



■ A-A interactions  
■ B-B interactions

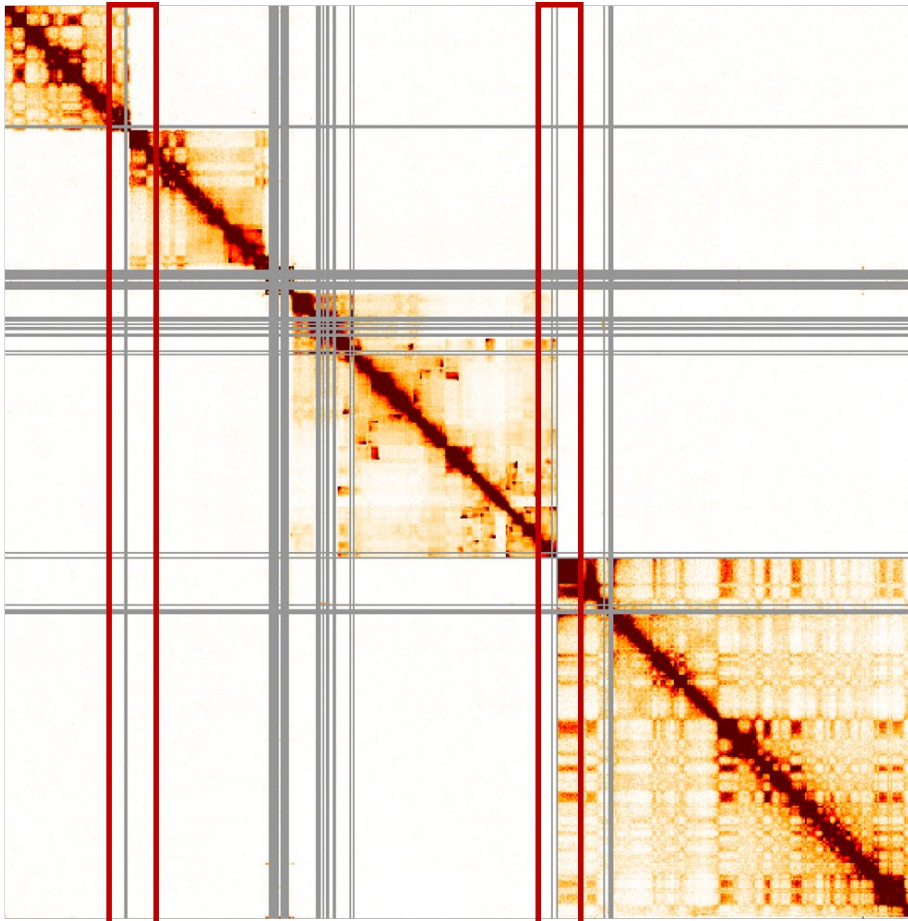
**F**

	1	0.74	0.61	0.63	0.69	0.81
RWPE		1	0.7	0.77	0.82	0.68
LNCaP			1	0.6	0.65	0.56
VCaP				1	0.91	0.63
MDA2A					1	0.68
MDA2B						1
A375						
	RWPE	LNCaP	VCaP	MDA2A	MDA2B	A375

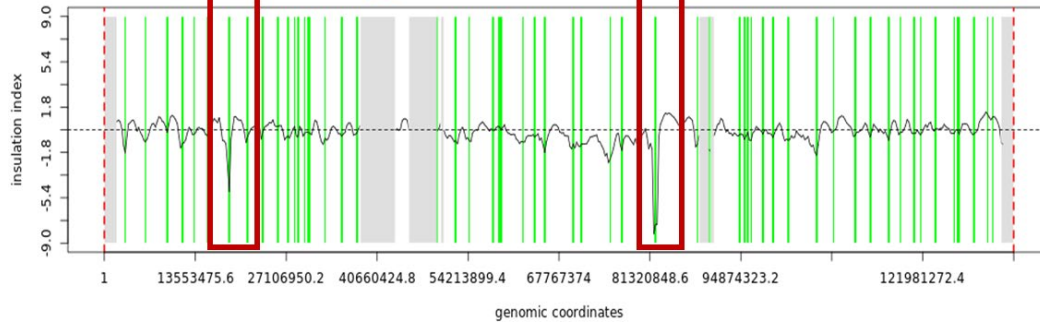


Sup Fig 6

A



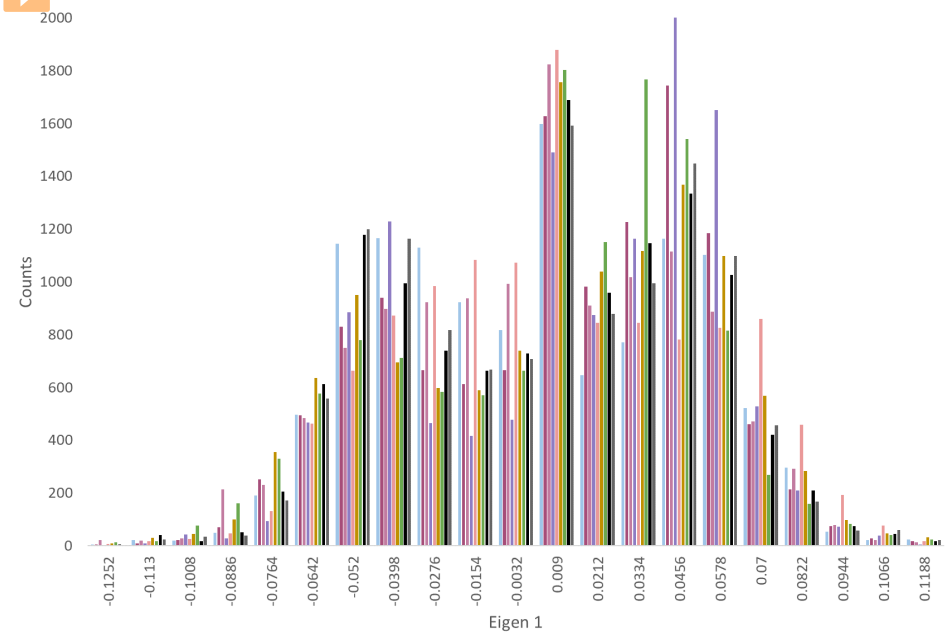
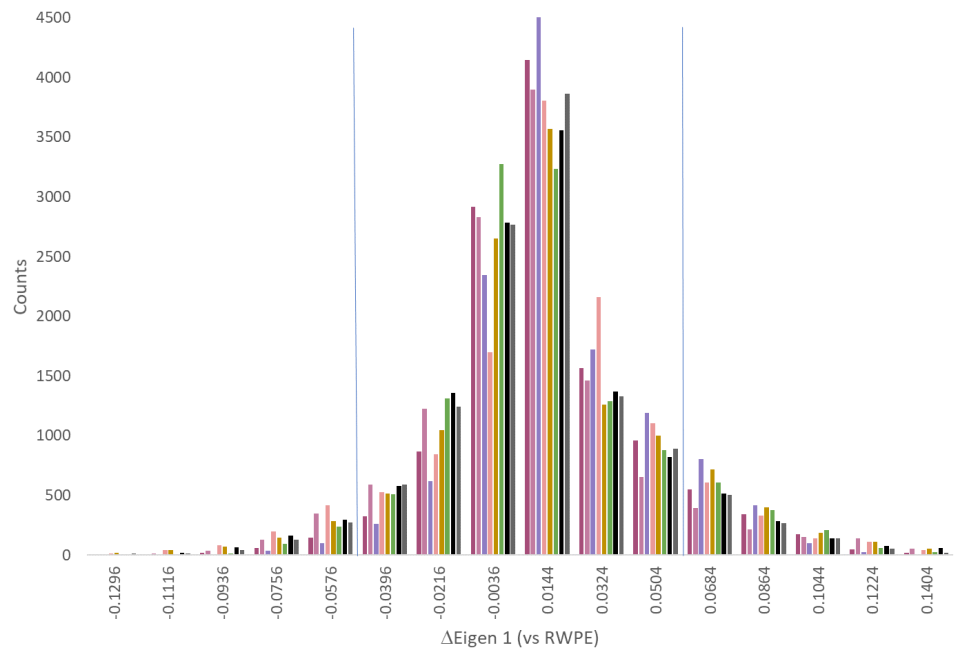
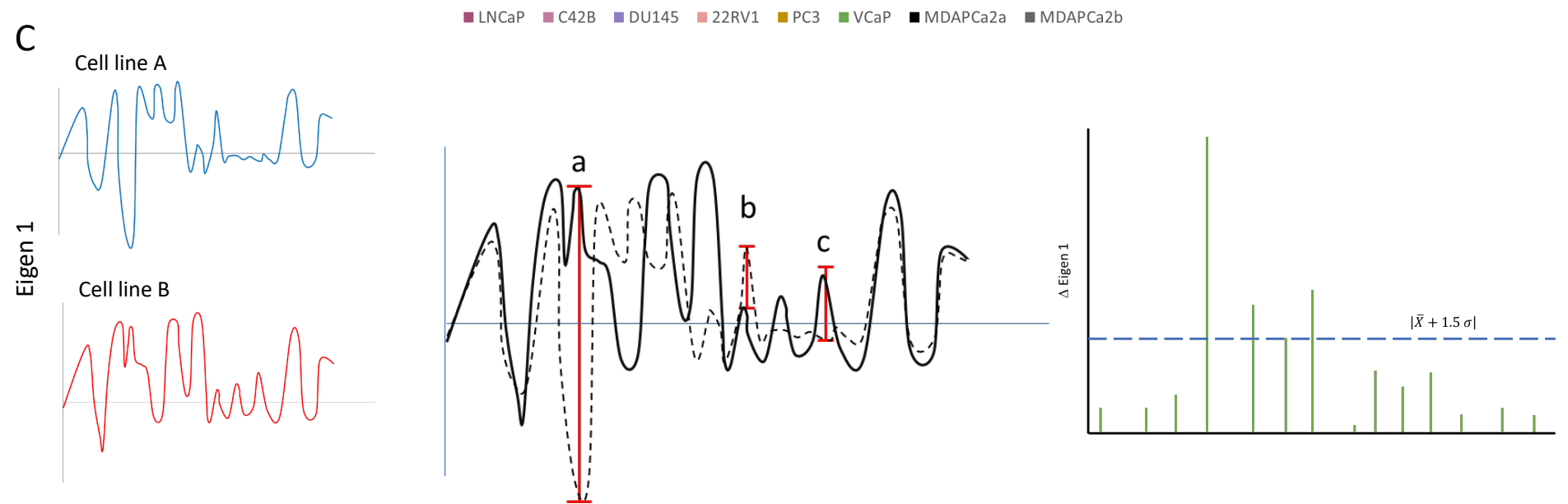
B



C

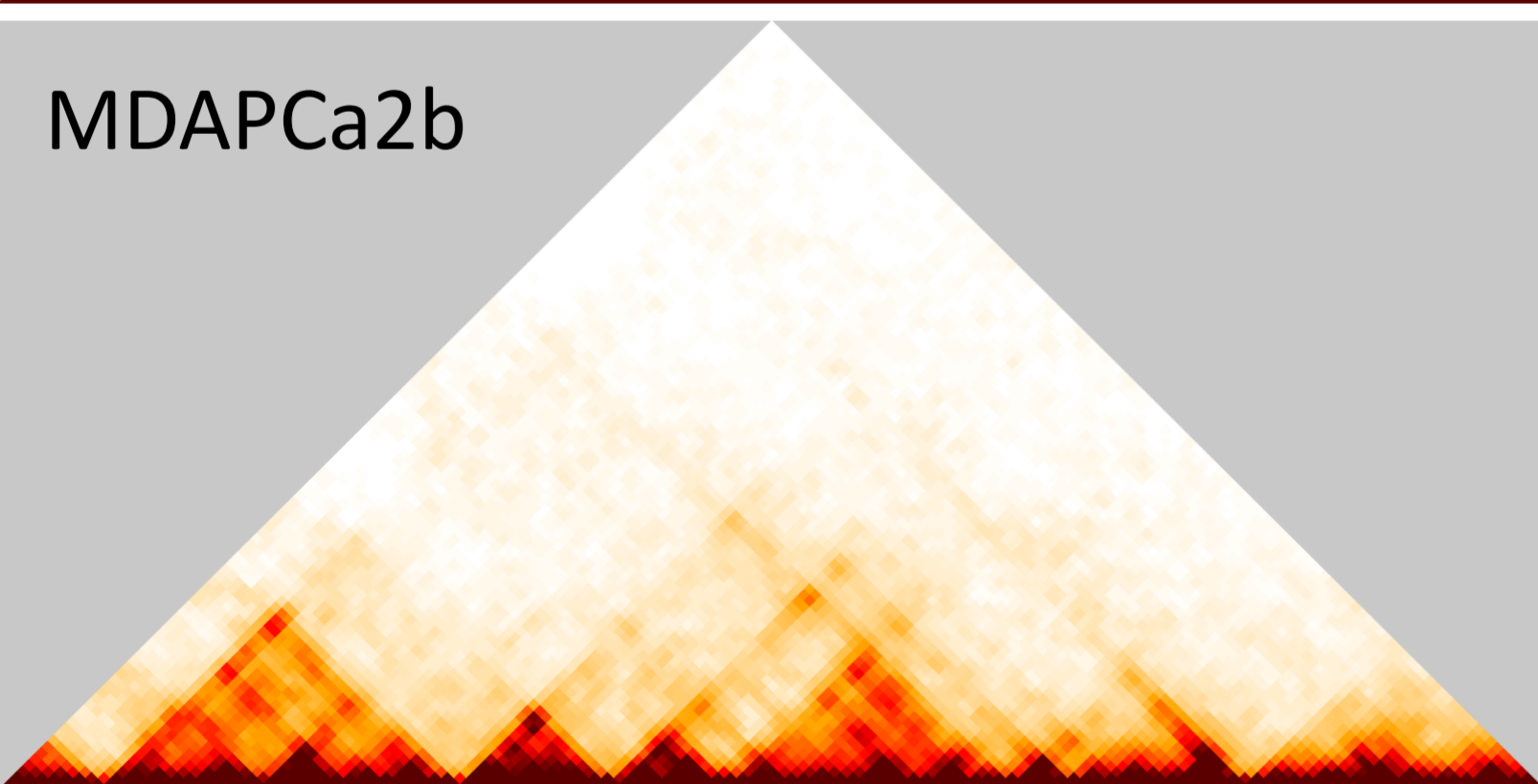
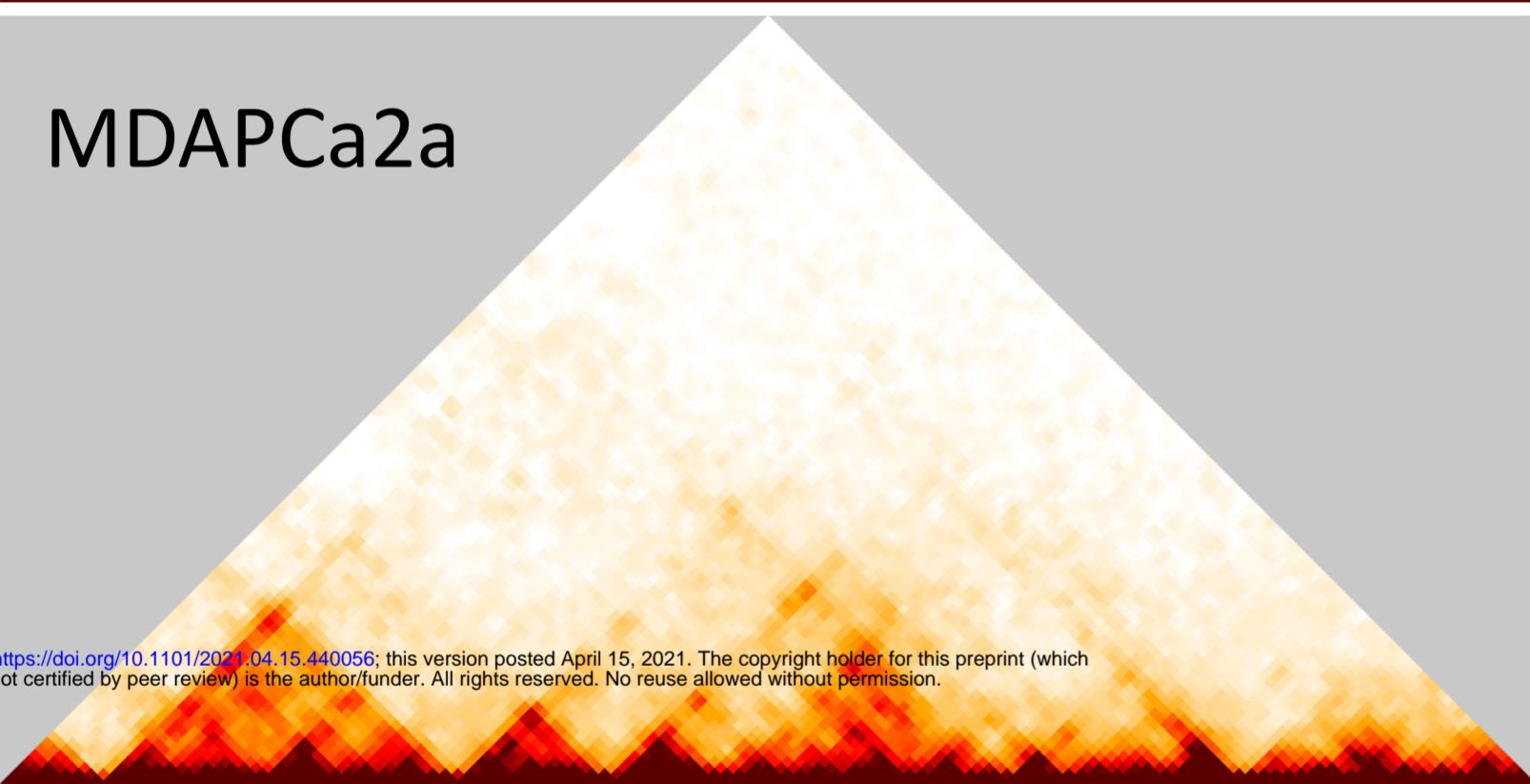
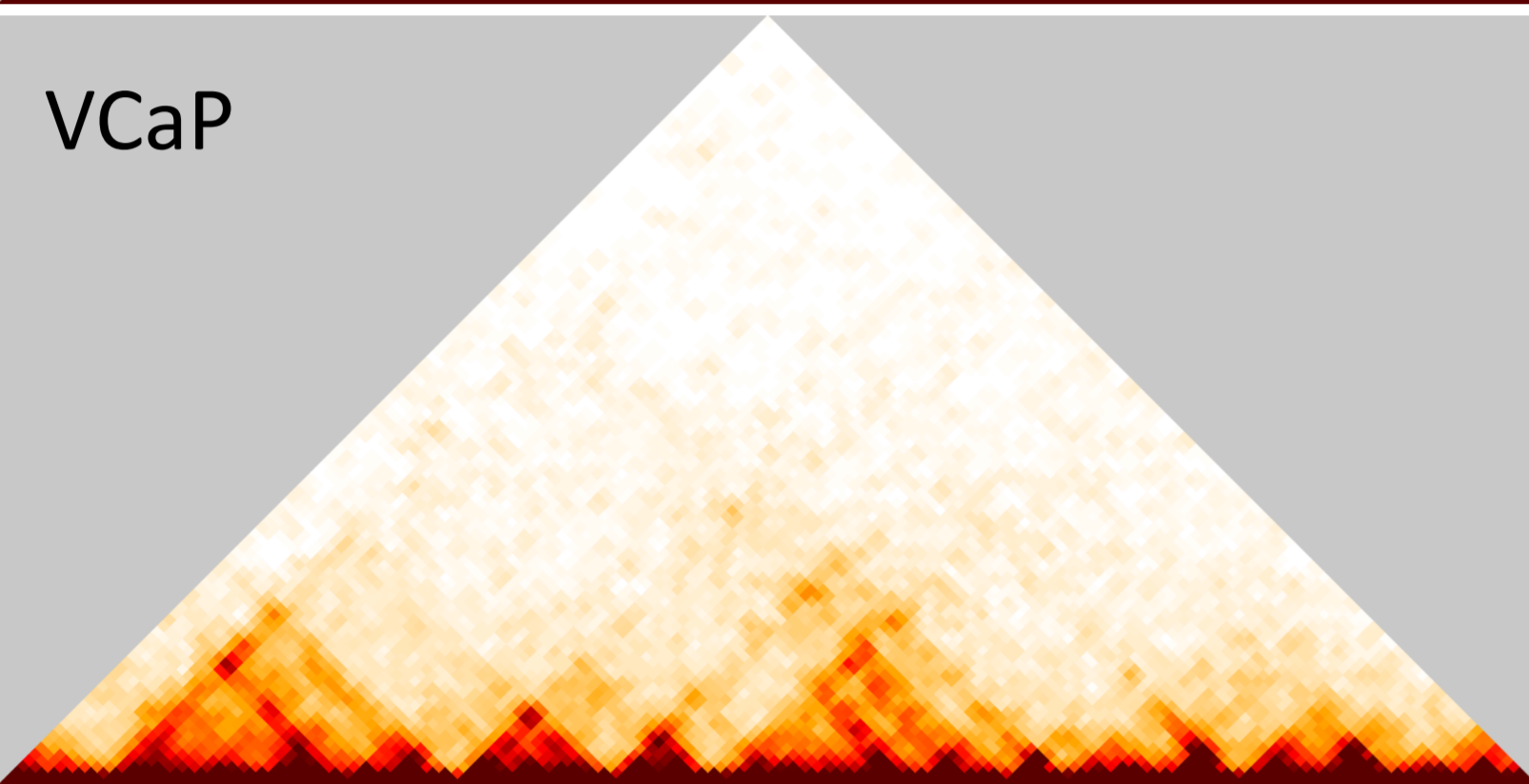
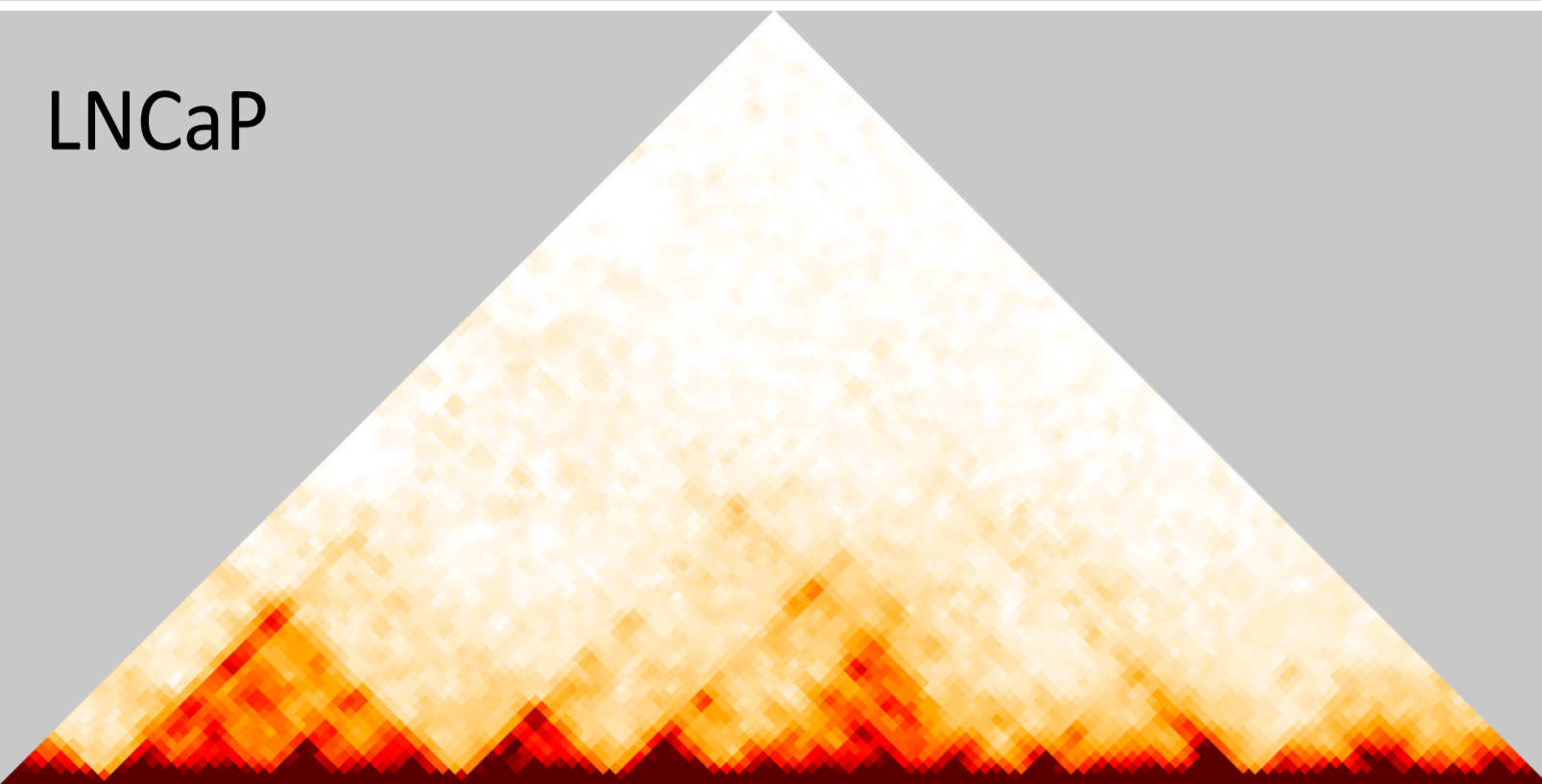
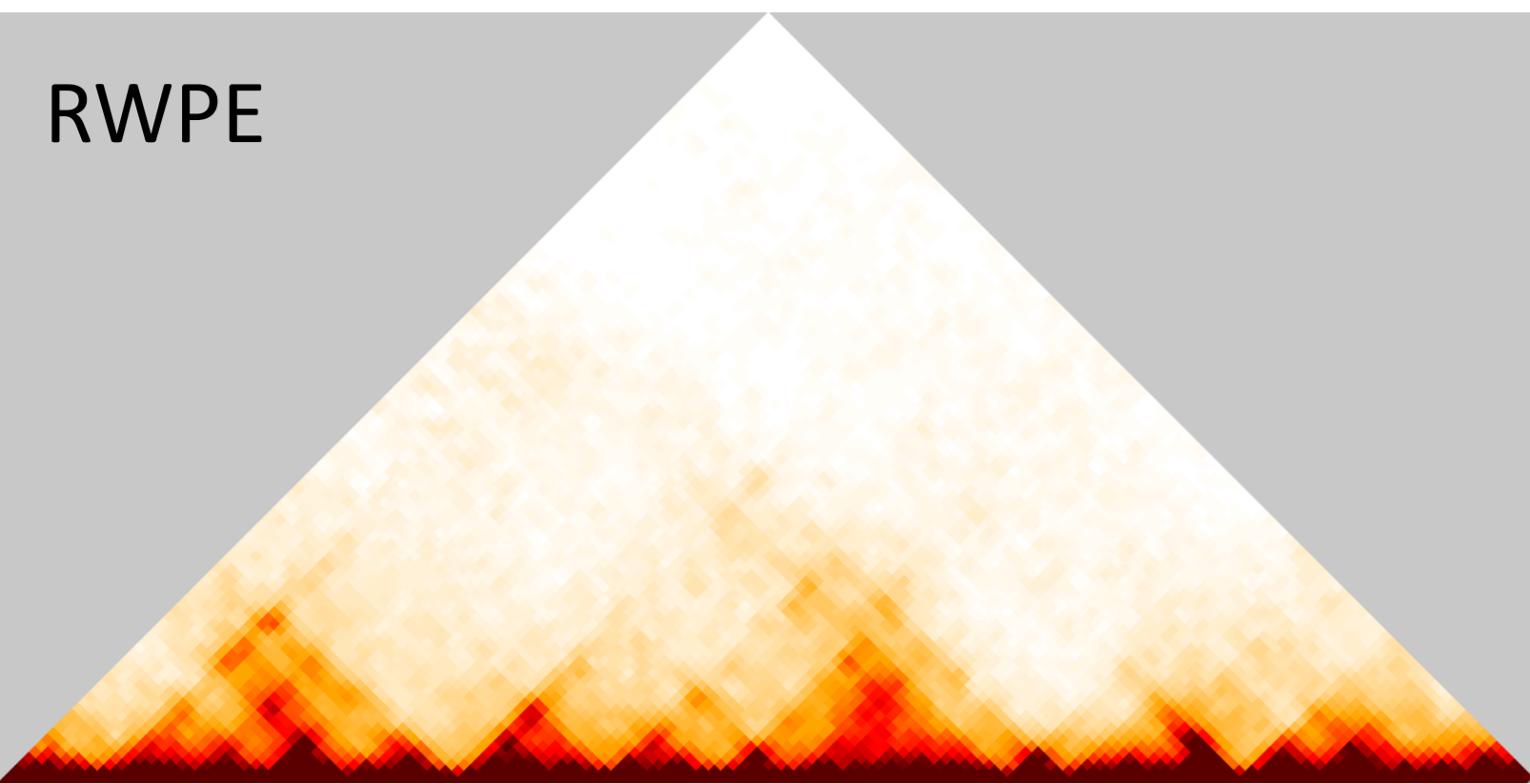
header	start	end	midpoint	insulationScore
6786 hg19 chr10:15000001-15250000	15000001	15250000	15125001	-0.381944518
6787 hg19 chr10:15250001-15500000	15250001	15500000	15375001	-0.466191433
6788 hg19 chr10:15500001-15750000	15500001	15750000	15625001	-0.084644467
6789 hg19 chr10:15750001-16000000	15750001	16000000	15875001	0.084578339
6790 hg19 chr10:16000001-16250000	16000001	16250000	16125001	0.625311169
6791 hg19 chr10:16250001-16500000	16250001	16500000	16375001	0.887754689
6792 hg19 chr10:16500001-16750000	16500001	16750000	16625001	0.726407409
6793 hg19 chr10:16750001-17000000	16750001	17000000	16875001	0.568173736
6794 hg19 chr10:17000001-17250000	17000001	17250000	17125001	0.96685072
6795 hg19 chr10:17250001-17500000	17250001	17500000	17375001	0.179920695
6796 hg19 chr10:17500001-17750000	17500001	17750000	17625001	-0.862118206
6797 hg19 chr10:17750001-18000000	17750001	18000000	17875001	-0.888747144
6798 hg19 chr10:18000001-18250000	18000001	18250000	18125001	-1.1175402
6799 hg19 chr10:18250001-18500000	18250001	18500000	18375001	-2.88607681
6800 hg19 chr10:18500001-18750000	18500001	18750000	18625001	-4.90913542
6801 hg19 chr10:18750001-19000000	18750001	19000000	18875001	-0.733429329
6802 hg19 chr10:19000001-19250000	19000001	19250000	19125001	0.14711439



**A****B****C**

Sup Fig 8

Cluster 18. chr15:47125590-52125590

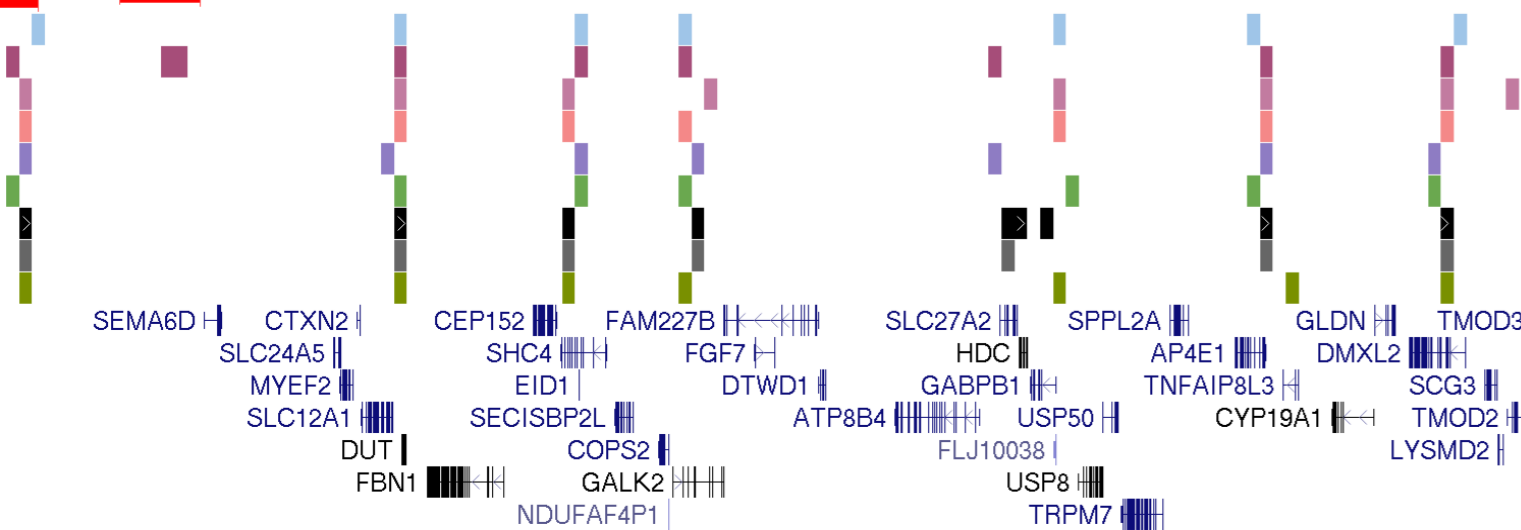


bioRxiv preprint doi: <https://doi.org/10.1101/2021.04.15.440056>; this version posted April 15, 2021. The copyright holder for this preprint (which was not certified by peer review) is the author/funder. All rights reserved. No reuse allowed without permission.

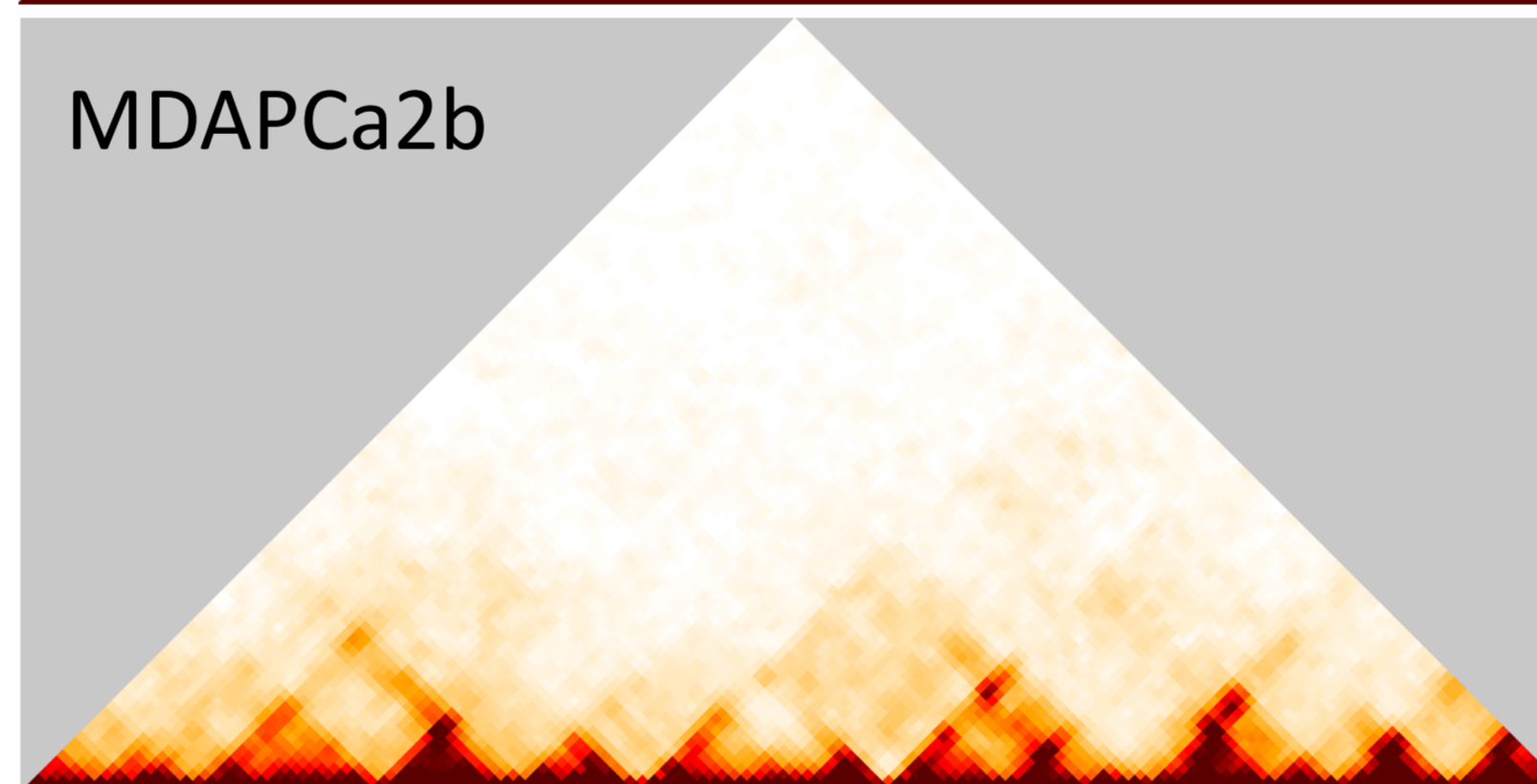
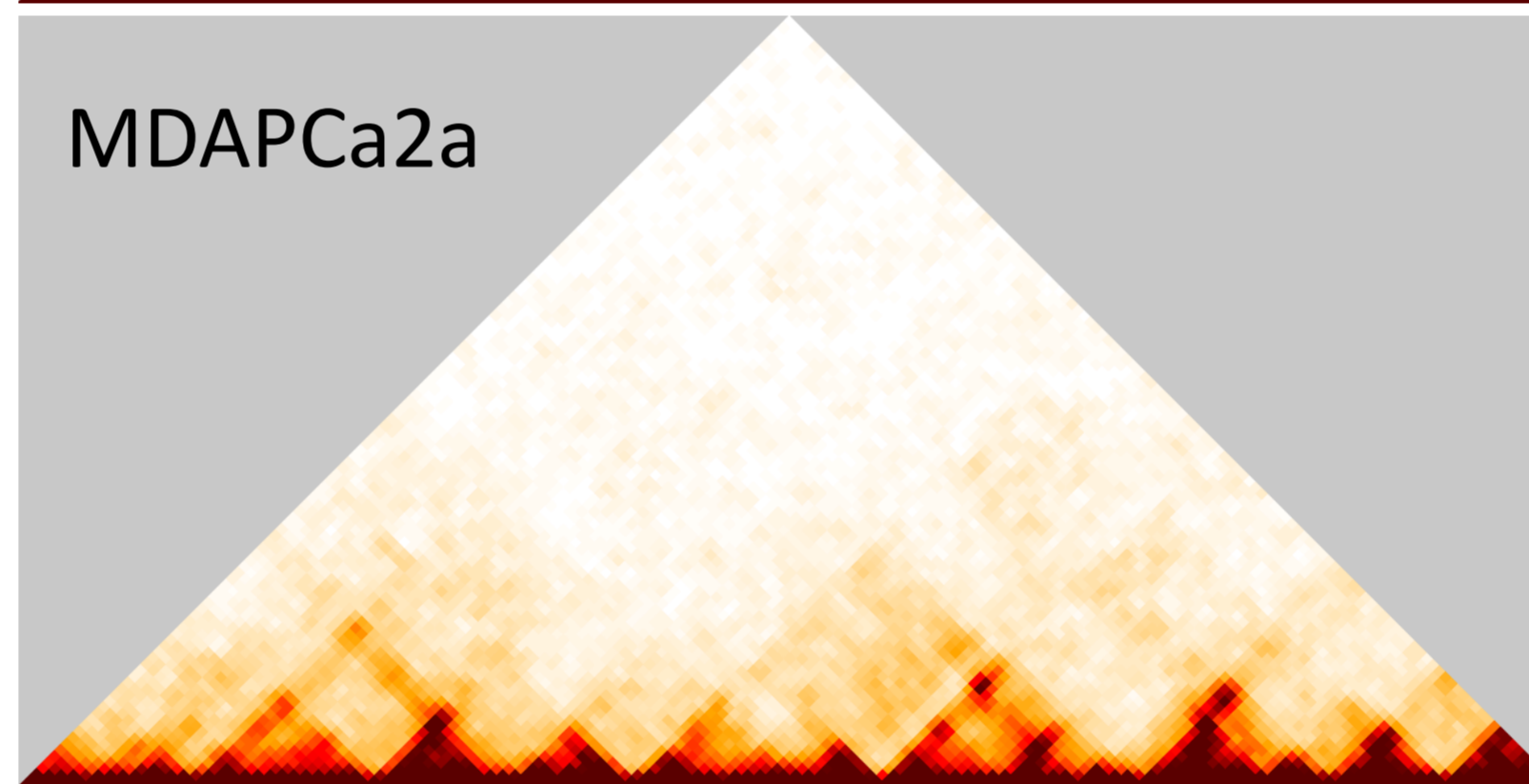
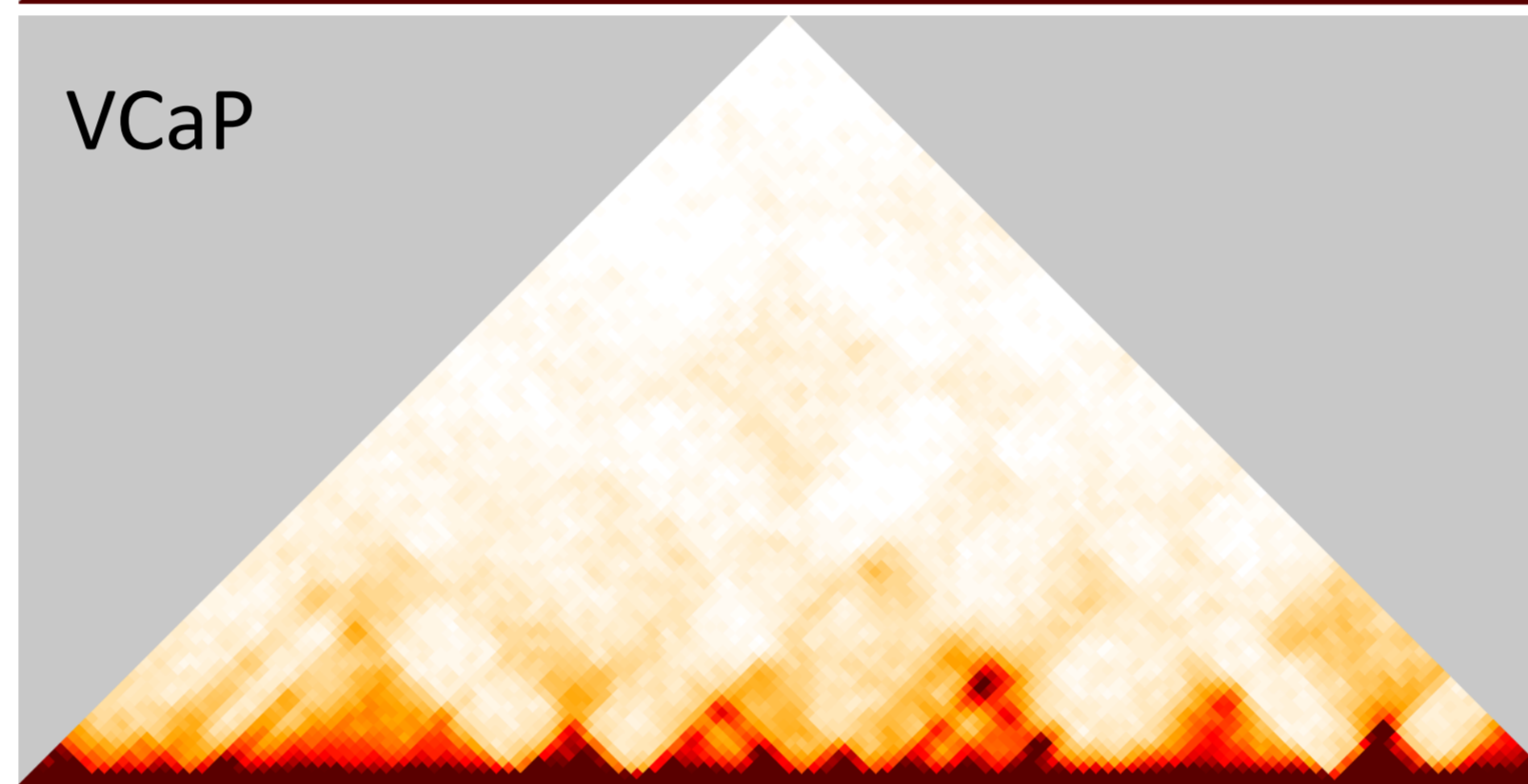
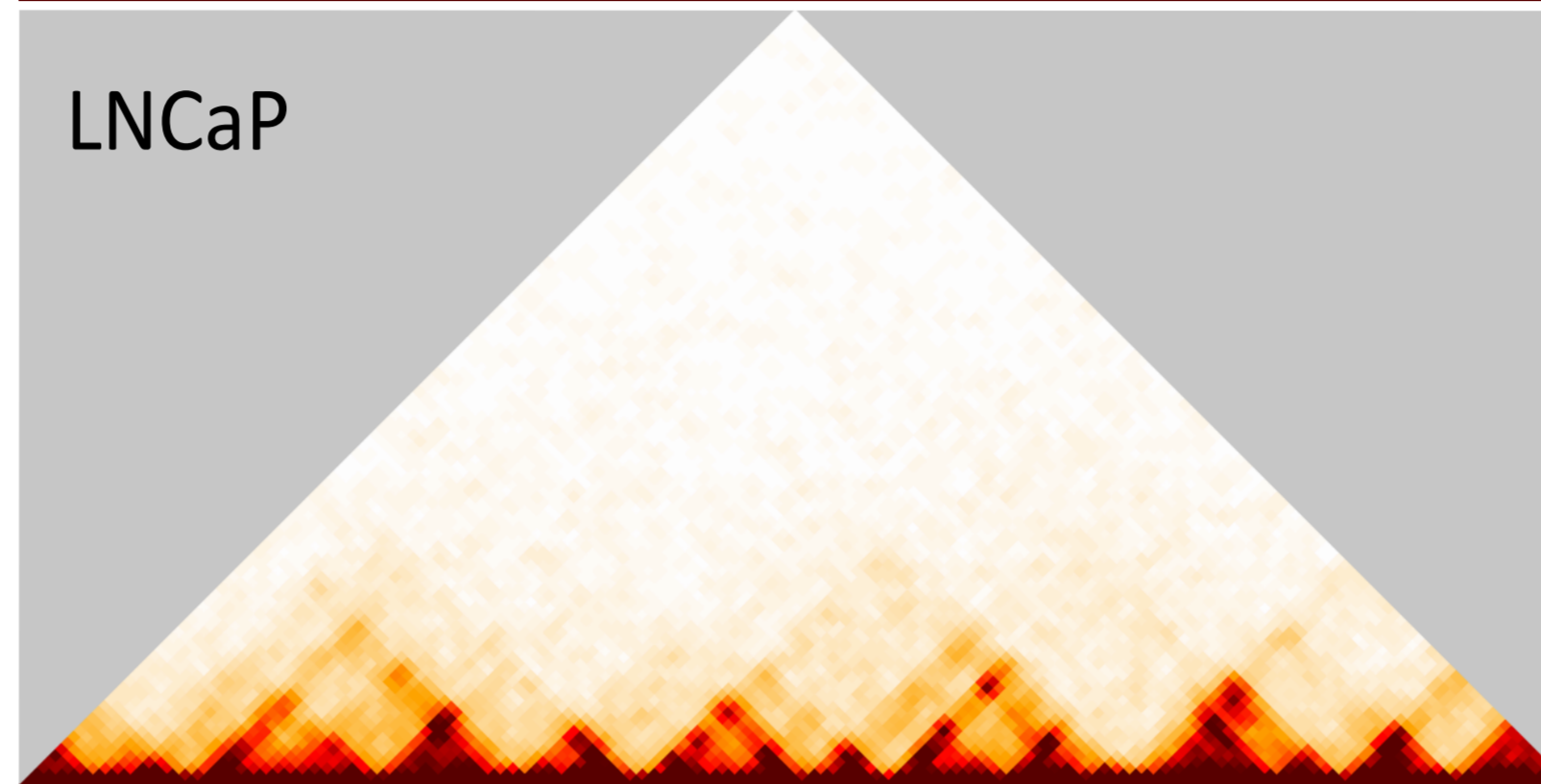
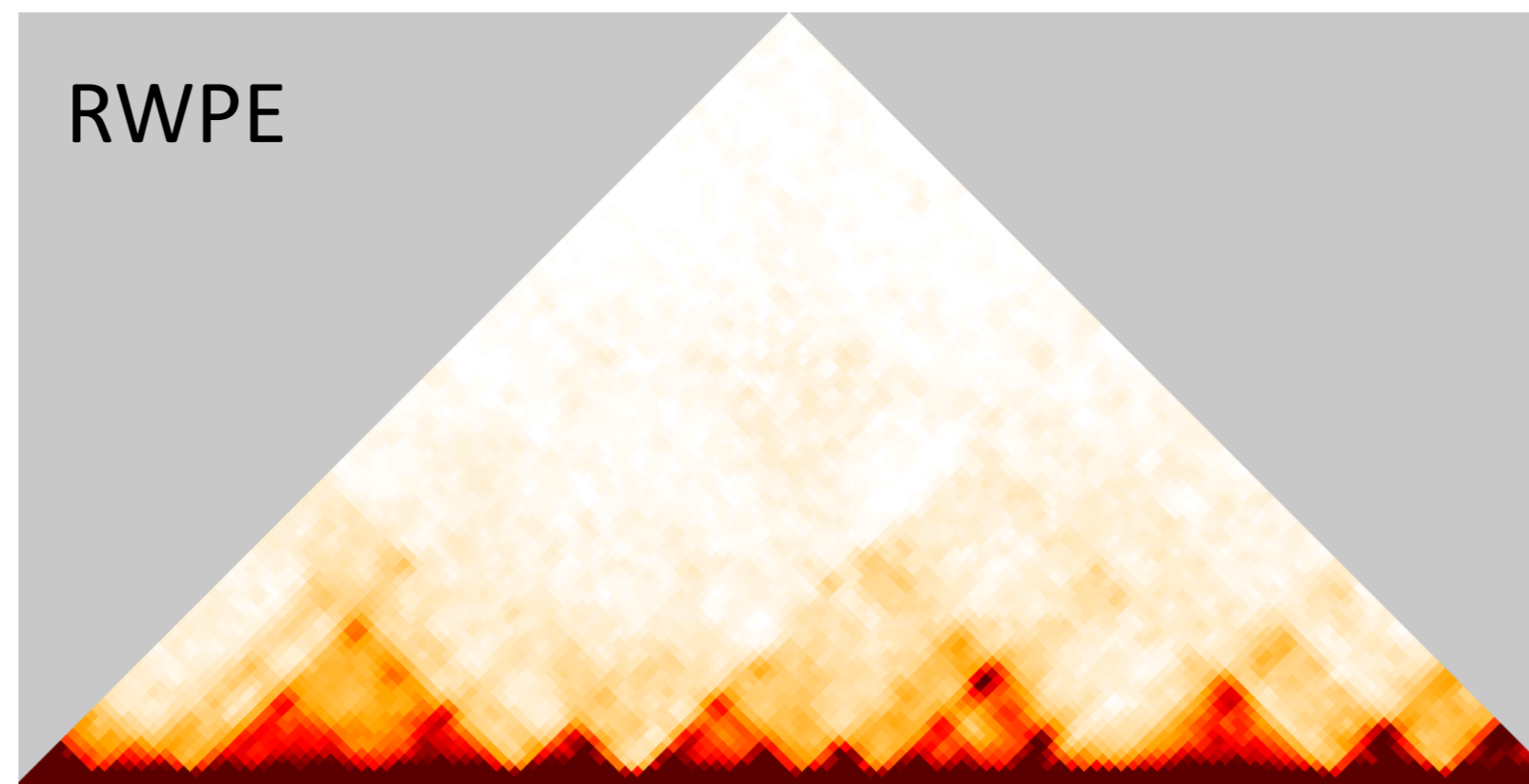
Scale chr15: 48,000,000 48,500,000 49,000,000 49,500,000 50,000,000 50,500,000 51,000,000 51,500,000 52,000,000

RWPE-Eigen1  
LNCaP-Eigen1  
C42B-Eigen1  
22RV1-Eigen1  
DU145-Eigen1  
PC3-Eigen1  
VCaP-Eigen1  
MDA PCa 2A-Eigen1  
MDA PCa 2B-Eigen1

RWPE1-TAD  
LNCaP-TAD  
C42B-TAD  
22RV1-TAD  
DU145-TAD  
VCaP-TAD  
MDA PCa2A-TAD  
MDA PCa2B-TAD  
PC3-TAD



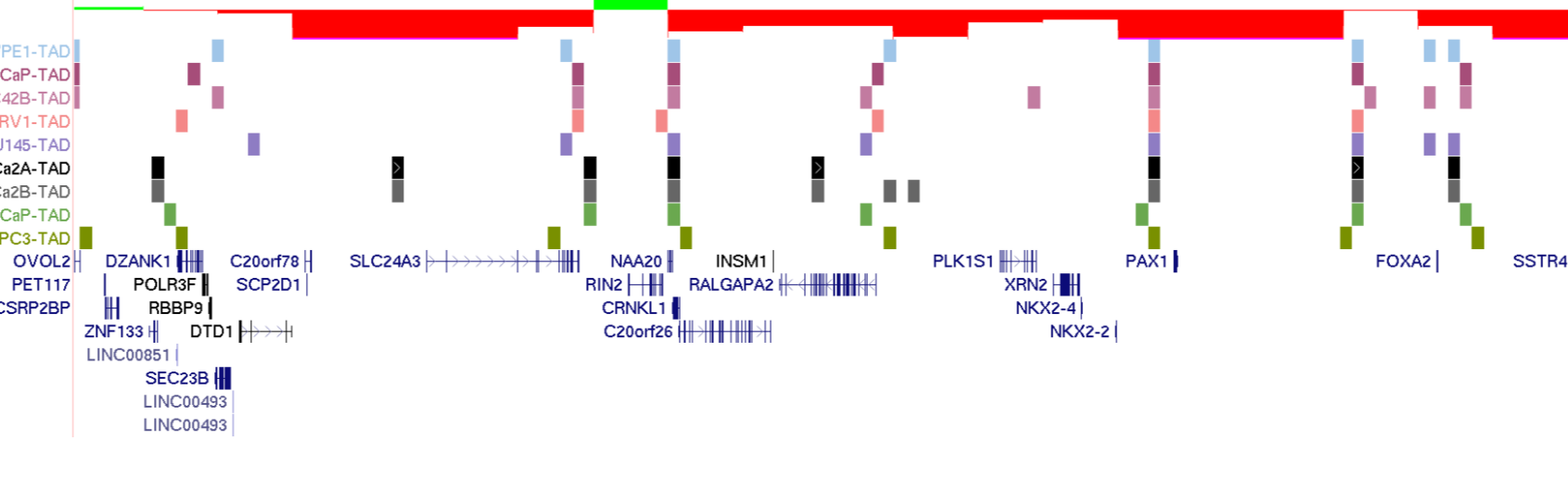
Cluster 5. chr20:18020781-23020781



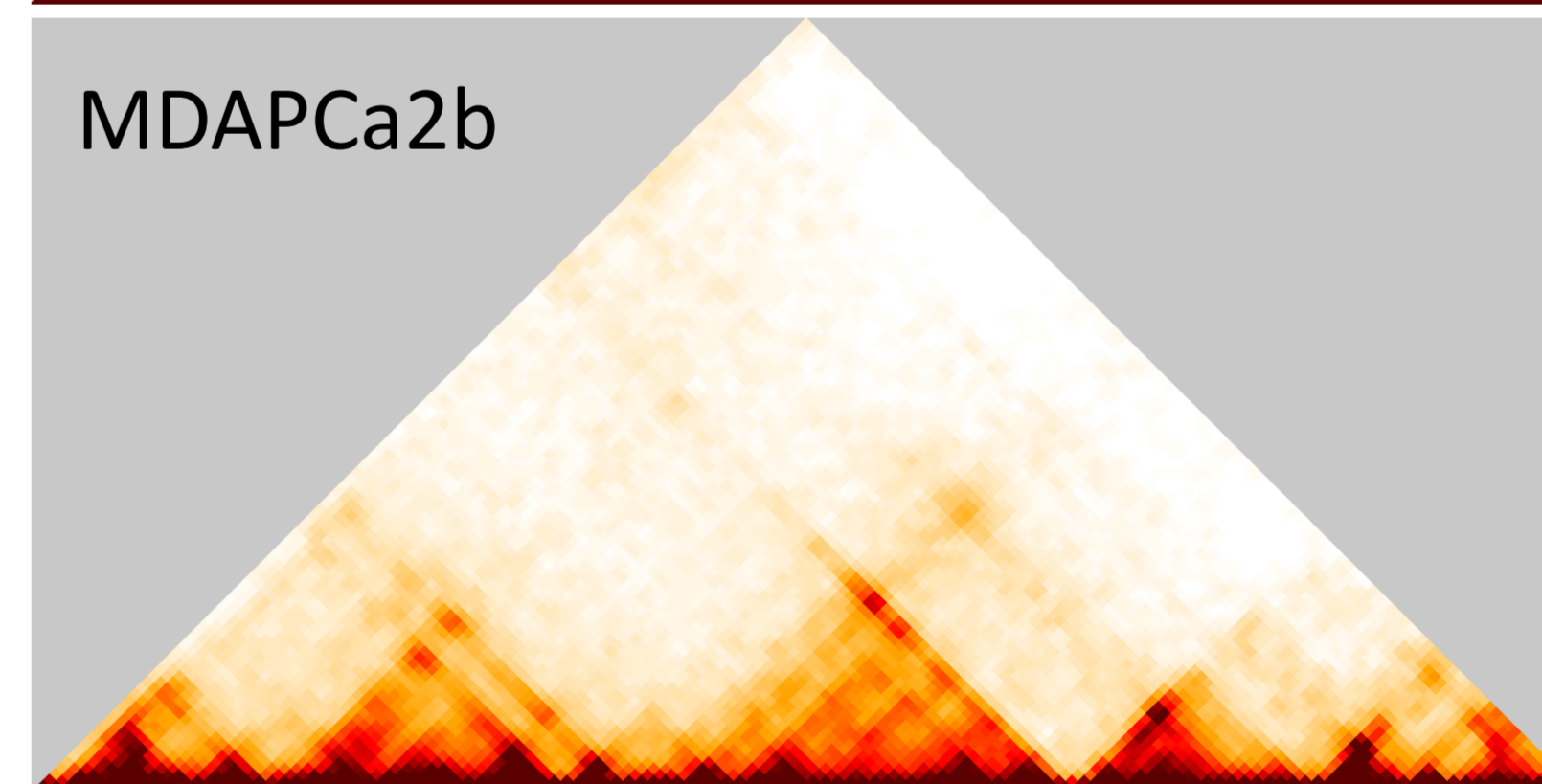
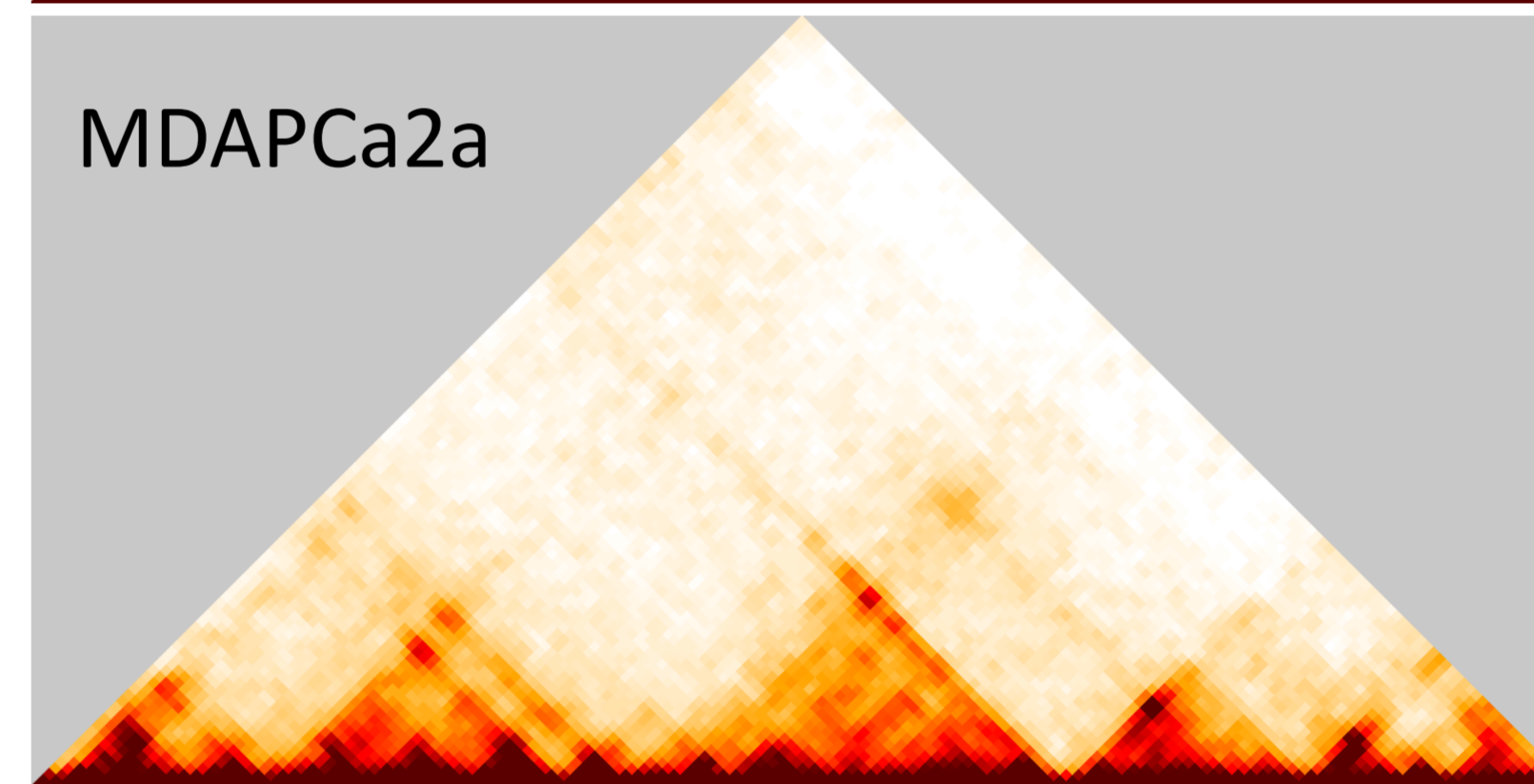
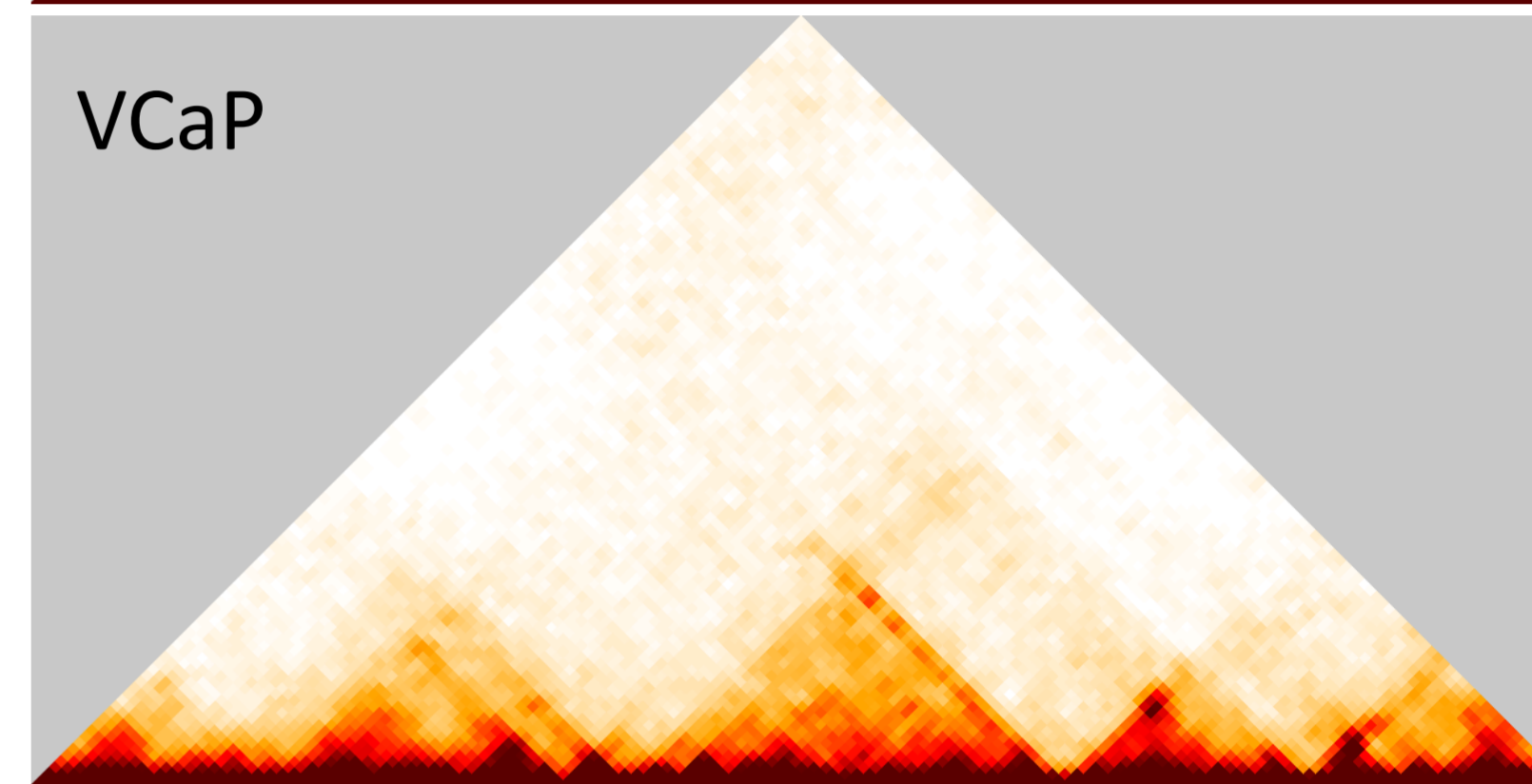
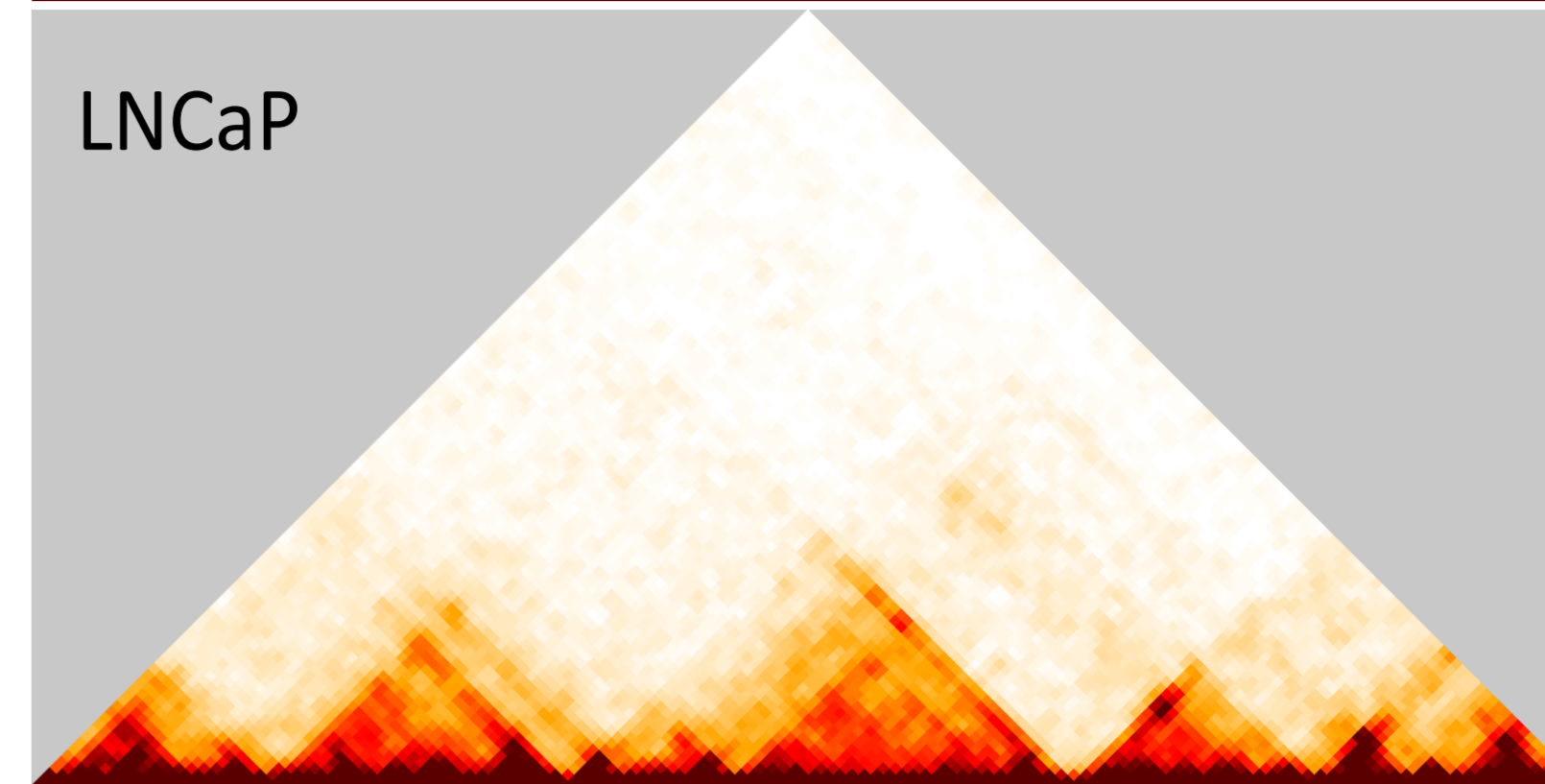
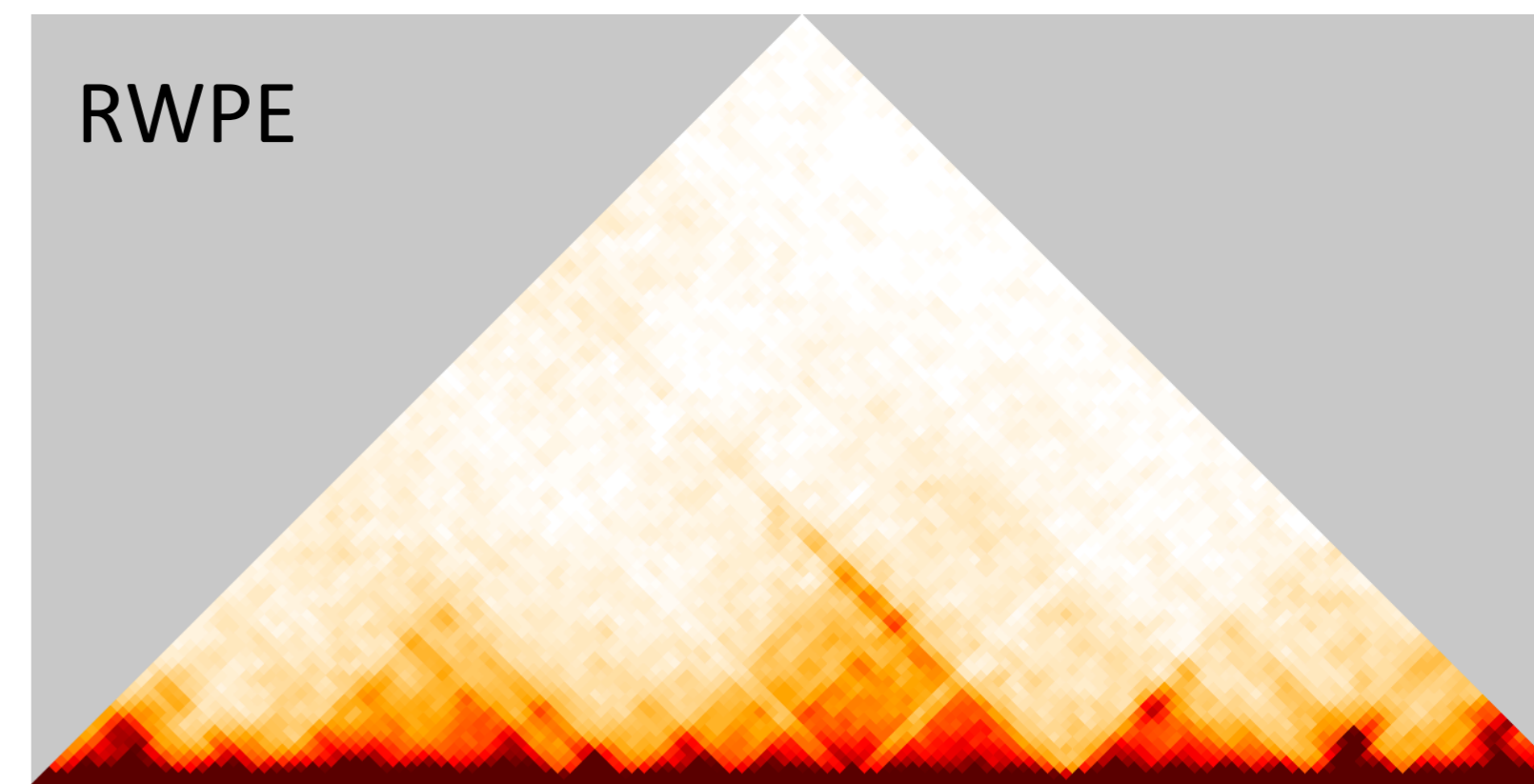
Scale chr20: 18,500,000 19,000,000 19,500,000 20,000,000 20,500,000 21,000,000 21,500,000 22,000,000 22,500,000 23,000,000

RWPE-Eigen1  
LNCaP-Eigen1  
C42B-Eigen1  
22RV1-Eigen1  
DU145-Eigen1  
VCaP-Eigen1  
MDA PCa 2A-Eigen1  
MDA PCa 2B-Eigen1  
PC3-Eigen1

RWPE1-TAD  
LNCaP-TAD  
C42B-TAD  
22RV1-TAD  
DU145-TAD  
VCaP-TAD  
MDA PCa2A-TAD  
MDA PCa2B-TAD  
PC3-TAD



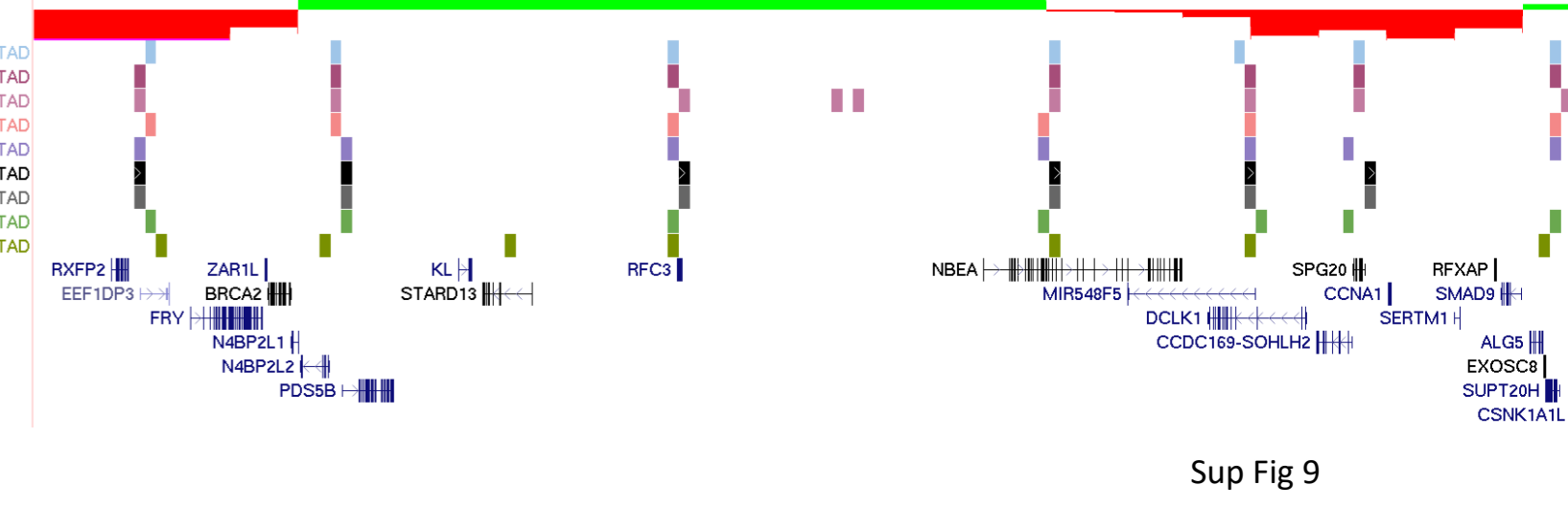
Cluster 4. chr13:32,030,440-37726532



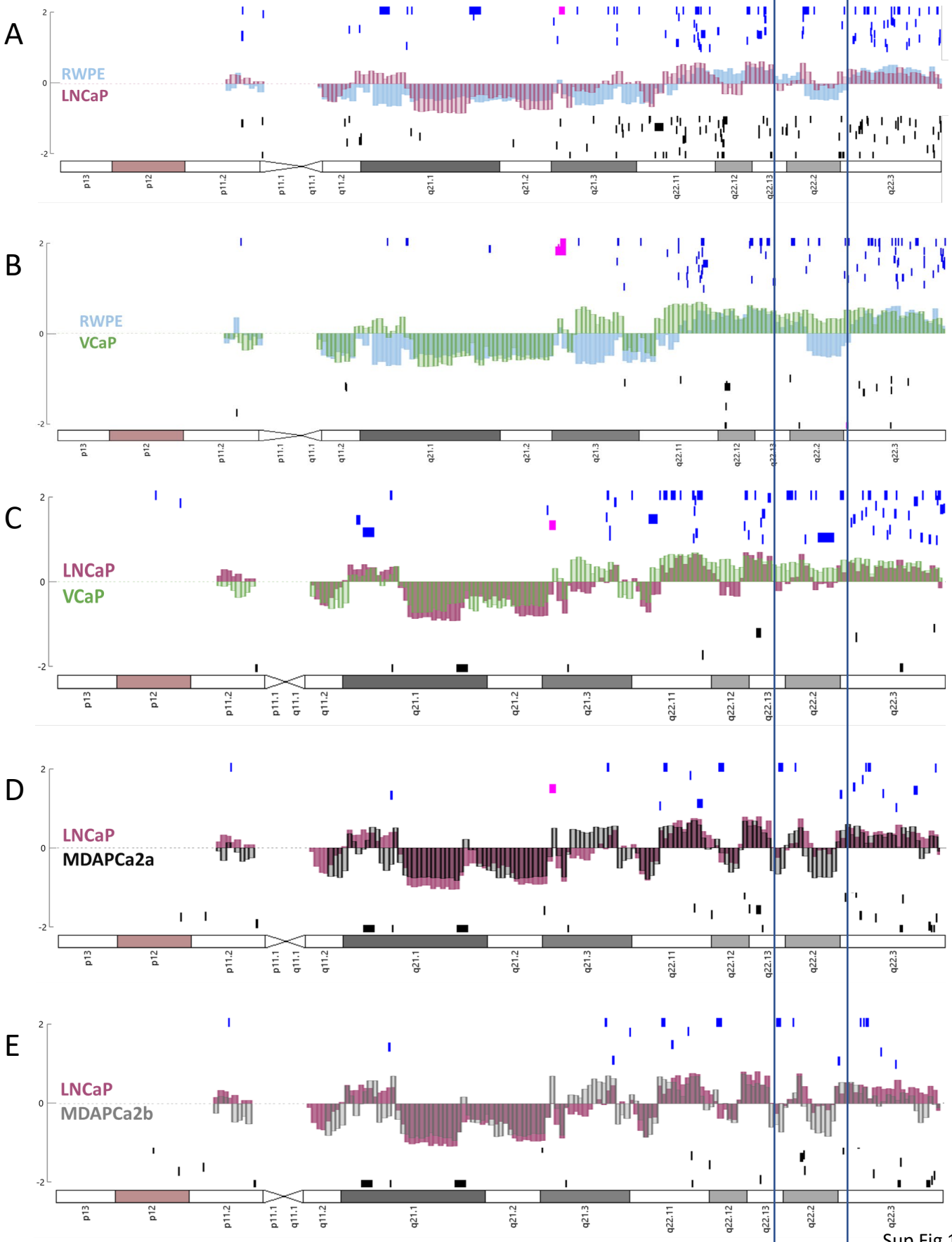
Scale chr13: 32,500,000 33,000,000 33,500,000 34,000,000 34,500,000 35,000,000 35,500,000 36,000,000 36,500,000 37,000,000 37,500,000

RWPE-Eigen1  
LNCaP-Eigen1  
C42B-Eigen1  
22RV1-Eigen1  
DU145-Eigen1  
VCaP-Eigen1  
MDA PCa 2A-Eigen1  
MDA PCa 2B-Eigen1  
PC3-Eigen1

RWPE1-TAD  
LNCaP-TAD  
C42B-TAD  
22RV1-TAD  
DU145-TAD  
VCaP-TAD  
MDA PCa2A-TAD  
MDA PCa2B-TAD  
PC3-TAD



APP



**Supplementary Table 1**

<b>Cell Line</b>	<b>Publication</b>	<b>GEO #</b>	<b>Replicate</b>	<b>Unique Valid Pairs</b>	<b>Total Valid Pairs in Replicates Combined</b>
RWPE	Luo et al., 2017: PMID: 29117547	GSE98898	R1	233,612,639	469,519,763
RWPE	Luo et al., 2017: PMID: 29117547	GSE98898	R2	235,907,124	
LNCaP	This paper	GSE172099	R1	105,867,365	105,867,365
VCaP	This paper	GSE172099	R1	40,931,888	348,741,539
VCaP	This paper	GSE172099	R2	40,628,914	
VCaP	This paper	GSE172099	R2	268,873,668	
MDA-PCA2a	This paper	GSE172099	R1	62,552,796	140,655,040
MDA-PCA2a	This paper	GSE172099	R2	78,102,244	
MDA-PCA2b	This paper	GSE172099	R1	55,097,322	210,944,948
MDA-PCA2b	This paper	GSE172099	R2	155,847,626	
22RV1	Rhie et al, 2019 PMID: 31515496	GSE118629	R2	320,370,533	320,370,533
C42B	Rhie et al, 2019 PMID: 31515496	GSE118629	R1	224,597,478	224,597,478
DU145	This paper	GSE172099	R1	157,348,192	309,278,852
DU145	This paper	GSE172099	R2	152,073,748	
PC3	This paper	GSE172099	R1	41,986,034	170,057,873
PC3	This paper	GSE172099	R2	128,072,419	

Δ Eigen 1 +1.5 STD (B to A)					
ABCC4	DR1CH1	IGF1	NBEA	RTN1	WNT5A
ACSL5	DTWD1	IGLL1	NBEA	RWDD2B	WRB
ACTR3C	DTWD2	IGSF5	NDUFAP4P1	RXFP2	XKR9
ADAMTS5	DYNLRB2	INSM1	NETO1	SCAF4	XRN2
ADRA2A	EDA	INSM1	NKX2.1	SDC2	ZBED6CL
AKAP7	EEF1DP3	ITGA9	NKX2-2	SECISBP2L	ZDHHC6
ALDH18A1	EID1	JPH1	NKX2-2	SEMA6A	ZNF134
ANK3	ELOC	KEL	NKX2-4	SETBP1	ZNF17
AP3S1	ENPP3	KRTAP13-1	NR3C2	SFTA3	ZNF28
AP5M1	ENTPD1	KRTAP13-3	NUP37	SH3BGR	ZNF302
APOH	EPB41L2	KRTAP13-4	NXK2-8	SHC4	ZNF302
AQP4	EPHB6	KRTAP15-1	ONECUT2	SHOC2	ZNF320
AQPEP	ERC2	KRTAP19-1	OPRK1	SLC24A3	ZNF329
AR	EXOC5	KRTAP19-2	OR6W1P	SLC25A21	ZNF331
ARG1	EYA	KRTAP19-3	OR9A2	SLC26A5	ZNF350
ARL1	FAM122A	KRTAP19-4	OR9A2	SLC27A2	ZNF468
ARL14EPL	FAM155B	KRTAP19-5	OTX2	SLC4A4	ZNF544
ASZ1	FAM227B	KRTAP19-6	PARPBP	SLCO5A1	ZNF547
ATG12	FAM3B	KRTAP19-7	PART1	SMCO4	ZNF548
ATP8B4	FAM3B	KRTAP20-1	PAX1	SOD1	ZNF550
AXIN2	FAM81B	KRTAP20-4	PAX1	SORBS1	ZNF551
B3GALT5	FBN1	KRTAP22-1	PAX9	SOX21	ZNF599
BACE2	FECH	KRTAP22-2	PCA3	SOX4	ZNF600
BACH1	FGF7	KRTAP6-1	PDE4D	SPIC	ZNF606
BCAS3	FOXA2	KRTAP6-2	PGM5	ST8SIA3	ZNF610
BMP6	FOXB2	KRTAP6-3	PI15	STAU2	ZNF613
BRCA2	FREM1	LACTB2	PIP	STXBP6	ZNF615
BTG3	FRMD3	LCA5L	PIP5K1B	SULF1	ZNF677
CASC15	FRY	LRIG1	PLAC4	SYCP3	ZNF765
CASP2	FRY	LRRC61	PLAC4	SYT4	ZNF776
CASP7	FUT8	LRRC9	PLK1S1	TBX2	ZNF792
CCDC53	FXN	LTN1	PMCH	TBX4	ZNF813
CCDC67	FZD1	LVRN	PPM1A	TCTN3	ZNF816
CCT8	GALK2	LY96	PPM1H	TECTB	ZNF880
CDK1	GDAP1	MAP3K7CL	PPM1H	TGD	ZSCAN18
CDK14	GET	MBIP	PRKAGG	TMEM139	
CDO1	GGT1	MBNL2	PRKCA	TMEM252	
CDYL2	GIMAP2	MCTF1	PRKD1	TMEM26	
CEP112	GIMAP6	MED23	PRL	TMEM70	
CEP152	GIMAP7	MIPOL1	PRUNE	TMPRSS2	
CFAP61	GIMAP8	mir 5681A	PRUNE2	TRAM1	
CFTR	GLYATL1	MIS18A	PSMC2	TRIM36	
CHPT1	GNA13	MPHOSPH6	PTDSS1	TRPV5	
CHST9	GNAZ	MRAP	RAB36	TRPV6	
CNPTAB	GPAM	MSC	RALGAPA2	TSPYL5	
COMD10	GPC6	MTERF3	RALGAPA2	TTC6	
COMMMD10	GPR180	MTERFD1	RARRES2	UBE2W	
COPS2	GRAMD1A	MX1	RELN	UGT2A1	
CPQ	GRAMDIA	MX2	REPIN1	UGT2A2	
CRNKL1	GSTK1	MYBPC1	RFC3	UGT2B4	
CRNKL1	GUCY2GP	MYRIP	RFC3	URB1	
CXADR	GUSBP11	N4BP2L1	RGS9	USP16	
CXCL12	HDC	N4BP2L1	RHOBTB1	USP25	
DACH1	HUNK	N6AMT1	RIN2	UTP20	
DEPDC1B	IDNK	NAA20	RIT2	VLDLR	
DMXL1	IFRD1	NACA2	RTDR1	VTI1A	

Δ Eigen 1 -1.5 STD (A to B)		
ARSF	IVL	NRG1
BLID	KCNJ15	PALM2
BMP2	KCNJ6	PAX3
BMP5	KDSR	PCNA
CAMK4	LCE1A	PITPNB
CAPNS2	LCE1B	PRKCQ
CCDC140	LCE1C	PRND
CMKLR1	LCE1D	PRNP
COL21A1	LCE1E	PRNT
COL8A1	LCE1F	PROKR2
CRAT37	LCE2A	PRR9
CYLD	LCE2B	PTPN3
DCBLD2	LCE2C	SALL1
DCHS2	LCE2D	SEMA3A
DLC1	LCE3A	SERPINB12
DMD	LCE3B	SERPINB5
DSCR4	LCE3C	SFTA1P
DSCR8	LCE3D	SGCZ
ERG	LCE3E	SLC6A2
ESD	LCE4A	SLCO3A1
FAM83B	LCE6A	SMCP
FTHL17	LPCAT2	SORL1
GFRAL	MMP2	ST3GAL6
HCRTR2	MN1	STARD4
HMGCLL11	MTAP	STARD4-
IL15	MXRA5	AS1
IL22	NALCN	SV2B
IL26	NOD2	TENM3
ITGBL1	NREP	TINAG

Supplementary Table 2

<b>1</b> TMRSS2 BACE2 PLAC4 MX1 MX2 FAM3B	<b>12</b> ABCC4 MBNL2 GPR180 TGDS GPC6 SOX21	<b>29</b> ZNF765 ZNF813 ZNF331 ZNF600	<b>39</b> RAB36 GNAZ RTDR1	<b>53</b> STAU2 UBE2W ELOC TMEM70 LY96 JPH1 GDAP1 PI15 mir 5681A PI15	<b>Unclassified</b> ADAMT55 ADRA2A AR ASZ1 BACH1 BMP6 CASP7 CDYL2 CFTR COMMD10 CXCL12 DACH1 EDA ENPP3 FAM155B FREM1 FUT8 IFRD1 ITGA9 LRIG1 MIPOL1 MTERFD1 MYRIP NETO1 NKX2.1 NR3C2 OPRK1 OR6W1P OTX2 PPM1H PRUNE2 SETBP1 SHOC2 SLC4A4 TRIM36 USP16 USP25 DYNLRB2 GGT1 GLYATL1 GRAMD1A MPHOSPH6 PPM1A PRKD1 STXBP6 URB1 VLDLR	<b>1</b> KCNJ6 DSCR4 DSCR8 KCNJ15 ERG	<b>60</b> CAMK4 STARD4 NREP
<b>2</b> WNT5A ERC2	<b>14</b> MBIP SFTA3 NXK2-8 PAX9 SLC25A21	<b>30</b> ZNF28 ZNF468 ZNF320 ZNF816 ZNF547	<b>40</b> IGLL1 DR1CH1 GUSBP11	<b>54</b> MTERF3 PTDSS1 SDC2 CPQ TSPYL5	<b>6</b> IVL LCE1A LCE1B LCE1C LCE1D LCE1E LCE1F LCE2A LCE2B LCE2C LCE2D LCE3A LCE3B LCE3C LCE3D LCE3E LCE4A LCE6A PRR9 SLC6A2 SMCP	<b>63</b> FAM83B HCRTR2 GFRAL HMGCLL11 BMP5 COL21A1	<b>63</b> FAM83B HCRTR2 GFRAL HMGCLL11 BMP5 COL21A1
<b>3</b> FZD1 CDK14	<b>15</b> EXOC5 AP5M1	<b>31</b> ZNF548 ZNF17 ZNF550 ZNF134 ZNF551 ZNF776 ZNF606 ZSCAN18 ZNF329 ZNF544 BTG3	<b>43</b> CDO1 AP3S1 LVRN COMD10 SEMA6A AQPEP ARL14EPL ATG12	<b>56</b> PGM5 PIP5K1B FAM122A PRKAGG TMEM252 FXN	LCE1D LCE1E LCE1F LCE2A LCE2B LCE2C LCE2D LCE3A LCE3B LCE3C LCE3D LCE3E LCE4A LCE6A PRR9 SLC6A2 SMCP	<b>Unclassified</b>	<b>Unclassified</b>
<b>4</b> RXFP2 EEF1DP3 FRY BRCA2 N4BP2L1 RFC3 NBEA	<b>16</b> RTN1 LRRC9	<b>34</b> CXADR NGAMT1	<b>44</b> DTWD2 DMXL1	<b>57</b> PRUNE PCA3 FOXB2	LCE2D LCE3A LCE3B LCE3C LCE3D LCE3E LCE4A LCE6A PRR9 SLC6A2 SMCP	<b>Unclassified</b>	<b>Unclassified</b>
<b>5</b> SLC24A3 RIN2 NAA20 CRNKL1 CFAP61 INSM1 RALGAPA2 PLK1S1 XRN2 NKX2-4 NKX2-2 PAX1 FOXA2 TTC6	<b>17</b> UGT2B4 UGT2A1 UGT2A2	<b>35</b> LTN1 RWDD2B CCT8 MAP3K7CL KRTAP13-1	<b>45</b> PDE4D PART1 DEPDC1B	<b>58</b> IDNK FRMD3	LCE3D LCE3E LCE4A LCE6A PRR9 SLC6A2 SMCP	<b>Unclassified</b>	<b>Unclassified</b>
<b>7</b> GPAM ACSL5 GUCY2GP VTI1A ZDHHC6 TECTB	<b>18</b> FBN1 CEP152 SHC4 EID1 SECISBP2L COPS2 NDUFAF4P1 GALK2 FAM227B FGF7 DTWD1 ATP8B4 SLC27A2 HDC	<b>36</b> KRTAP13-3 KRTAP13-4 KRTAP15-1 KRTAP19-1 KRTAP19-2 KRTAP19-3 KRTAP19-4 KRTAP19-5 KRTAP19-6 KRTAP19-7 KRTAP20-1 KRTAP20-4 KRTAP22-1 KRTAP22-2 KRTAP6-1 KRTAP6-2 KRTAP6-3	<b>46</b> MCTF1 FAM81B	<b>61</b> CDK1 RHOBTB1 ANK3 TMEM26	LCE3D LCE3E LCE4A LCE6A PRR9 SLC6A2 SMCP	<b>11</b> IL22 IL26	<b>Unclassified</b>
<b>8</b> ALDH18A1 SORBS1 ENTPD1 TCTN3	<b>22</b> BCAS3 TBX2 TBX4 NACA2	<b>37</b> SOD1 SCAF4 HUNK MIS18A MRAP GET	<b>47</b> EPB41L2 AKAP7 ARG1 MED23	<b>62</b> SYT4 RIT2	LCE3D LCE3E LCE4A LCE6A PRR9 SLC6A2 SMCP	<b>13</b> NALCN ITGBL1	<b>Unclassified</b>
<b>9</b> CCDC67 SMCO4	<b>23</b> GNA13 AXIN2 RGS9 CEP112 APOH PRKCA	<b>38</b> WRB LCA5L SH3BGR B3GALT5 IGSF5	<b>48</b> PRL CASC15 SOX4		LCE3D LCE3E LCE4A LCE6A PRR9 SLC6A2 SMCP	<b>19</b> SLCO3A1 SV2B CRAT37	<b>Unclassified</b>
<b>10</b> ARL1 MYBPC1 SYCP3 CHPT1 CNPTAB CCDC53 PARPBP IGF1 NUP37 PMCH SPIC UTP20	<b>24</b> CHST9 AQP4		<b>49</b> PSMC2 SLC26A5 RELN		LCE3D LCE3E LCE4A LCE6A PRR9 SLC6A2 SMCP	<b>20</b> NOD2 CYLD	<b>Unclassified</b>
	<b>25</b> ONECUT2 FECH ST8SIA3		<b>50</b> TRPV5 TRPV6 GSTK1 CASP2 EPHB6 KEL OR9A2 PIP TMEM139		LCE3D LCE3E LCE4A LCE6A PRR9 SLC6A2 SMCP	<b>21</b> CAPNS2 MMP2 LPCAT2	<b>Unclassified</b>
	<b>27</b> ZNF302 ZNF792 GRAMDIA ZNF599 ZNF880		<b>51</b> ACTR3C LRRC61 ZBED6CL RARRES2 REPIN1 GIMAP8 GIMAP7 GIMAP6 GIMAP2		LCE3D LCE3E LCE4A LCE6A PRR9 SLC6A2 SMCP	<b>26</b> SERPINB5 SERPINB12 KDSR	<b>Unclassified</b>
	<b>28</b> ZNF610 ZNF615 ZNF350 ZNF613 ZNF677		<b>52</b> SULF1 SLCO5A1 TRAM1 LACTB2 XKR9 EYA MSC		LCE3D LCE3E LCE4A LCE6A PRR9 SLC6A2 SMCP	<b>32</b> CCDC140 PAX3	<b>Unclassified</b>
					LCE3D LCE3E LCE4A LCE6A PRR9 SLC6A2 SMCP	<b>33</b> PRND PRNP PRNT PCNA	<b>Unclassified</b>
					LCE3D LCE3E LCE4A LCE6A PRR9 SLC6A2 SMCP	<b>41</b> MN1 PITPNB	<b>Unclassified</b>
					LCE3D LCE3E LCE4A LCE6A PRR9 SLC6A2 SMCP	<b>42</b> COL8A1 ST3GAL6	<b>Unclassified</b>
					LCE3D LCE3E LCE4A LCE6A PRR9 SLC6A2 SMCP	<b>55</b> PALM2 PTPN3	<b>Unclassified</b>
					LCE3D LCE3E LCE4A LCE6A PRR9 SLC6A2 SMCP	<b>59</b> FTHL17 DMD	<b>Unclassified</b>

Supplementary Table 3